Collective Nonlinear Dynamics and Self-Organization in Decentralized Power Grids

Dirk Witthaut*

Forschungszentrum Jülich,
Institute for Energy and Climate Research (IEK-STE), 52428 Jülich,
Germany
Institute for Theoretical Physics,
University of Cologne, Köln, 50937,
Germany

Frank Hellmann

Potsdam Institute for Climate Impact Research, Potsdam,
Germany[†]

Jürgen Kurths

Potsdam Institute for Climate Impact Research, Potsdam,
Germany[†]
Humboldt University Berlin, Berlin,
Germany
Lobachevsky University of Nizhny Novgorod,
Nizhnij Novgorod 603950,
Russia[‡]

Stefan Kettemann[§]

Department of Physics and Earth Sciences,
Department of Computer Science,
Jacobs University Bremen,
Campus Ring 1, 28759 Bremen,
Germany
Division of Advanced Materials Science,
POSTECH San 31,
Hyoja-dong, Nam-gu,
Pohang 790-784,
South Korea

Hildegard Meyer-Ortmanns[¶]

Department of Physics and Earth Sciences,
Jacobs University Bremen,
Campus Ring 1, 28759 Bremen,
Germany

Marc Timme**

Chair for Network Dynamics,
Center for Advancing Electronics (cfaed) and Institute for Theoretical Physics,
Technical University of Dresden, 01062 Dresden,
Germany

(Dated: October 8, 2021)

The ongoing transition to renewable energy supply comes with a restructuring of power grids, changing their effective interaction topologies, more and more strongly decentralizing them and substantially modifying their input, output and response characteristics. All of these changes imply that power grids become increasingly affected by collective, nonlinear dynamic phenomena, structurally and dynamically more distributed and less predictable in space and time, more heterogeneous in its building blocks, and as a consequence less centrally controllable. Here we review corner stone aspects of data-driven and mathematical modeling of collective dynamical phenomena emerging in real and model power grid networks by combining theories from nonlinear dynamics, stochastic processes and statistical physics, anomalous statistics, optimization, and graph theory. We introduce the mathematical background required for adequate modeling and analysis approaches, give an overview of power system models, and focus on a range of collective dynamical phenomena, including synchronization and phase-locking, flow (re)routing, Braess' paradox, geometric frustration, spreading and localisation of perturbations and cascading failures, as well as the non-equilibrium dynamics of power grids where fluctuations play a pivotal role.

CONTENTS

I. Introduction 2

II. Fundamentals of graphs and networks 4

III. Power System Models 5
  A. Static models 5
    1. Fundamentals of AC power flow 5
    2. Transformers and the per unit system 6
    3. The AC load flow equations 7
    4. Linearized power flow 8
    5. Matrix formulation 8
    6. Generalized linear approximations 9
    7. Hybrid power grids 9
  B. Optimal power flow 9
  C. Dynamic models 10
    1. The swing equation 11
    2. Principles of synchronous machines 11
    3. Dynamics of synchronous machines 12
    4. Synopsis: A hierarchy of dynamical models 13
    5. A single generator coupled to an infinite busbar 13
    6. Ohmic loads and the Kron reduction 14
    7. The structure-preserving model 15
    8. Dynamics of power electronic inverters for renewable sources 15
    9. Aggregated dynamical model 16
  D. Load frequency control 16

IV. Power Grid Topologies and Datasets 17
  A. General aspects 17
  B. Network ensembles and synthetic grid models 18
  C. Network datasets 18

V. Dynamics of Elementary Networks and Building Blocks 19
  A. Static solutions and voltage stability 19
  B. Flow and voltage limits 20
  C. Dynamic stability 21
    1. Local stability of a single generator 21
    2. Bifurcations 21
    3. Probabilistic stability measures 22
    4. Stochastic stability 23

VI. Synchronization and Steady States in Complex Grids 24
  A. The need for synchrony 24
  B. Linear Stability of the phase dynamics 25
  C. Existence, multiplicity and properties of synchronous states 25
    1. Properties of synchronous states 25
    2. Phase cohesiveness and necessary conditions 26
    3. Existence of solutions and multistability 26
  D. Nonlinear stability and explicit synchronization criteria 27
    1. Sufficient criteria for dense networks 28
    2. Sufficient criteria for sparse networks 28
  E. Probabilistic analysis of nonlinear stability 29
    1. Limit cycles and other attractors 29
    2. The impact of network structure 29
    3. The necessity of realistic models 30

VII. Structural Stability of Power Grids 31
  A. Quasi-static analysis of line outages 31
    1. The line outage distribution factors 31
    2. Spreading of failures 32
    3. Locality and the importance of distance 33
    4. The importance of community structures 34
    5. Multiple outages and collective effects 34
  B. Robustness of power grids and critical infrastructures 35
    1. Why secondary failures? 35
    2. Critical links: A graph theoretic perspective 35
    3. Generation variability and critical fluctuations 36
  C. Cascades of failures and large scale blackouts 37
    1. Simulating cascading failures 37
    2. Local versus non-local propagation 37
    3. Influence graphs 38
    4. Statistical analysis of cascading failures 38
    5. The size of cascading failures 39
    6. Transient effects in cascading failures 40
  D. Braess' paradox 40

VIII. Perturbations, Fluctuations and Transient Dynamics 41
  A. Frequency fluctuations from time series data 41
  B. Network linear response theory for fluctuating power 42
  C. Spatio-temporal responses from localized to resonant 43
    1. Propagation of short duration disturbances 43
    2. Propagation of stochastic disturbances 45
    3. Localization, distributed resonances and bulk oscillations 45
  D. Blackouts as rare events due to large fluctuations 46
  E. Ensembles of power grids for distributed fluctuations 48
    1. Basic approach 48
    2. A second network layer 49
    3. Alternatives for treating uncertainties 49

IX. Summary and Outlook 50

A. Glossary of acronyms 51

Acknowledgments 51

References 51

I. INTRODUCTION

The mitigation of climate change is one of the greatest challenges of mankind. Currently, 65% of all greenhouse gas emissions are caused by the carbon dioxide (CO_2) emissions from fossil fuel combustion and industrial processes (IPCC, 2014). Thus, a fundamental transformation of our energy system is inevitable to meet the goals

---

[*] d.witthaut@fz-juelich.de
[†] hellmann@pik-potsdam.de
[‡] kurths@pik-potsdam.de
[§] s.kettemann@jacobs-university.de
[¶] h.ortmanns@jacobs-university.de
[**] marc.timme@tu-dresden.de

of the Paris agreement to limit global warming (Rogelj *et al.*, 2015). Rapid actions are needed as greenhouse gas emissions continue to increase and the remaining carbon budgets shrink at an alarming rate (Figueres *et al.*, 2017; Rockström *et al.*, 2017).

Power grids are at the heart of this transformation. Renewable energy sources have shown a remarkable development in the last decades (Creutzig *et al.*, 2017; Edenhofer *et al.*, 2011; Wiser *et al.*, 2016), but they fundamentally change the operation of the grids they are connected to. The decarbonization of heating, transport and other sectors introduces new consumers to the electric power grid. Gas and oil heatings are replaced by heat pumps, and district heating plants use resistive heaters in times of high renewable power generation (Gröger *et al.*, 2015). Batteries of electric vehicles have to be charged, which may cause congestion in the grid (Bloess *et al.*, 2018; Carvalho *et al.*, 2015), but also offer a chance for improving stability (Gajduk *et al.*, 2014b; Liu *et al.*, 2013).

Power grids are central for our economy and daily life. It is a uniquely critical infrastructure, as a variety of other infrastructures and sectors are dependent on the secure supply of electric power (Van der Vleuten and Lagendijk, 2010). Communication, information processing, public transport, even cooling infrastructure for food supply cannot work without electric power. The energy transition further increases this dependence, as other sectors are being electrified. Ensuring a stable operation of the power system is thus a necessity and a grand challenge.

Transforming the electric power system to meet the 21st century challenges constitutes a transdisciplinary challenge (Brummitt *et al.*, 2013). Modelling, simulation and analysis of the physical grid has always been an integral part of power engineering. By now, thousands of simulations are run every hour to assess the state of the grid and potential contingencies. But the grid does not run in isolation, it is affected by the weather, by automatic controls and information systems, energy markets, and finally also by human operators and consumers. Understanding such interdependent systems is challenging, in particular when they leave the normal state of operation in case of contingencies. Complexity science can effectively complement detailed simulation models. It can elucidate fundamental mechanisms and interactions, provide explicative models, and identify new and unexpected risks. At the same time huge amounts of data become available from new measurement devices and smart grid infrastructures. This fosters an empirical and statistical view on power grid operation and stability. In summary, power systems are becoming increasingly complex and methods from statistical physics, nonlinear dynamics and network science can play an important part to address the current challenges.

Let us name three central challenges for power system operation arising during the energy transition: (i) The variability of renewable energy sources is perhaps the most well known one. Wind and solar power generation is determined by the weather and fluctuates on all temporal and spatial scales. Synoptic and seasonal variability are the most obvious features (Bloomfield *et al.*, 2018; Heide *et al.*, 2010; Staffell and Pfenninger, 2018), but power generation can also fluctuate within seconds due to atmospheric turbulence and the dynamics of clouds affecting power grid operation (Anvari *et al.*, 2016, 2017; Milan *et al.*, 2013; Zhang *et al.*, 2019). Fingerprints of these fluctuations can be observed in power grid frequency data (Haehne *et al.*, 2018), cf. also (Gorjão *et al.*, 2020b) for a comprehensive data source.

Longer timescales have gained increasing interest recently, ranging from inter-annual (Collins *et al.*, 2018) to decadal variability (Wohland *et al.*, 2019) and the impact of climate change (Schlott *et al.*, 2018; Weber *et al.*, 2018; Wohland *et al.*, 2017). A thorough statistical understanding of all modes of variability and their consequences is integral for system operation.

(ii) Furthermore, wind and solar power are typically generated at locations with favorable natural resources. These locations are often far away from consumers, so that a long-distance transmission of electric power becomes necessary (Pesch *et al.*, 2014). This increases grid loads and makes it vulnerable to large scale blackouts via cascading failures. Robustness and vulnerability are central topics in network science. Physicists have developed and analyzed a variety of models for cascading failures to understand their propagation, their statistical features and methods to mitigate them, see e.g. (Albert *et al.*, 2000; Carreras *et al.*, 2002; Dobson *et al.*, 2007, 2005; Motter and Lai, 2002; Nesti *et al.*, 2018; Schäfer *et al.*, 2018; Witthaut *et al.*, 2016; Yang *et al.*, 2017). More recently, the optimal design of networks has received a vivid interest in the scientific community, see e.g. (Kaiser *et al.*, 2020a; Katifori *et al.*, 2010; Nishikawa and Motter, 2006).

(iii) Finally, renewable power sources are different from conventional power plants operating synchronous machines. They are typically connected to the grid via power electronic inverters with different characteristics and dynamics (Carrasco *et al.*, 2006). Inverters have some important disadvantages, in particular they have no intrinsic inertia to stabilize grid dynamics (Milano *et al.*, 2018), but offer a great flexibility in design and control. Hence, the dynamical stability of complex networked systems is a topic of rapidly growing importance, cf. (Anvari *et al.*, 2020). Research must address the stability of existing systems as well as the design of future systems.

The goal of this review article is two-fold. First, it provides a starting point for physicists interested in aspects of power system dynamics, operation and robustness. To this end, the first part of the article is written as a tutorial. We provide a very short review of the main tools from dynamical systems and network science in chapter II. Then, we review basic principles of power grid operation and provide an overview of static and dynamic models for power grids in chapter III. We focus on the mathematical description of the elements of power systems, avoiding most technical details covered in the engineering literature (Grainger and Stevenson Jr., 1994; Kundur, 1994; Machowski *et al.*, 2008; Wood *et al.*, 2014). Chapter IV then briefly discusses the availability of power system datasets required for own studies and simulations. The tutorial part closes with a review of fundamental aspects of power grid stability in chapter V.

The second part of the article then reviews some recent results obtained at the interface of statistical physics, dynamical systems, network science and power engineering. We first consider aspects of dynamical stability in chapter VI. When do stable fixed points exist and how do they depend on local dynamics and network topologies? Then we analyze the robustness and vulnerability of power grids in chapter VII. How does a grid react to the failure of single elements and how do large scale blackouts emerge? Then we investigate dynamical perturbations or fluctuations and the transient dynamics of grids in chapter VIII. We conclude with an outlook on current and future research topics in chapter IX.

II. FUNDAMENTALS OF GRAPHS AND NETWORKS

A broad variety of collective dynamical phenomena in future-compliant power systems crucially depend on how consumers, producers, and storage infrastructures are interconnected. The topology of the resulting interactions typically exhibits a variety of complex structural features beyond regular lattices or random structures. We here briefly introduce basic concepts from graph theory used to quantitatively describe such topologies and remark by example where they emerge in the analysis and modeling of power systems. A more comprehensive introduction to graph theory and its applications can be found in a variety of text books, as for example (Bollobás, 1998).

A *graph* $\mathtt{G} = (\mathtt{V}, \mathtt{E})$ is given by a set $\mathtt{V} = \{1, \ldots, \mathtt{N}\}$ of *vertices* together with a set $\mathtt{E}$ of *edges* that is a symmetric subset of $\mathtt{V} \times \mathtt{V}$, i.e. if $i, j \in \mathtt{V}$ then $(i,j) \in \mathtt{E}$ if and only if $(j,i) \in \mathtt{E}$. Because of this symmetry, such a graph is also called an *undirected graph.* In a *directed graph*, the edges are ordered 2-tuples, denoted $(i,j) \in \mathtt{E}$, thus have a direction from j to i and the edge set is not necessarily symmetric.

If $(i,j) \in \mathtt{E}$, we call i and j *adjacent* or *neighbors* and write $i \sim j$, where for directed graphs, i might be *adjacent to* j but not vice versa. The *degree* of a vertex is the number of its neighbors; for directed graphs the *in-degree* is the number of edges pointing to the vertex, and the *out-degree* is the number of edges pointing from the vertex. If the degree of every vertex is the same, $k_i \equiv k$ for all i, the graph is called *k-regular* or just regular.

A *walk* in a graph is a sequence of vertices and edges

$$\mathtt{p} = (v_0, e_0, v_1, e_1, \ldots, e_{k-1}, v_k)\,, \tag{1}$$

where each successive pair of vertices v_j, v_{j+1} is connected by an edge $e_j = (v_j, v_{j+1})$. If no vertex repeats in such a sequence, it is called a *path.* A *cycle* is a walk with at least one edge, with first and last vertices identical and with no other vertices repeating. A graph is *connected* if there is a path from any of its vertices to any other. A directed graph is *strongly connected* if there is a directed path from any of its vertices to any other; it is *weakly connected* if for any two of its vertices v and w there is a directed path from v to w or from w to v. A graph with no cycles is called a *forest*; a connected forest is a *tree.*

Paths can be used to unambiguously define a metric on a graph. The (unweighted) *length* of a path $\mathtt{p}$ is simply the number k of edges in the sense of equation (1). The geodesic distance between two vertices v_n and v_m is defined as the length of the shortest path connecting the two vertices. Note that the shortest path is not necessarily unique; if no such path exists, the distance is infinite. In many applications, such a simple definition of distance is not sufficient as edges may exhibit heterogeneous features. If a distance or weight $d(e)$ is assigned to every edge $e \in \mathtt{E}$, the weighted length of a path is given by

$$\mathrm{length}(\mathtt{p}) = \sum_{j=0}^{k-1} d(e_j)\,. \tag{2}$$

As before the length defines a weighted geodesic distance via the shortest path, provided all $d(e)$ are non-negative.

The modeling of power grids and other real-world networks includes but goes far beyond the basic concepts of graph theory. In particular, we may assign quantities such as voltages or power injections to the nodes, currents and power flows to the edges and study dynamical systems on networks. We will thus need an algebraic description of networks, which links properties of nodes and edges to basic properties of graphs defined above. For a more detailed overview of algebraic graph theory and its applications to power grids see (Dörfler *et al.*, 2018).

A power grid has $\mathtt{N}$ vertices, often referred to as buses in power engineering, and $\mathtt{L}$ edges or branches. Properties of vertices such as voltages are encoded in vectors in $\mathbb{R}^{\mathtt{N}}$ or $\mathbb{C}^{\mathtt{N}}$. The absolute value of each complex number encodes the voltage magnitude and the arguments its phase (relative to a reference). Similarly, properties of edges such as flows are encoded in vectors in $\mathbb{R}^{\mathtt{L}}$ or $\mathbb{C}^{\mathtt{L}}$. The topology of such a network or graph is encoded in the *adjacency matrix* $A \in \mathbb{R}^{\mathtt{N}\times\mathtt{N}}$ with components

$$A_{n,m} = \begin{cases} 1 & \text{if vertices } n \text{ and } m \text{ are adjacent,} \\ 0 & \text{otherwise.} \end{cases} \tag{3}$$

Furthermore, it is useful to define the *node-edge incidence* *matrix* $E \in \mathbb{R}^{\mathtt{N}\times\mathtt{L}}$ with components (Newman, 2010)

$$E_{n,\ell} = \begin{cases} 1 & \text{if line } \ell \text{ starts at node } n, \\ -1 & \text{if line } \ell \text{ ends at node } n, \\ 0 & \text{otherwise.} \end{cases} \tag{4}$$

We note that power grids abstract to undirected graphs: a transmission line can transmit power in either direction. For each edge we fix an orientation to encode the direction of power flow: positive in one direction and negative in the other one. The orientation, the start and end of an edge is arbitrary, but must be kept fixed.

The node-edge incidence matrix is useful to keep track of network flows. Suppose that the flows over all edges are denoted as a vector $\boldsymbol{F} \in \mathbb{R}^{L}$, then the total in- or out-flow at all nodes is given by $E\boldsymbol{F} \in \mathbb{R}^{\mathtt{N}}$. The kernel of E corresponds to cycle flows: For any vector $\boldsymbol{F} \neq 0$ in the kernel, the in- and out-flow vanishes at every node, such that the flow must be cyclic. We can fix a basis for the kernel by choosing $\mathtt{L}-\mathtt{N}+1$ independent fundamental cycles and encode this basis in the cycle-edge incidence matrix $C \in \mathbb{R}^{\mathtt{L}\times(\mathtt{L}-\mathtt{N}+1)}$ with components

$$C_{\ell,n} = \begin{cases} 1 & \text{if edge } \ell = (i,j) \text{ belongs to cycle } c, \\ -1 & \text{if the reverse edge } (j,i) \text{ belongs to cycle } c, \\ 0 & \text{otherwise} \end{cases} \tag{5}$$

such that $EC = 0$. In a plane graph, a graph drawn on a plane without edge crossings, one typically chooses the facets of the graph as the fundamental cycles. After fixing a basis, any cycle flow (any vector in the kernel of E) can be written as $\boldsymbol{F} = C\boldsymbol{f}$, with coefficients $f_1, \ldots, f_{\mathtt{L}-\mathtt{N}+1}$.

Not all edges in a grid are equally strong; for instance the impedance typically scales with the length of a line such that longer transmission lines will have lower conductances and susceptances. We assign weights b_{ij} to all edges (i,j). These weights can either be encoded in a diagonal matrix

$$B_d = \mathrm{diag}(b_1, b_2, \ldots, b_{\mathtt{L}}) \in \mathbb{R}^{\mathtt{L}\times\mathtt{L}} \tag{6}$$

or we can define a *weighted adjacency matrix*

$$A_{n,m} = \begin{cases} b_{nm} & \text{if vertices } n \text{ and } m \text{ are adjacent,} \\ 0 & \text{otherwise.} \end{cases} \tag{7}$$

A particularly important matrix to characterize the stability of a network dynamical system is the *Laplacian matrix* $\Lambda \in \mathbb{R}^{\mathtt{N}\times\mathtt{N}}$ with components (Newman, 2010)

$$\Lambda_{n,m} = \begin{cases} \sum_{i=1}^{\mathtt{N}} b_{ni} & \text{for } n = m, \\ -b_{nm} & \text{if } n \neq m \text{ and } n, m \text{ are adjacent,} \\ 0 & \text{otherwise.} \end{cases} \tag{8}$$

Using the node-edge incidence matrix, the Laplacian is written as $\Lambda = EB_dE^\top$, where the superscript $\top$ denotes the transpose of a matrix. If all weights are positive, Λ is symmetric and positive semi-definite, i.e. all eigenvalues are real and non-negative and can be ordered as

$$0 = \lambda_1 \leq \lambda_2 \leq \cdots \leq \lambda_{\mathtt{N}}. \tag{9}$$

The second eigenvalue λ_2 measures the algebraic connectivity of a graph (Fiedler, 1973) and the associated eigenvector v_2 is called the Fiedler vector. More generally, the number of zero eigenvalues of Λ equals the number of connected components of the graph (Newman, 2010).

III. POWER SYSTEM MODELS

In this section we introduce the basic mathematical models for power system operation and stability. We start with the fundamental relations for currents and powers flows in AC power grids leading to static power grid models, then introduce dynamical models for synchronous machines and power electronic inverters.

A. Static models

1. Fundamentals of AC power flow

In an AC power grid the voltages V and currents I oscillate approximately sinusoidally with time

$$\begin{aligned} V(t) &= V_{\text{peak}}\cos(\omega t + \vartheta_V) = \sqrt{2}\,\Re(\underline{V}e^{\mathrm{i}\omega t}), \\ I(t) &= I_{\text{peak}}\cos(\omega t + \vartheta_I) = \sqrt{2}\,\Re(\underline{I}e^{\mathrm{i}\omega t}), \end{aligned} \tag{10}$$

where we have defined the *complex*-valued amplitudes

$$\underline{V} = \frac{V_{\text{peak}}}{\sqrt{2}}e^{\mathrm{i}\vartheta_V}, \qquad \underline{I} = \frac{I_{\text{peak}}}{\sqrt{2}}e^{\mathrm{i}\vartheta_I}. \tag{11}$$

Voltage and current are typically out of phase due to capacities or inductances, which is reflected by the phase factors ϑ_V and ϑ_I. As the phases of voltage and current play essential roles in describing grid operation, we will mainly employ a complex notation. In the engineering literature, the complex quantities $\underline{V}$ and $\underline{I}$ are referred to as phasors and denoted by an underline. We will adopt this notation in the following, but will denote the imaginary unit by the symbol i as it is common in physics. The electric power is oscillating, too, but only the time-averaged value

$$P = \frac{1}{T}\int_0^T V(t)I(t)dt = \Re(\underline{V}\,\underline{I}^*), \tag{12}$$

the *real power* or *active power* can do work. The imaginary part $Q = \Im(\underline{V}\,\underline{I}^*)$ describes the power temporarily stored in capacitances and inductances and is referred to as the *reactive power*. Furthermore, one defines the *apparent power* $S = P + \mathrm{i}Q = \underline{V}\,\underline{I}^*$. These relations show that the relative phases of voltages and currents are essential for the power flow in a grid. We note that deviations from perfect sinusoidal signals do occur in practice, for example higher harmonics in power electronic sources (Liang and Andalib-Bin-Karim, 2018). Nevertheless, this idealization is extremely helpful for the modeling and analysis of power systems.

The basic relation between voltage at the nodes $k, n \in \{1, \ldots, \mathtt{N}\}$ of a power grid and the currents flowing between the nodes is given by Ohm's law,

$$\underline{I}_{kn} = \frac{1}{z_{kn}}(\underline{V}_k - \underline{V}_n) = y_{kn}(\underline{V}_k - \underline{V}_n), \tag{13}$$

where $z_{kn} = r_{kn} + \mathrm{i}x_{kn}$ is the impedance and $y_{kn} = 1/z_{kn}$ the admittance of the transmission line between the nodes k and n. The admittance is divided into its real and imaginary part, $y_{kn} = g_{kn} + \mathrm{i}b_{kn}$, where g_{kn} is the conductance and b_{kn} the susceptance. For multi-circuit transmission lines, we take y_{kn} to be the sum of the admittances of the single circuits and $y_{kn} = 0$ if no transmission line exists. The total current injected to the node k is then given by $\underline{I}_k = \sum_n \underline{I}_{kn} = \sum_n y_{kn}(\underline{V}_k - \underline{V}_n)$. For actual calculations it is convenient to introduce the *nodal admittance matrix* $Y \in \mathbb{C}^{\mathtt{N}\times\mathtt{N}}$ with the entries

$$Y_{kn} = G_{kn} + \mathrm{i}B_{kn} = \begin{cases} \sum_{n=1}^{\mathtt{N}} y_{kn} & \text{if } \; k = n; \\ -y_{kn} & \text{if } \; k \neq n. \end{cases} \tag{14}$$

Ohm's law can then be rewritten in a vectorial form, which yields the *network equations*

$$\underline{\boldsymbol{I}} = Y\, \underline{\boldsymbol{V}}, \tag{15}$$

where $\underline{\boldsymbol{I}} = (\underline{I}_1, \underline{I}_2, ..., \underline{I}_{\mathtt{N}})$ represents the *complex* currents injected into the $\mathtt{N}$ nodes, and $\underline{\boldsymbol{V}} = (\underline{V}_1, \underline{V}_2, \ldots, \underline{V}_{\mathtt{N}})$ denotes the *complex* voltages. The apparent power injected to a node k is then given by

$$S_k = \underline{V}_k \underline{I}_k^*. \tag{16}$$

Real power transmission and distribution grids are mostly constructed as three-phase systems. Hence there are three conductors with voltages $V_A(t) = V_{\text{peak}}\cos(\omega t + \vartheta_V)$, $V_B(t) = V_{\text{peak}}\cos(\omega t + \vartheta_V + 2\pi/3)$ and $V_C(t) = V_{\text{peak}}\cos(\omega t + \vartheta_V + 4\pi/3)$ to ground. The voltage between two conductors oscillates sinusoidally with an amplitude of $\sqrt{3}V_{\text{peak}}$. If all three conductors have the same voltage magnitude and a fixed phase difference, it is sufficient to keep one value of $\underline{V}$ and $\underline{I}$. The basic relations such as (15) remain unchanged but the transmitted power is three times as large as in a single-phase system. The power balance at each node hence reads

$$\begin{aligned} S_k &= 3\underline{V}_k \underline{I}_k^* \qquad (17) \\ &= \sum_{n=1}^{\mathtt{N}} 3|V_k||V_n| \left(G_{kn} - \mathrm{i}B_{kn}\right)\left(\cos\theta_{kn} + \mathrm{i}\sin\theta_{kn}\right), \end{aligned}$$

where $\theta_{kn} = \theta_k - \theta_n$ is the phase difference of complex voltages $\underline{V}_k$ and $\underline{V}_n$. Real and imaginary parts yield the active and the reactive power balance conditions

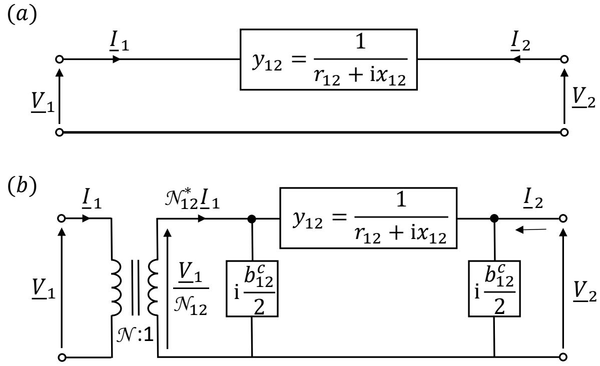

FIG. 1 Transmission elements: (a) a simple series admittance. (b) A unified transmission element consisting of an ideal transformer and a π-equivalent line model.

$$P_k = \sum_{n=1}^{\mathtt{N}} 3|V_k||V_n| \left(G_{kn}\cos\theta_{kn} + B_{kn}\sin\theta_{kn}\right), \tag{18}$$

$$Q_k = \sum_{n=1}^{\mathtt{N}} 3|V_k||V_n| \left(G_{kn}\sin\theta_{kn} - B_{kn}\cos\theta_{kn}\right). \tag{19}$$

A detailed discussion of the network equations and the resulting power flow equations are provided in (Grainger and Stevenson Jr., 1994, Chapters 7-9) and (Wood *et al.*, 2014, Chapter 6).

2. Transformers and the per unit system

Real-world transmission system are more diverse and include different transmission elements. In particular, we consider the following three types of devices. First, transformers are essential to link different voltage levels, from the transmission grid at highest voltages (380 kV in Europe, up to 765 kV in Northern America) down to the house connecting lines at low voltages (380 V in Europe). Second, special transformers may shift the phase of voltage and current on the two terminal ends (Verboomen *et al.*, 2005). Third, the model for an ordinary transmission line needs to be extended to take into account charging capacity typically present in real-world lines.

Remarkably, one can include all these devices into the common network model using a system of rescaled variables, the per unit (pu) system, and a unified model for all transmission elements depicted in Fig. 1 (b). The equivalent circuit of this transmission element includes an ideal transformer with tap ratio $\mathfrak{t}$ and phase shift θ^{shift} in addition to a π-equivalent line model. The line model includes the series admittance y and a charging susceptance b^c, which is attributed equally to the two end points of the line for the sake of simplicity.

To see how the network equations have to be modified in each case, we first consider a single transmission element as shown in Fig. 1 (b). The voltages and currents on the two terminals of the ideal transformer are related by a factor $\mathcal{N}_{12} = \mathsf{t}_{12} e^{\mathrm{i}\theta_{12}^{\text{shift}}}$. The current flowing through the series admittance is given by $y_{12}(\underline{V}_2 - \underline{V}_1/\mathcal{N}_{12})$ according to Ohm's law. Kirchhoff's current law for the junctions marked by thick black dots in the figure read

$$\underline{I}_2 = y_{21}\left(\underline{V}_2 - \frac{\underline{V}_1}{\mathcal{N}_{12}}\right) + \frac{\mathrm{i}}{2}\, b^{\mathrm{c}}_{12}\underline{V}_2, \tag{20}$$

$$\mathcal{N}_{12}^{*}\underline{I}_1 = -y_{12}\left(\underline{V}_2 - \frac{\underline{V}_1}{\mathcal{N}_{12}}\right) + \frac{\mathrm{i}}{2}\, b^{\mathrm{c}}_{12}\frac{\underline{V}_1}{\mathcal{N}_{12}}\,. \tag{21}$$

It is convenient to introduce scaled units, which are referred to as 'per unit' or 'pu' system in power engineering. We fix a reference value S_{base} for the power in the entire grid and a reference value $V_{\text{base},k}$ for the voltage separately for every voltage level k. The reference values for the currents and admittances are then given by $I_{\text{base},k} = S_{\text{base}}/(3V_{\text{base},k})$ and $Y_{\text{base},k} = I_{\text{base},k}/V_{\text{base},k}$. Generally, one selects the nominal voltage of each voltage level as the reference value, while a typical value for the power would be $S_{\text{base}} = 100$ MVA. For the π-transmission line depicted in Fig. 1 this choice yields $V_{\text{base},1}/V_{\text{base},2} = \mathsf{t}_{12}$. Dividing Eq. (20) by $I_{\text{base},2} = Y_{\text{base},2}V_{\text{base},2}$ then yields

$$\begin{aligned}\frac{\underline{I}_2}{I_{\text{base},2}} &= \frac{y_{21}}{Y_{\text{base},2}}\left(\frac{\underline{V}_2}{V_{\text{base},2}} - e^{-\mathrm{i}\theta_{12}^{\text{shift}}}\frac{\underline{V}_1}{\underbrace{\mathsf{t}_{12}V_{\text{base},2}}_{=V_{\text{base},1}}}\right)\\ &\quad + \frac{\mathrm{i}}{2}\frac{b^{\mathrm{c}}_{12}}{Y_{\text{base},2}}\frac{\underline{V}_2}{V_{\text{base},2}}\\ \Rightarrow \tilde{\underline{I}}_2 &= \tilde{y}_{21}\left(\tilde{\underline{V}}_2 - e^{-\mathrm{i}\theta_{12}^{\text{shift}}}\tilde{\underline{V}}_1\right) + \frac{\mathrm{i}}{2}\tilde{b}^{\mathrm{c}}_{12}\tilde{\underline{V}}_2,\end{aligned} \tag{22}$$

where we use a tilde to denote the scaled quantities in the pu-system, as e.g. $\tilde{\underline{I}}_2 = \underline{I}_2/I_{\text{base},2}$. Equation (21) can be rescaled analogously if we adopt the convention that $\theta_{12}^{\text{shift}} = -\theta_{21}^{\text{shift}}$. We note that $Y_{\text{base},2}$ and not $Y_{\text{base},1}$ has to be used in the normalization of the impedance, $\tilde{y}_{12} = \tilde{y}_{21} = y_{12}/Y_{\text{base},2}$, as the line is on the 2-side of the transformer, not on the 1-side.

In a large power grid with many nodes and transmission lines we then obtain

$$\tilde{\underline{I}}_k = \sum_{n=1}^{\mathtt{N}} \tilde{y}_{kl}\left(\tilde{\underline{V}}_k - e^{\mathrm{i}\theta_{kn}^{\text{shift}}}\tilde{\underline{V}}_n\right) + \frac{\mathrm{i}}{2}\tilde{b}_{kn}^{\text{charge}}\tilde{\underline{V}}_k. \tag{23}$$

We note that an ideal transformer appears as a simple series admittance $\tilde{y}_{12}$ in the pu system. This simplification will be used in the modeling of generators, which are typically connected to the grid via a step-up transformer.

Rewriting equations (23) in a vectorial form we recover the network equations in the form (15), however with a modified modal admittance matrix $\tilde{Y}$ defined as

$$\tilde{Y}_{kn} = \begin{cases} \sum_{n=1}^{\mathtt{N}} \tilde{y}_{kn} + \mathrm{i}\tilde{b}^{\mathrm{c}}_{kn}/2 & \text{if } k = n,\\ -\tilde{y}_{kn}e^{\mathrm{i}\theta_{kl}^{\text{shift}}} & \text{if } k \neq n. \end{cases} \tag{24}$$

Finally, the power is rescaled to the pu system by dividing Eq. (17) through the reference value $S_{\text{base}} = 3V_{\text{base},k}I_{\text{base},k}$ which yields $\tilde{S}_k = \tilde{\underline{V}}_k\tilde{\underline{I}}_k^*$ as desired.

The pu system thus simplifies the network equations, as we can treat all transmission elements alike. In addition, it is advantageous for numerical calculations as all quantities are of order unity such that rounding errors are minimized. All details of the transmission elements, are absorbed in the nodal admittance matrix $\tilde{Y}$. In the absence of phase shifters, $\tilde{Y} = \tilde{Y}^{\top}$ is symmetric. A detailed discussion of the pu systems and its benefits is provided in (Grainger and Stevenson Jr., 1994, Chapters 1,2).

3. The AC load flow equations

In previous sections we have established a set of nonlinear algebraic equations describing the steady state of AC power grids, linking nodal power injections P_n, Q_n to nodal state variables θ_n, $|V_n|$. Two of these four quantities are fixed externally for every node, for instance via power demand. The remaining unknown variables are obtained by numerical solution of the load-flow equations, see (Grainger and Stevenson Jr., 1994, Chapter 9), (Wood *et al.*, 2014, Chapter 6) for a detailed introduction.

In practice, we distinguish three types of nodes. A PV bus is typically connected to a generator, which provides a fixed power output P at fixed voltage magnitudes $|V|$. A PQ bus represents a node with a given consumption, such that net injected active power P and reactive power Q are given, while the voltages at these nodes are unknown. A special kind of bus is the slack bus, that captures the supply of the power necessary to have overall power balance in the system to ensure that there exists a steady state solution. It acts as an ideal voltage source (fixed $\underline{V}$), where the parameters P and Q remain unspecified to balance active and reactive power during the iteration towards the steady state solution. This is necessary because power losses on the transmission lines are not known *a priori*, before the solution is obtained.

Suppose we are interested in a transmission grid of $\mathtt{N}_\ell$ loads, $\mathtt{N}_g$ generators plus one generator node taken as slack. Then, we have $2\mathtt{N}_\ell + \mathtt{N}_g$ unknown state variables: the phases of all $\mathtt{N}_g + \mathtt{N}_\ell$ non-slack nodes and the voltage magnitudes of $\mathtt{N}_\ell$ load nodes. These unknown variables are fixed by $2\mathtt{N}_\ell + \mathtt{N}_g$ nonlinear algebraic equations:

$$\begin{aligned} P_n\left(\theta_1, \cdots, \theta_{\mathtt{N}_g+\mathtt{N}_\ell}, |V_1|, \cdots, |V_{\mathtt{N}_\ell}|\right) &= P_n^{\text{sp}},\\ Q_k\left(\theta_1, \cdots, \theta_{\mathtt{N}_g+\mathtt{N}_\ell}, |V_1|, \cdots, |V_{\mathtt{N}_\ell}|\right) &= Q_k^{\text{sp}}, \end{aligned} \tag{25}$$

where n labels all non-slack nodes, while k labels load nodes only. The superscript "sp" indicates that values on the right side are specified beforehand and the functions $P_n(\cdot)$ and $Q_k(\cdot)$ are given by Eq. (18) and Eq. (19).

A common and effective way to solve this equation system is the Newton-Raphson method (cf. (Grainger and Stevenson Jr., 1994, Chapter 9), (Wood *et al.*, 2014, Chapter 6)), which iteratively updates the state vector from an initial guess towards the solution of Eqs. (25). The solution for the state vector describes the power grid in steady-state operation. We note that a set of nonlinear equations may exhibit a single well-defined solution but may also have no or several solutions. The lack of a solution indicates an unstable situation to be further discussed in section V.A, while multistability will be addressed in section VI.C.3. Recent advances and challenges in numerical methods for AC power flow computations are discussed in (Mehta *et al.*, 2016; Trias, 2012).

4. Linearized power flow

For small loads and losses in a power grid, load flow calculations simplify considerably (Wood *et al.*, 2014, Chapter 6.18) via linearized power flow equations that are based on three approximations. (i) For each transmission element, the resistance and the charging susceptance are small compared to the reactance and are thus neglected. Hence, the admittance is purely imaginary, $y_{nk} = 1/(\mathrm{i}x_{nk})$. (ii) Variations of the voltage magnitude are typically small in transmission grids, such that we can fix them at the reference value of the respective voltage level. In the pu system we thus write $\underline{V}_n = e^{\mathrm{i}\theta_n}$ and the power balance at a node n reads (cf. Eq. (18) and (20))

$$\underline{S}_n = \underline{V}_n \underline{I}_n^* = \sum_{k=1}^{\mathtt{N}} \frac{1}{\mathrm{i}\tilde{x}_{nk}} (\underline{V}_n^* - e^{-\mathrm{i}\theta_{nk}^{\text{shift}}} \underline{V}_k^*) \underline{V}_n. \tag{26}$$

Technically, all nodes must then be considered as PV buses, such that no equations for the reactive power must be taken into account. Taking the real part of equation, we obtain the balance equation for the real power,

$$P_n = \sum_{k=1}^{\mathtt{N}} P_{n\to k} = \sum_{k=1}^{\mathtt{N}} \frac{1}{\tilde{x}_{nk}} \sin(\theta_n - \theta_k - \theta_{n,k}^{\text{shift}}). \tag{27}$$

(iii) Finally, small loads imply that the phase differences across a transmission line are small such that the sine function is approximated to first order. The load flow calculations then reduce to a set of linear equations

$$\sum_{k=1}^{\mathtt{N}} B_{nk}\theta_k = P_n^{\text{sp}} - P_n^{\text{shift}}, \tag{28}$$

where $P_n^{\text{shift}} = \sum_k B_{nk}\theta_{nk}^{\text{shift}}$ accounts for the effects of the phase shifting transformers and the matrix $B \in \mathbb{R}^{\mathtt{N}\times\mathtt{N}}$ is the nodal susceptance matrix expressed in per-units but without taking into account potential phase shifts:

$$B_{n,k} = \begin{cases} \sum_m \tilde{x}_{nm}^{-1} & \text{if } n = k; \\ -\tilde{x}_{nk}^{-1} & \text{if } n \text{ is connected to } k \\ 0 & \text{otherwise.} \end{cases} \tag{29}$$

The simplified Eq. (28) is often referred to as the DC approximation, as it is mathematically equivalent to Kirchoff's circuit equation for DC electric circuits. Still, it describes the flow of real power in AC power grids. Obviously, linear equations can be solved much faster than nonlinear load flow Eqs. (25), which is advantageous when the flow must be calculated for many different scenarios of generation and load. Furthermore, the linear approximation avoids the problem of multiple or disappearing solutions or multiple optima in optimization problem. Limits of its applicability are discussed in detail in (Purchala *et al.*, 2005; Stott *et al.*, 2009; Van Hertem *et al.*, 2006).

A word of caution is in order, as the symbol B is used for several related but different quantities. Transmission lines and ordinary transformers have a positive reactance $\tilde{x} > 0$. Hence, the off-diagonal elements of the nodal susceptance matrix (29) are negative. In contrast, the imaginary parts of the nodal admittance matrix elements (14) are positive. Both quantities are denoted by the symbol B and one must be careful to not confuse them.

5. Matrix formulation

The linearized power flow equations can be condensed in a highly practical compact matrix notation. So let $\mathtt{N}$ denote the number of nodes and $\mathtt{L}$ the number of lines in a grid as before. We define the vectors of power injection $\boldsymbol{P} = (P_1, \ldots, P_{\mathtt{N}})^\top \in \mathbb{R}^{\mathtt{N}}$, the vector of voltage phase angles $\boldsymbol{\theta} = (\theta_1, \ldots, \theta_{\mathtt{N}})^\top \in \mathbb{R}^{\mathtt{N}}$ and the vector of line flows $\boldsymbol{F} = (F_1, \ldots, F_{\mathtt{L}})^\top \in \mathbb{R}^{\mathtt{L}}$. As the flow is directed, we must assign an orientation to each line in the grid which is arbitrary but must be kept fixed.

The directed real power flow F_ℓ on a line ℓ from node m to node n is given by $F_\ell = x_\ell^{-1}(\theta_m - \theta_n)$. Using the diagonal matrix B_d defined in Eq. (6) with weights $b_\ell = x_\ell^{-1}$ and the node-edge incidence matrix (4), the relation of flows and phase angles are given by

$$\boldsymbol{F} = B_d E^\top \boldsymbol{\theta}. \tag{30}$$

The real-power balance at each node now reads

$$\boldsymbol{P} = E\boldsymbol{F}, \tag{31}$$

stating that the power flowing out of each node must equal the power injected at the node. Combining (30) and (31) the equation for the power injections in terms of the voltage angles is obtained as

$$\boldsymbol{P} = EB_d E^\top \boldsymbol{\theta} = B\boldsymbol{\theta}. \tag{32}$$

Together with Eq. (30) we thus have a linear relation between line flows $\boldsymbol{F}$ and nodal power injections $\boldsymbol{P}$.

The matrix $B = EB_dE^\top$ with elements given is Eq. (29) is a weighted Laplacian and thus has a single zero eigenvalue if the network is connected (cf. section

II). Thus, it is non-invertible and we solve (32) for $\boldsymbol{\theta}$ via the Moore-Penrose pseudo-inverse B^* to obtain the line flows directly as a linear function of the nodal power injections

$$\boldsymbol{F} = \underbrace{B_d E^\top B^*}_{=:\text{PTDF}} \boldsymbol{P}. \tag{33}$$

The matrix prefactor is called power transfer distribution factor (PTDF) matrix (Wood *et al.*, 2014), as it describes how power injections are distributed throughout the grid.

The zero eigenvalue of the Laplacian B represents a phase-shift invariance. Uniformly shifting all nodal phases by the same constant c, $\theta_n \to \theta_n + c$, does not affect any power flows. Fixing the phase angle $\theta_k \equiv 0$ at one node k (the slack node) removes this degree of freedom. We then remove the node from the analysis by removing the k-th row from the vector $\boldsymbol{\theta}$ and the k-th row and k-th column from the matrix B. The resulting matrix is called a *grounded Laplacian.*

6. Generalized linear approximations

Several generalizations of the DC approximation have been developed and we briefly comment on three of them. (i) First, one can improve on the linear approximation of the sine function by rewriting the governing equations of the DC approximation in two parts. First we have

$$\boldsymbol{P} = E B_d \boldsymbol{\psi}, \tag{34}$$

where ψ_ℓ denotes the sine of the phase difference along the line ℓ. In the ordinary DC approximation, one simply replaces the sine by its argument; in vectorial form one thus obtains $\boldsymbol{\psi} = E^\top \boldsymbol{\theta}$. If we do not neglect the sine, we would instead have

$$\boldsymbol{\psi} = \sin(E^\top \boldsymbol{\theta}). \tag{35}$$

The basic idea of the generalized DC approximation (Dörfler and Bullo, 2013; Simpson-Porco, 2017) is to first obtain $\boldsymbol{\psi}$ approximately and then solve for $\boldsymbol{\theta}$. The general solution to the underdetermined Eq. (34) reads

$$\boldsymbol{\psi} = E^\top B^* \boldsymbol{P} + B_d^{-1} C \boldsymbol{f}, \tag{36}$$

where C is the cycle-edge incidence matrix (5) and $\boldsymbol{f}$ a vector of cycle flows. To find the actual value of the cycle flows, we would obtain the correct solution of the nonlinear power flow equations, an approach discussed in section VI.C. Here we consider practical approximate solutions, and assume the cycle flows $\boldsymbol{f}$ to be negligible under normal operating conditions. Eq. (35) then yields

$$\boldsymbol{\theta} \approx (E E^\top)^{-1} E \, \arcsin(E^\top B^* \boldsymbol{P}). \tag{37}$$

(ii) A second generalization is to approximately incorporate Ohmic losses in a linear fashion. Two iterative procedures that introduce losses, but keep the assumption of fixed voltage magnitudes, are described in (Simpson-Porco, 2017; Stott *et al.*, 2009).

(iii) A third class of linear models includes reactive power flows and voltage variations by appropriate linearization of the nonlinear AC load flow equations. Different approaches have been discussed in (Coffrin *et al.*, 2012; Yang *et al.*, 2019; Zhang *et al.*, 2013).

7. Hybrid power grids

High voltage DC (HVDC) transmission lines can transmit bulk power over large distances with lower capital cost and lower losses than standard AC lines (Setreus and Bertling, 2008). They are connected to AC via power electronic converter stations, which offers a high degree of flexibility. The transmitted real power can be controlled by the grid operator. Modern converter stations can provide system services such as reactive power. HVDC lines are included in a load flow study rather easily by representing the two converter stations by two additional PV buses. One of the converter nodes draws a power $P_f < 0$ from the grid at node f, and the other converter then feeds a power

$$P_t = -P_f - P_{\text{loss}} = -P_f - (l_0 - l_1 P_f), \tag{38}$$

back into the grid at node t. Losses are typically small so that l_0 is of the order of a few MW and l_1 a few percent.

B. Optimal power flow

A fundamental problem in power engineering and energy economics is to determine the cost-optimal dispatch of generators: Which generators should run to satisfy a given demand at minimum costs (Grainger and Stevenson Jr., 1994, Chapter 13),(Wood *et al.*, 2014, Chapter 8)? We will address this problem in terms of the DC approximation, taking into account the real power generation and demand, but neglecting losses. Suppose that the total demand or load is given by $P_{\text{tot}}^{\text{load}}$ and that there are $\mathtt{N}_g$ generators which can be used to satisfy this demand at minimum costs. The actual generation P_m^{gen} of each generator $m = 1, \ldots, \mathtt{N}_g$ is bounded by the technical capacity such that we have the constraints

$$0 \le P_m^{\text{gen}} \le P_m^{\max}. \tag{39}$$

The power balance condition in the grid reads $\sum_{m=1}^{\mathtt{N}_g} P_m^{\text{gen}} = P_{\text{tot}}^{\text{load}}$. We assume for simplicity that the costs are proportional to the output P_m^{gen} for each generator. Then the total variable costs can be written as

$$\text{Cost}_{\text{tot}} = \sum_{m=1}^{\mathtt{N}_g} c_m P_m^{\text{gen}}, \tag{40}$$

where c_m denotes the variable costs for generator m. If there are no further constraints, the solution with minimum costs is simple: Switch on all generators consecutively according to their variable costs c_m such that

$$P_m^{\rm gen} = \begin{cases} P_m^{\rm max} & c_m < c^* \\ P_{\rm tot}^{\rm load} - \sum_m' P_m^{\rm max} \quad \text{for} & c_m = c^* \\ 0 & c_m > c^*, \end{cases} \tag{41}$$

where c^* is the variable cost of the last generator switched on which is identified with the market electricity price. The primed sum in the equation runs over all generators with $c_m < c^*$. This is called the *merit order principle*.

In real-world applications there are many more necessary conditions and constraints. Most importantly, the real power flow in each transmission line must not exceed the line rating in order not to become overloaded and fail,

$$|F_\ell| \leq F_\ell^{\rm max} \quad \text{for all lines } \ell. \tag{42}$$

To satisfy this condition we must consider where power is generated and consumed. In particular, the demand or load $P_i^{\rm load}$ must be specified separately for every node $i \in \{1, \ldots, \mathtt{N}\}$ of the grid. We can then express all line flows F_ℓ in terms of the dispatch $P_m^{\rm gen}$ as follows. We first introduce a generator incidence matrix $E^{\rm gen}$ which indicates where each generator is connected to the grid,

$$E_{i,m}^{\rm gen} = \begin{cases} 1 & \text{if generator } m \text{ is connected to node } i \\ 0 & \text{otherwise.} \end{cases} \tag{43}$$

The resulting net real power injection is thus given by

$$P_n = \sum_{m=1}^{\mathtt{N}_g} E_{n,m}^{\rm gen} P_m^{\rm gen} - P_n^{\rm load}, \tag{44}$$

for every node n. Next, the line flows F_ℓ can be expressed by power injections via Eq. (33), leading to an affine linear relation of flows F_ℓ and optimization variables $P_m^{\rm gen}$. Finally, we arrive at the following important optimization problem, commonly referred to as DC or linear optimal power flow (DC-OPF):

$$\begin{aligned} &\min_{P_m^{\rm gen}} \sum_{m=1}^{\mathtt{N}_g} c_m P_m^{\rm gen} \\ &\text{such that } 0 \leq P_m^{\rm gen} \leq P_m^{\rm max}, \quad |F_\ell| \leq F_\ell^{\rm max}. \end{aligned} \tag{45}$$

Mathematically, this optimization problem is a linear program which admits an efficient solution. Different formulations and their computational efficiency are discussed in (Hörsch *et al.*, 2018b). Eq. (45) represents the basic optimal power flow problem and various extensions have been discussed for real world applications leading to a vast body of literature (Frank *et al.*, 2012a,b; Huneault and Galiana, 1991; Momoh *et al.*, 1999a,b). The linear function (40) is a strong simplification of the real cost function. It can be replaced by a convex function without changing the overall complexity of the optimization problem. In contrast, a non-convex cost function strongly alters the nature of the problem, making it hard to solve in general. Another approach is to consider different modes of operation of a generator. In the simplest case the generator is either *on* or *off*. If a generator is *on* it typically has a minimum generation such that an additional constraint $P_m^{\rm min} \leq P_m^{\rm gen}$ arises. To take into account this switching behavior, an additional binary optimization variable is introduced, leading to a a mixed-integer linear program (MILP).

Variable renewable energy sources may be included in two different ways. If renewable generation is taken to be fixed, the real power load at each node $P_i^{\rm load}$ is replaced by the *residual load*, i.e. the difference of load and renewable generation. However, renewable generation will exceed the load at least temporarily in future energy systems. To allow for a *curtailment* of the power generation, wind farms and PV parks are included as generators with zero variable costs and $P_m^{\rm max}$ is set to the assumed or forecasted power generation. For optimization, we may then choose any value between $P_m^{\rm gen} = 0$ (complete curtailment) and $P_m^{\rm gen} = P_m^{\rm max}$, depending on what best benefits the grid. A systematic way of optimizing the dispatch under uncertainties in production and demand is sketched in section VIII.E, where the system constraints are satisfied only with a specified probability.

A further natural extension is to abandon the assumptions of the DC approximation and start from the full nonlinear AC power flow equations. However, the resulting optimization problem is again non-convex which is much harder to solve. The development of algorithms for this problem is an active field of research (see, e.g. (Engelmann *et al.*, 2017; Erseghe, 2014)).

C. Dynamic models

While load flow calculations describe the steady-state of a power grid, a large set of models of different complexity is available to analyze its dynamics and the stability of steady states. Which model to chose depends crucially on the phenomena and the time scales that shall be investigated (Sauer *et al.*, 2018). The bulk power generation and demand change on time scales of minutes to hours. Optimization models are routinely used to model how the unit commitment and power flows change from hour to hour. In the following, we focus on the next time scale and address aspects of synchronisation, transient stability and, to a lesser extend, voltage dynamics and load-frequency control. These phenomena typically take place on time scales of 10^{-1} to 10^1 seconds. Faster phenomena, including subtransient effects and electromagnetic propagation effects, as well as the modeling of generator control and protection systems are not covered in this review article. A much more detailed and extensive introduction can be found in the standard text books (Kundur, 1994; Machowski *et al.*, 2008; Sauer *et al.*, 2018). An overview of different modeling aspects can be found in the articles (Gajduk *et al.*, 2014a; Nishikawa and Motter, 2015).

1. The swing equation

The classic swing equation describes the dynamics of the mechanical rotation of a synchronous machine (Machowski *et al.*, 2008, Chapter 5.1), (Nishikawa and Motter, 2015). The basic dynamical variable is the mechanical phase angle which is identical to the voltage phase angle (hence the term 'synchronous machine'). The phase angle δ is commonly measured relative to a frame of reference rotating at the reference frequency of the grid ω_R. The dynamics is then simply given by Newton's equation

$$J\ddot{\delta} = \mathfrak{T}_{\mathrm{mech}} - \mathfrak{T}_{\mathrm{el}} - D_{\mathrm{mech}}\omega - (D_{\mathrm{el}} + \kappa)\Delta\omega, \qquad (46)$$

where $\omega = \dot{\delta}$ is the angular frequency, $\Delta\omega = \omega - \omega_R$ its deviation from the reference, J is the moment of inertia of the machine, $\mathfrak{T}_{\mathrm{mech}}$ the mechanical torque driving the rotating machine and $\mathfrak{T}_{\mathrm{el}}$ the electromagnetic torque due to the power transferred to the grid. The machine experiences mechanical friction with damping coefficient D_{mech} and an effective damping due to damper windings characterized by coefficient D_{el}. In addition, one sometimes includes the effects of a frequency controller with gain constant κ, which will be discussed in detail in section III.D. Aggregating the damping factors $D = D_{\mathrm{mech}} + D_{\mathrm{el}} + \kappa$ and noting that $\dot{\delta} = \omega$ we obtain

$$J\omega_R\ddot{\delta} + D\omega_R\dot{\delta} = \frac{\omega_R}{\omega}\Big[\underbrace{(\mathfrak{T}_{\mathrm{mech}} - D_{\mathrm{mech}}\omega_R)\omega}_{=P_{\mathrm{mech}}} - \underbrace{\mathfrak{T}_{\mathrm{el}}\omega}_{=P_{\mathrm{el}}}\Big]. \qquad (47)$$

We have thus related the dynamics to the net mechanical input power P_{mech} and the electric power P_{el} acting on the machine. The swing equation is used to analyze the stability and small-amplitude dynamics around a steady state, hence we can approximate $\omega_R/\omega \approx 1$.

As for static flows, calculations are often carried out in dimensionless units, i.e. the pu system. To make the swing equation (47) dimensionless, we divide it by the rated power of the machine P_R and define the quantities

$$H = \frac{\frac{1}{2}J\omega_R^2}{P_R}, \qquad \tilde{D} = \frac{D\omega_R}{P_R}\,. \qquad (48)$$

The inertia constant H measures the ratio of stored kinetic energy and output power of the machine when it operates under normal conditions. Typical values are of the order of $4 - 6s$. Then, we obtain the *swing equation*

$$\frac{2H}{\omega_R}\ddot{\delta} + \tilde{D}\dot{\delta} = \tilde{P}_{\mathrm{mech}} - \tilde{P}_{\mathrm{el}}, \qquad (49)$$

where the power is now expressed in the pu system. The motion of the generator is coupled to the rest of the grid via the exchanged real power P_{el}, which we discuss below.

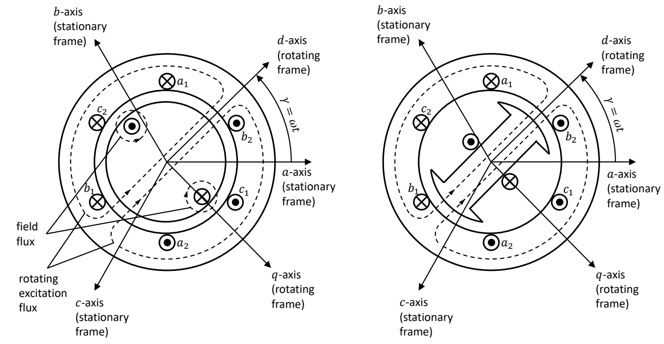

FIG. 2 Schematic of round-rotor synchronous machine (left) and a salient pole machine (right).

2. Principles of synchronous machines

As a next step towards a full machine model, we have to examine how the mechanical rotation induces voltages and currents. A careful introduction can be found in (Machowski *et al.*, 2008, Chapter 3.3), we here provide only the essential results. Consider first an unloaded round-rotor generator as depicted in Fig. 2. The rotor carries a field coil, where a DC current I_f generates a magnetic field. The stator consists of three coils called A,B,C in which the rotating field induces an AC voltage, cf. section III.A.1. The magnetic flux in the A coil with M_f windings, $\Psi_{rA}(t) = M_f I_f \cos(\omega t)$, induces the voltage

$$E_{rA}(t) = -\frac{d\Psi_{rA}}{dt} = \omega M_f I_f \sin(\omega t), \qquad (50)$$

commonly referred to as the 'air-gap' electromagnetic force (EMF). The EMFs in coils B and C are the same up to a phase shift of $\pm 2\pi/3$. If the generator is connected to a load or the grid, a current

$$I_A(t) = I_M \cos(\omega t - \varphi) = \sqrt{2}\Re\left(\underline{I}e^{\mathrm{i}\omega t}\right) \qquad (51)$$

flows through the coil. It is generally phase shifted with respect to the voltage. Here $\underline{I} = I_m e^{-\mathrm{i}\varphi}/\sqrt{2}$ is a complex ("phasor") quantity. The voltage drop at the coil then reads

$$E_{rA}(t) = \omega M_f I_f \sin(\omega t) + \underbrace{\omega L_A}_{=:X_A} I_M \cos(\omega t - \varphi). \qquad (52)$$

An explicit modeling of synchronous machines, including magnetic fluxes and DC currents, is cumbersome and not always necessary for analyzing large grids with tens to thousands of machines. Often, an aggregated description in terms of voltage and current phasors is sufficient. Notable exceptions include the modeling of reactive power limits for voltage collapse, the detailed simulation of system wide transients, or the design of power system stabilizers. In the aggregated description, one defines the two

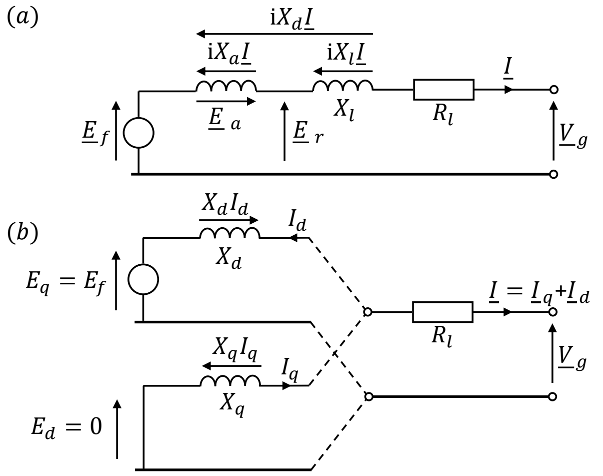

FIG. 3 Equivalent circuit diagram of (a) a round-rotor synchronous machine and (b) a salient pole machine.

phasor variables $\underline{E}_f = \omega M_f I_f/\sqrt{2}$ and $\underline{E}_r$ describing the air-gap EMF. Then, Eq. (52) reads $\underline{E}_r = \underline{E}_f - \mathrm{i}X_A\underline{I}$. We can further take into account imperfections, losses and leakage of magnetic flux by an additional impedance $R_l + iX_l$ between the air-gap EMF and the terminal voltage of the generator $\underline{V}_g$ to obtain

$$\underline{V}_g = \underline{E}_f - \mathrm{i}X_A\underline{I} - (R_l + \mathrm{i}X_l)\underline{I}. \tag{53}$$

Hence, the basic relation between the rotor quantities, the air-gap EMF at the stator coils, and the terminal generator voltage can be represented by a simple equivalent circuit as depicted in Fig. 3. This description is very effective and compatible with electric circuit theory.

In a salient pole machine the rotor is asymmetric, see Fig. 2. The asymmetry can be taken into account approximately in an effective model that differs only slightly from the case of a round-rotor machine. We decompose all phasors into two contributions, in- and out-of-phase with the magnetic flux of the rotor. The two components are denoted by the subscripts d and q referring to the direct and quadrature axis, respectively. To describe the asymmetry, we replace the effective reactance X_A by X_{Ad} and X_{Aq} for the $d-$ and $q-$component. Hence Eq. (53) is replaced by the two-component equations

$$\begin{aligned} E_d &= V_{gd} + X_q I_q + R_l I_d = 0 \\ E_q &= V_{gq} - X_d I_d + R_l I_q = E_f, \end{aligned}$$

with $X_q = X_{Aq} + X_l$ and $X_d = X_{Ad} + X_l$. Fig. 3 shows the equivalent diagram of the synchronous machine. Recombining the components yields the phasors of current and terminal voltage,

$$\begin{aligned} \underline{V}_g &= \underline{V}_{gd} + \underline{V}_{gq} = V_{gd} + \mathrm{i}V_{gq}, \\ \underline{I} &= \underline{I}_d + \underline{I}_q = I_d + \mathrm{i}I_q. \end{aligned} \tag{54}$$

Why have we introduced the EMFs E_q and E_p in addition to E_f? The quantities $E_{d,q}$ characterize the physical source of the induced voltage – the magnetic flux of the field coil, while E_f quantifies the current in the field coil. The simple relations $E_q = E_f$ and $E_d = 0$ hold only during the steady operation of the machine. After a disturbance, the magnetic flux changes and so do the effective EMFs $E_{q,d}$. Hence, $E_{q,d}$ become dynamic state variables for which we introduce the equations of motion in the next section. In contrast, E_f is a fixed system parameter or, if we include excitation control of the synchronous machine, a control variable.

3. Dynamics of synchronous machines

We now proceed to model the transient dynamics of a synchronous machine. A detailed derivation is available in textbooks on electric machines (Machowski *et al.*, 2008, Chapter 11.1). Here we only quote the result and provide a brief motivation for the form of the resulting equations.

Recall that a machine in the steady state was modeled by an EMF $\underline{E} = \underline{E}_q + \underline{E}_d$ connected to the terminal ends via the reactances X_q and X_d, respectively. A similar approach can be used to describe the transient dynamics of a synchronous machine. The EMFs become time dependent, commonly indicated by a dash. Similarly, we must assign a different, transient value to the reactances. We stress that these are only effective quantities, which yield a highly condensed description of the dynamics. A full dynamical model of a synchronous machine must be based on the magnetic fluxes in the different coils, the voltages and currents and the model's complexity increases quickly.

We first consider the EMF dynamics in the q-axis, which quantifies the flux in the field coil (more precisely the field flux linkage). In steady state the flux is proportional to the voltage exciting the field coil, which leads to $E_q = E_f$. In the transient regime two additional terms have to be taken into account when considering the voltage in the field coil. Firstly, the magnitude of flux changes leads to an inductive term proportional to $\dot{E}_q$. Secondly, there is a term due to the coupling to the stator. A careful accounting of these terms yields the equation (Machowski *et al.*, 2008)

$$E_q' + T_{do}\dot{E}_q' - (X_d - X_d')I_d = E_f. \tag{55}$$

A similar relation can be found for the d-axis EMF:

$$E_d' + T_{qo}\dot{E}_d' + (X_q - X_q')I_q = 0. \tag{56}$$

We note that these two equations cover only the transient dynamics after a disturbance. Further models have been introduced to describe the very short sub-transient dynamics. We omit these models, as they typically yield only a small improvement (Stott, 1979; Weckesser *et al.*, 2013). It should be noted, however, that higher-order models include damper winding explicitly, which we had to include phenomenologically in the swing equation.

4. Synopsis: A hierarchy of dynamical models

Combining the results from the previous section with the swing equation we obtain a hierarchy of models (Machowski *et al.*, 2008, Chapter 11.1). In the two-axis or *fourth order model* the generator is described by four state variables, the transient EMFs E'_q and E'_d, the mechanical phase angle δ relative to the grid and its derivative ω, which evolve according to

$$\begin{aligned} \frac{2H}{\omega_R}\dot{\omega} &= -\tilde{D}\omega + \tilde{P}_{\mathrm{mech}} - \tilde{P}_{\mathrm{el}}, \\ \dot{\delta} &= \omega, \\ T_{do}\dot{E}'_q &= E_f - E'_q + (X_d - X'_d)I_d, \\ T_{qo}\dot{E}'_d &= -E'_d + (X_q - X'_q)I_q. \end{aligned} \tag{57}$$

The one-axis or *third-order model* neglects the dynamics of E'_d (Schmietendorf *et al.*, 2014). Often it is set to zero, $E'_d = 0$, as in the elementary steady state model discussed in section III.C.2. Hence, the model reduces to three state variables per generator and the last equation in (57) is omitted.

The second order or *classical model* is widely used in the analysis of power system dynamics. It describes the mechanical motion of the generator at constant EMFs:

$$\begin{aligned} \frac{2H}{\omega_R}\dot{\omega} &= -\tilde{D}\omega + \tilde{P}_{\mathrm{mech}} - \tilde{P}_{\mathrm{el}}, \\ \dot{\delta} &= \omega. \end{aligned} \tag{58}$$

To study the resulting dynamics of the state variables, we have to specify the remaining quantities in the equations of motion. The electric quantities $\tilde{P}_{\mathrm{el}}$, I_q and I_d are time dependent. In fact, they are related to the state variables of all connected generators via algebraic equations describing the grid as discussed in detail below. The quantities E_f and $\tilde{P}_{\mathrm{mech}}$ are set by the control system of the generator, more precisely the exciter and the governor (Machowski *et al.*, 2008). If the action of the control system is ignored, they become fixed system parameters. The remaining quantities, in particular the time constants T and the reactances X, are regarded as constant system parameters.

We note that detailed models can also include subtransient effects yielding a sixth-order model (Machowski *et al.*, 2008). Furthermore, dynamical models can be reformulated as adaptive networks (Berner *et al.*, 2021) or port Hamiltonian systems (Fiaz *et al.*, 2013; Mehrmann *et al.*, 2018), which enables further insights and generalizations.

5. A single generator coupled to an infinite busbar

First basic insights into power system stability can be obtained by focusing on the dynamics of a single generator (Machowski *et al.*, 2008, Chapters 5.3-5.5). To this end, we assume that the generator is connected to a huge system and that the influence of the generator on that system is negligible. Such a setup is commonly referred to as an 'infinite busbar' with a fixed voltage V_s. We carry out the calculation in the reference frame of the rotor, and recall that the angle between the rotor and the stator frame is denoted by δ. Hence, the system voltages at the infinite busbar is written as

$$V_{sq} = V_s\cos(\delta), \quad V_{sd} = -V_s\sin(\delta). \tag{59}$$

The generator is connected to the infinite bus bar through a set of grid elements, modeled as series impedances. First, there may be internal losses or a leakage in the machine which is described by the impedance $R_l + \mathrm{i}X_l$. Then there is typically a step-up transformer which we describe by the impedance $R_T + \mathrm{i}X_T$, recalling that the pu system takes care of voltage levels automatically. Finally, there are transmission elements with effective impedance $R_S + \mathrm{i}X_S$ to the system. Typically, resistances can be neglected since Ohmic losses as well as shunt impedances are small. Then, the machine EMFs and the system voltages are related by

$$\begin{aligned} &V_{sd} = E'_d - x'_q I_q, \quad V_{sq} = E'_q + x'_d I_d, \\ &\Rightarrow I_q = \frac{E'_d + V_s\sin(\delta)}{x'_q}, \quad I_d = \frac{-E'_q + V_s\cos(\delta)}{x'_d}, \end{aligned} \tag{60}$$

where we have introduced the short-hand $x'_d = X'_d + X_l + X_T + X_s$ and $x'_q = X'_q + X_l + X_T + X_s$. Neglecting Ohmic losses, the air-gap power acting on the machine equals the real power at the system terminal end

$$\begin{aligned} \tilde{P}_{\mathrm{el}} &= V_{sq}I_q + V_{sd}I_d \qquad (61) \\ &= E'_d I_d + E'_q I_q + (x'_d - x'_q)I_d I_q \\ &= \frac{E'_q V_s}{x'_d}\sin(\delta) + \frac{E'_d V_s}{x'_q}\cos(\delta) - \frac{V_s^2}{2}\frac{x'_q - x'_d}{x'_q x'_d}\sin(2\delta). \end{aligned}$$

We have thus found explicit expression for the quantities $\tilde{P}_{\mathrm{el}}$, I_q and I_d in terms of the generator state variables, closing the equations of motion of Sec. III.C.4.

In the widely used *classical model* of power grid dynamics one neglects transient saliency and thereby the asymmetry of the rotor geometry in a salient pole machine, assuming that $x'_d \approx x'_q = x'$. This assumption simplifies the calculations, as we do not have to separate the q- and d-axis explicitly but can work with phasors. The relation of voltages and currents simplifies to

$$\underline{V}_s = \underline{E}' - \mathrm{i}x'\underline{I} \quad \Rightarrow \quad \underline{I} = \frac{\underline{E} - \underline{V}_s}{\mathrm{i}x'}\,, \tag{62}$$

where the real parts correspond to the $q-$components and imaginary parts to the d-components. Writing $\underline{E}' = E'e^{-\mathrm{i}\phi}$ and $\underline{V}_s = V_s e^{-\mathrm{i}\delta}$ the real power simplifies to

$$\tilde{P}_{\mathrm{el}} = \Re(\underline{V}_s \underline{I}^*) = \frac{E'V_s}{x'}\sin(\delta - \phi). \tag{63}$$

Finally, we recall that in the second order model the dynamics of the rotor EMFs is fully neglected. Hence, E' is set to a constant which is chosen to correspond to the steady state value when the generator provides the power $P + \mathrm{i}Q$. Then, we have to satisfy the relation

$$P + \mathrm{i}Q = \underline{V}_s \underline{I}^* = \frac{V_s^2 - \underline{V}_s \underline{E}}{\mathrm{i}x'} \tag{64}$$

which can be solved for E^2 with the result

$$E^2 = \left(\frac{Px'}{V_s}\right)^2 + \left(\frac{Qx'}{V_s} + V_s\right)^2. \tag{65}$$

6. Ohmic loads and the Kron reduction

To understand the operation and stability of extended power grids, including collective effects, we extend the model of the previous section to coupled generators. Recall that we have to specify the currents and the real power in terms of the internal EMFs in order to close the equations of motion summarized in section III.C.4. To this end, we have to model the loads and we have to describe the grid explicitly. We formulate Kirchhoff's equation in a fixed network frame of reference and work out the transformation to the reference frames of the rotating machines explicitly. For the sake of simplicity we will neglect transient saliency here, setting $x'_d = x'_q = x'$. The derivation follows the presentation by (Nishikawa and Motter, 2015), a mathematical treatment is provided in (Dörfler and Bullo, 2013).

So, assume that the generator or active nodes are labeled as $j \in \{1, \ldots, \mathtt{N}_g\}$ and the load or passive nodes are labeled as $j \in \{\mathtt{N}_g + 1, \ldots, \mathtt{N}_g + \mathtt{N}_l\}$. For the generator nodes, we have already discussed the relation between internal EMFs $\underline{E}'$ and the voltage at the system terminal end $\underline{V}$ in the previous section. The current injection from internal to terminal end at a node j is given by

$$\underline{I}_j^{\mathrm{in}} = \frac{\underline{E}'_j - \underline{V}_j}{\mathrm{i}x'_j}. \tag{66}$$

Load nodes with a given power demand $\underline{S}_j = P_j + \mathrm{i}Q_j$ are modeled by a fixed admittance to the ground $y_j^{\mathrm{ground}} = \underline{S}_j^*/V_0^2$. Then, if the voltage magnitude V_j equals the reference voltage V_0, the load nodes consume the power $\underline{V}_j \underline{I}_j^{\mathrm{in}*} = V_0\, y_j^{\mathrm{ground}*}\, V_0 = P_j + \mathrm{i}Q_j$ as desired.

For each node $j \in \{1, \ldots, \mathtt{N}_g + \mathtt{N}_l\}$ we then evaluate Kirchhoff's current law: The current inflow must equal the current flowing to the other nodes in the grid:

$$\underline{I}_j^{\mathrm{in}} = \sum_{k=1}^{\mathtt{N}_g + \mathtt{N}_l} y_{kj}(\underline{V}_j - \underline{V}_k). \tag{67}$$

We now collect all these linear relations in vectorial form, defining the vectors and matrices

$$\begin{aligned}
\underline{\boldsymbol{E}} &= (\underline{E}'_1, \ldots, \underline{E}'_{\mathtt{N}_g})^\top, \quad \underline{\boldsymbol{I}} = (\underline{I}_1^{\mathrm{in}}, \ldots, \underline{I}_{\mathtt{N}_g}^{\mathrm{in}})^\top, \\
\underline{\boldsymbol{V}}_g &= (\underline{V}_1, \ldots, \underline{V}_{\mathtt{N}_g})^\top, \quad \underline{\boldsymbol{V}}_l = (\underline{V}_{\mathtt{N}_g+1}, \ldots, \underline{V}_{\mathtt{N}_g+\mathtt{N}_l})^\top, \\
Y_i &= \mathrm{diag}\left((\mathrm{i}x'_1)^{-1}, \ldots, (\mathrm{i}x'_{\mathtt{N}_g})^{-1}\right) \\
Y_{gg}^{\mathrm{gr}} &= \mathrm{diag}\left(y_{\mathtt{N}_g+1}^{\mathrm{ground}}, \ldots, y_{\mathtt{N}_g+\mathtt{N}_l}^{\mathrm{ground}}\right).
\end{aligned} \tag{68}$$

Equation (66) and Kirchhoff's current laws for the generator and load nodes are thus condensed into the form

$$\begin{pmatrix} Y_i & -Y_i & 0 \\ -Y_i & Y_{gg} + Y_i & Y_{gl} \\ 0 & Y_{lg} & Y_{ll} + Y_{ll}^{\mathrm{gr}} \end{pmatrix} \begin{pmatrix} \underline{\boldsymbol{E}} \\ \underline{\boldsymbol{V}}_g \\ \underline{\boldsymbol{V}}_l \end{pmatrix} = \begin{pmatrix} \underline{\boldsymbol{I}} \\ 0 \\ 0 \end{pmatrix}, \tag{69}$$

where Y_{gg} , Y_{gl}, Y_{lg} and Y_{ll} are the respective partitions of the nodal admittance matrix (14). We can now gradually eliminate the network voltages, using the third row to eliminate $\underline{\boldsymbol{V}}_l$ and then the second row to eliminate the $\underline{\boldsymbol{V}}_g$. This procedure is referred to as Kron reduction, a mathematical accounting of this procedure is discussed in (Dörfler and Bullo, 2013). We finally obtain

$$\underbrace{Y'\left(1 + Y_i^{-1}Y'\right)^{-1}}_{=:Y^{\mathrm{eff}}} \underline{\boldsymbol{E}} = \underline{\boldsymbol{I}}, \tag{70}$$

where we defined the short-hand $Y' = Y_{gg} - Y_{gl}(Y_{ll} + Y_{ll}^{\mathrm{gr}})^{-1}Y_{lg}$. Equation (70) has the same structure as (15), but the reduced susceptibility matrix Y^{eff} represents an effective, not the physical network. In summary, Eq. (70) directly yields the currents and the real power acting on the machines in terms of the internal EMFs:

$$\begin{aligned}
\underline{I}_j^{\mathrm{in}} &= \sum_{k=1}^{\mathtt{N}_g} Y_{jk}^{\mathrm{eff}} \underline{E}'_k, \qquad (71) \\
P_j^{\mathrm{el}} &= \Re(\underline{V}_j \underline{I}_j^{\mathrm{in}*}) = \Re(\underline{E}'_j \underline{I}_j^{\mathrm{in}*}) = \sum_{k=1}^{\mathtt{N}_g} \Re\left(\underline{E}'_j Y_{jk}^{\mathrm{eff}*} \underline{E}'^*_k\right).
\end{aligned}$$

These quantities are given in the network frame of reference as stated above. To evaluate them for the dynamical models summarized in section III.C.4, we transfer back to the rotating frame of reference of each machine via

$$\begin{aligned}
&\underline{I}_j \text{ [network frame]} = e^{\mathrm{i}\delta_j}(I_{qj} + \mathrm{i}I_{dj}) \text{ [machine frame]} \\
&\underline{E}'_j \text{ [network frame]} = e^{\mathrm{i}\delta_j}(E'_{qj} + \mathrm{i}E'_{dj}) \text{ [machine frame]}.
\end{aligned}$$

Solving for the currents in the machine frame yields

$$I_{dj} + \mathrm{i}I_{qj} = \sum_{k=1}^{\mathtt{N}_g} Y_{jk}^{\mathrm{eff}}(E'_{qk} + \mathrm{i}E'_{dk})e^{\mathrm{i}(\delta_k - \delta_j)}, \tag{72}$$

and the real power acting on the jth machine reads

$$P_j^{\mathrm{el}} = \Re\left(\sum_{k=1}^{\mathtt{N}_g} Y_{jk}^{\mathrm{eff}*}(E'_{jk} + \mathrm{i}E'_{jk})(E'_{qk} - \mathrm{i}E'_{dk})e^{\mathrm{i}(\delta_j - \delta_k)}\right).$$

This expression simplifies considerably for the particularly important case of a second order model. Then we have $E'_{qj} = E_j = \mathit{const}$ and $E'_{dj} \equiv 0$. Writing $Y_{jk}^{\mathrm{eff}} = |Y_{jk}^{\mathrm{eff}}|e^{\mathrm{i}(\gamma_{jk}+\pi/2)}$ we obtain

$$P_j^{\mathrm{el}} = \sum_{k=1}^{\mathtt{N}_g} |Y_{jk}^{\mathrm{eff}}| E_j E_k \sin(\delta_j - \delta_k - \gamma_{jk}). \tag{73}$$

7. The structure-preserving model

In the previous section all loads were modeled as constant admittances to the ground and subsequently eliminated. Bergen and Hill (Bergen and Hill, 1981) introduced an alternative model for power grid frequency dynamics, keeping the load nodes and hence the full network structure. Generator nodes are described as in the swing equations, setting the magnitude of the EMF to a constant. The model of load nodes is based on the observation that the real power consumption typically increases with frequency, which is written in the form

$$P_j^{\mathrm{el}}(t) = P_j^{(0)} + \frac{D_j}{\omega_R}\dot{\delta}_j \quad \Rightarrow \quad \frac{D_j}{\omega_R}\dot{\delta}_j = P_j^{\mathrm{el}} - P_j^{(0)}. \tag{74}$$

We thus obtain an equation of motion for load nodes which is equivalent to the swing equation with a vanishing inertia H_j. To close the model, one then has to express the real power injections P_j^{el} at the generator and load nodes in terms of the voltage phase angles, recalling that the voltage magnitudes are assumed to be constant. This procedure, which includes the elimination of the generator terminal nodes, is described in detail in (Nishikawa and Motter, 2015). The great advantage of this approach is that the coupling in the resulting equations of motions reflects the true network structure.

8. Dynamics of power electronic inverters for renewable sources

Renewable power sources are generally *not* equivalent to synchronous machines. All photovoltaic power sources and virtually all wind turbines are connected to the grid via power electronic inverters. The transition to renewable energy supply thus fundamentally changes the dynamics of power grids. In particular, the decrease of inertia provided by conventional synchronous machines is a major challenge for grid stability (Milano *et al.*, 2018).

One generally distinguishes two modes of operation of power electronic inverters. A grid-following inverter provides a given amount of electric power adjusting to the voltage and frequency provided by the grid. Hence, the operation relies on other resources which are able to provide a stable voltage and frequency. In contrast, grid-forming inverters regulate the voltage and frequency to specific setpoints similar to a synchronous machine. Mixed modes are also possible in principle, regulating either voltage or frequency and following the other.

The development and analysis of new types of (grid-forming) inverters and inverter-based grids is a very active field of research. We thus introduce one important class, the droop-controlled inverter, following (Schiffer *et al.*, 2014). The basic state variables of such an inverter are the EMF magnitude E_j and phase angle δ_j, where j labels the different generators in the grid. The control system adjusts these state values to maintain the predefined set values of power and frequency. To this end, the control system measures the real and reactive power exchanged with the grid and compares it to predefined set values. In a simple proportional, or droop control scheme, the frequency control is proportional to the active power deviation and the voltage control is proportional to the reactive power deviation such that we obtain the equations of motion

$$\dot{\delta}_j = \omega^d - \kappa_j^{\mathrm{act}}\left(P_j^{\mathrm{mes}} - P_j^d\right), \tag{75}$$

$$T_j^V \dot{E}_j = -E_j + E_j^d - \kappa_j^{\mathrm{rec}}\left(Q_j^{\mathrm{mes}} - Q_j^d\right), \tag{76}$$

where the superscript $\cdot^{\mathrm{mes}}$ indicates the measured values of real and reactive power and the superscript $\cdot^{\mathrm{d}}$ stands for *desired* values. Naturally, the desired frequency ω^d is unique across the grid, whereas the desired voltages E_j^{d} may differ. The parameters κ_j^{act} and κ_j^{rec} are the droop gains for the frequency and voltage, respectively. The measurements are not instantaneous and characterized by a low-pass filter such that $T_j\dot{P}_j^{\mathrm{mes}} = -P_j^{\mathrm{mes}} + P_j^{\mathrm{el}}$ and $T_j\dot{Q}_j^{\mathrm{mes}} = -Q_j^{\mathrm{mes}} + Q_j^{\mathrm{el}}$. The recovery time of voltage dynamics is typically much lower than the time constant T_j of the low-pass filter. We thus simplify the model by setting $T_j^V = 0$, obtaining (Schiffer *et al.*, 2014)

$$\dot{\delta}_j = \omega_j, \tag{77}$$

$$T_j\dot{\omega}_j = -\omega_j + \omega^{\mathrm{d}} - \kappa_j^{\mathrm{act}}\left(P_j^{\mathrm{el}} - P_j^{\mathrm{d}}\right), \tag{78}$$

$$T_j\dot{E}_j = -E_j + E_j^{\mathrm{d}} - \kappa_j^{\mathrm{rec}}\left(Q_j^{\mathrm{el}} - Q_j^{\mathrm{d}}\right). \tag{79}$$

The real and reactive power exchanged with the grid, P_j^{el} and Q_j^{el}, depend on the state of all elements in the grid. To close the equations of motion, one thus has to specify the network equations. Modelling all loads by constant impedances to the ground as in section III.C.6, we find

$$P_j^{\mathrm{el}} + \mathrm{i}Q_j^{\mathrm{el}} = \sum_{k=1}^{\mathtt{N}_g} \underline{E}'_j Y_{jk}^{\mathrm{eff}*} \underline{E}_k^{'*}, \tag{80}$$

where $\underline{E}_j = E_j e^{\mathrm{i}\delta_j}$ (cf. Eq. (71)).

9. Aggregated dynamical model

The classical model describes the dynamics of power systems as coupled second order rotators with each node representing one synchronous generator. Notably, similar equations of motion emerge on much coarser spatial scales (Filatrella *et al.*, 2008; Joe H. Chow (Ed.), 2013; You *et al.*, 2004; Zhang *et al.*, 1997), emphasizing the generality of the coupled rotator model.

The dynamical model introduced in (Filatrella *et al.*, 2008) considers the aggregated dynamics of *regions* labeled by $n \in \{1, \dots, \mathtt{N}\}$. If the internal coupling is sufficiently strong, we take the phase angle to be constant throughout the region. Again, we measure the phase and frequency relative to a frame rotating at reference grid frequency ω_R writing $\phi_n(t) = \omega_R t + \delta_n(t)$. The equations of motion for the $\delta_n(t)$ are obtained from energy conservation. Each region stores kinetic energy in the rotation of all synchronous machines,

$$E_n^{\text{kin}} = \frac{J_n}{2}(\dot{\phi})^2, \tag{81}$$

where J_n is the aggregated moment of inertia. At each node a power P_n^{in} is injected by generators or withdrawn by consumers and some energy will be dissipated at a rate $P_n^{\text{diss}} = \eta_n(\dot{\phi}_n)^2$. Assuming a constant voltage magnitude, the real power transmitted from a region n to a region m is determined by the phase difference

$$P_{n\to m}^{\text{trans}} = K_{nm}\sin(\delta_n - \delta_m), \tag{82}$$

neglecting Ohmic losses. K_{nm} is an aggregated quantity, summing over all lines connecting the two regions n and m. Then, the energy conservation for region n gives

$$P_n^{\text{in}} = \frac{dE_n^{\text{kin}}}{dt} + P_n^{\text{diss}} + \sum_m P_{n\to m}\,. \tag{83}$$

Noting that $|\dot{\delta}| \ll \omega_R$ in the vicinity of the normal operation, we simplify the expression for the change of the kinetic energy, $dE_n^{\text{kin}}/dt \approx \omega_R J_n \ddot{\delta}_n$, and the dissipated power, $P_n^{\text{diss}} \approx \eta\omega_R^2 + 2\eta_n\omega_R\dot{\delta}_n$. Substituting these results into the energy conservation law (83) then directly yields the equations of motion

$$\omega_R J_n\ddot{\delta}_n + 2\omega_R\eta_n\dot{\delta}_n = P_n^{\text{eff}} - \sum_m K_{nm}\sin(\delta_n - \delta_m), \tag{84}$$

where $P_n^{\text{eff}} = P_n^{\text{in}} - \omega_R^2\eta_n$. Eqs. (84) have the same structure as the classical second order model, but describe the dynamics on a coarser level. The above derivation is based on elementary energetic arguments, but similar results can also be obtained via model reduction (Joe H. Chow (Ed.), 2013; You *et al.*, 2004; Zhang *et al.*, 1997). This emphasizes the generic nature of coupled rotator models in network science.

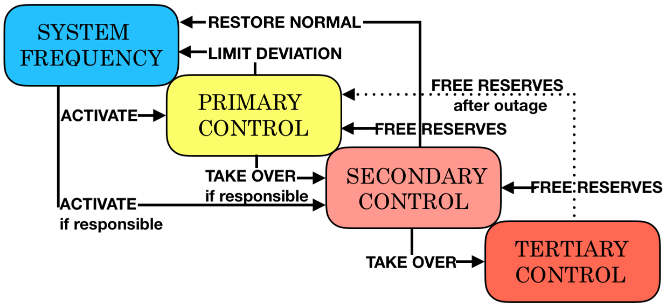

FIG. 4 Load Frequency Control-Scheme according to ENTSO-E (UCTE Operations Handbook, 2009).

D. Load frequency control

A power grid itself does not store energy, so the generated power must match the demand and the losses at all times. A hierarchy of control systems exists to maintain this balance, which we introduce starting from the swing equation (47). As before, we use a rotating frame of reference, such that $\omega_i = \dot{\delta}_i$ denotes the deviation from the nominal grid frequency ω_R,

$$J_i\omega_R\dot{\omega}_i + D_i\omega_R\omega_i = P_i^{\text{mech}} - P_i^{\text{el}}\,. \tag{85}$$

In normal operation, all machines $i \in \{1, \dots, \mathtt{N}\}$ in a grid run in synchrony at the same frequency, a fact that we will discuss in more detail in section VI. We thus focus on the bulk frequency and define

$$\bar{\omega}(t) = \bar{J}^{-1}\sum_{i=1}^{\mathtt{N}} J_i\omega_R\omega_i(t) \quad \text{with } \bar{J} = \sum_{i=1}^{\mathtt{N}} J_i\omega_R. \tag{86}$$

In many studies, the damping is assumed to be proportional to the inertia of a machines (cf. the supplement of ref. (Motter *et al.*, 2013)). Setting $D_i = \eta J_i$ we obtain

$$\bar{J}\dot{\bar{\omega}} + \eta\bar{J}\bar{\omega} = \Delta P, \tag{87}$$

where $\Delta P = \sum_i P_i^{\text{mech}} - P_i^{\text{el}}$ is the power balance in the entire grid. We thus see that the power balance directly drives the dynamics of the bulk: A scarcity of generation leads to a decrease, while an overgeneration leads to an increase of the frequency. As the frequency can be measured rather easily, it is used to control the generation.

Different control mechanisms are distinguished according to different time scales they act on and different purposes they serve. (i) The *momentary reserve* is provided by the inertia of synchronous machines. The higher the inertia $\bar{J}$, the slower the grid frequency reacts to a power imbalance. This reaction rate is referred to as the *Rate of Change of Frequency (RoCoF)* in the engineering literature. Notably, renewable power sources with power electronic inverters have no intrinsic inertia, such that frequency stability is an important challenge in the energy transition (Milano *et al.*, 2018).

(ii) Next, the power imbalance is reduced by increasing or decreasing the generation of specific control power plants, or, more recently, battery electric storage systems (Fleer and Stenzel, 2016). According to the guidelines of the ENTSO-E (UCTE Operations Handbook, 2009), primary control is activated as soon as the frequency leaves a small dead band around ω_R and must be fully available within 30 seconds. Up to the dead band, the power is adapted proportional to the frequency deviation,

$$P_{\mathrm{PRL},i}(t) = -\kappa_i \omega_i, \tag{88}$$

where the parameter κ_i describes the sensitivity of primary control for the grid area i. Primary control stabilizes the frequency, but does not restore the nominal grid frequency, which can be seen by adding primary control to the equation of motion (87). For a constant power imbalance ΔP and a single area we find the fixed point

$$\bar{\omega} = \frac{\Delta P}{\kappa + \eta \bar{J}} \,. \tag{89}$$

Damping terms $\propto D_i$ in Eq. (85) affect frequency dynamics similar to primary control $\propto \kappa_i$, which is often directly included in the swing equation (cf. Sec. III.C.1).

(iii) Secondary control restores the nominal grid frequency ω_R and reduces unscheduled power flows between different grid areas on time scale of minutes. Control power plants adapt their generation according a proportional-integral (PI) law (Böttcher *et al.*, 2020),

$$P_{\mathrm{SRL},i}(t) = -\left(\kappa_P G_i(t-\tau) + \kappa_I \int_{-\infty}^{t-\tau} G_i(t')dt' \right), \tag{90}$$

with κ_P and κ_I being tunable gain factors. The local area-control-error G_i is a measure of the power that is missing in area i. It is determined by the difference between the expected primary control power and the deviations ΔF_i of the power flow to neighbouring control areas as $G_i = \kappa_i \omega_i - \Delta F_i$. Note, that while the PI controller is linear, the local area-control error G_i depends nonlinearly on the system state. The finite time delay τ in the control (90) results from the time required for the measurement of G_i, communication and the adaption of the control power generation. The secondary control requires to measure local area-control-errors G_i with a cycle time between 2 to 5 seconds (UCTE Operations Handbook, 2009). The delay time τ can therefore be expected to be of similar magnitude, but may vary in different control areas and with time (Böttcher *et al.*, 2020).

(iv) Tertiary control power is invoked on even longer timescales. In Europe, the tertiary control power must be activated within at most 15 minutes. Tertiary control is operated partly manually and mostly used to restore the automatic control reserve.

IV. POWER GRID TOPOLOGIES AND DATASETS

The previous sections introduced the various components of power grids, in particular power lines and various producers and consumers at the nodes. In order to derive a model of a complete power grid, the missing ingredient is the topology, that is, how these components are connected. Besides studying concrete examples of real power grids, it is also desirable to obtain plausible synthetic networks, to allow a more systematic study of the impact of topological features on dynamical properties.

A. General aspects

Large power grids, especially at the continental scale, operate at many different voltage levels. Long-range transmission is achieved through high voltage connections in order to minimize losses. In Central Europe for example, the transmission grid operates at 220 kV and 380 kV. The regional distribution is then achieved by grids at successively lower voltages, connected to the high voltage transmission grid at substations (transformers). Typical voltage levels in Europe range from high voltages (60 kV, 110 kV) over medium voltages (3-30 kV) to low voltages (230V, 380V). Typical line parameters for transmission grids are summarized in table I.

Grids at these different voltage levels are constructed in very different ways and with different trade-offs and goals in mind and thus exhibit different network topologies. A low voltage distribution grid is typically organized as a tree graph, in this context called a *radial design.* While loops might physically exist, there often is a switch interrupting them. We remark that only if a line fails, the loop is closed to resume supply downstream of the failure.

High voltage transmission grids require uninterrupted operation even in cases where a line fails ($N-1$ criterion). This implies that the network is meshed, i.e. it contains loops. An example of such a topology is shown in Fig. 5. Medium voltage grids often fall in an intermediate regime, with varying amounts of meshing.

From a network science perspective a notable aspect of power grids is that they are geographically embedded. That is, nodes and lines have geographical locations and lengths. Line crossings are possible, but are rare. These aspects are reflected in the connectivity or topology of the network, putting them in a different class than the ensembles typically studied in network science.

Further, as infrastructure has costs, they typically also contain as few lines as possible. As a consequence, power grids are typically sparse. The observed average degree for transmission grids falls between 2 and 5, and the degree distribution peaks between two and three, and has an exponential tail (Solé *et al.*, 2008; Wang *et al.*, 2010).

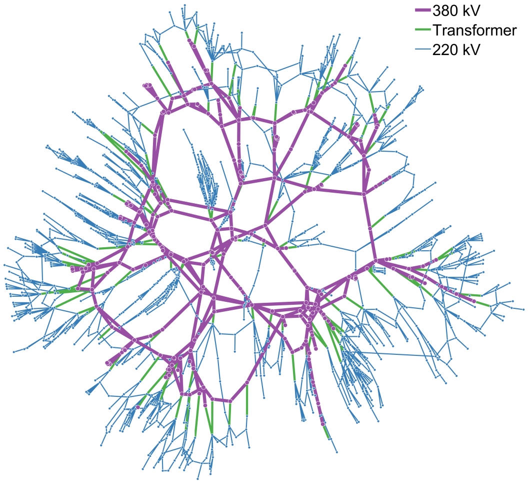

FIG. 5 Topology of a high voltage power grid (Coffrin *et al.*, 2014), visualized using the methods of (Cuffe and Keane, 2015), by Paul Cuffe, CC BY-SA 4.0, Wikimedia.

f_n [Hz]	V_n [kV]	r [Ω/km]	x [Ω/km]	b_c [μS/km]
50 (UK)	400	0.018	0.265	5.36
	230	0.05	0.488	3.371
50 (DE)	380	0.03	0.246	4.335
	220	0.06	0.301	3.927
60 (USA)	345	0.037	0.367	4.518
	500	0.028	0.325	5.2
	765	0.012	0.329	4.978

TABLE I Typical parameters of overhead transmission lines at different voltage levels for the United Kingdom and the USA according to (Kundur, 1994; Machowski *et al.*, 2008) and for Germany according to (Oeding and Oswald, 2016). Ohmic resistance, susceptance and charging capacity are proportional to the length of the line and are given per km.

B. Network ensembles and synthetic grid models

The statistical physics of networks often considers ensembles of networks to map out typical topological properties and to provide a reference class for actual real-world data sets. Power grids do not fully resemble any of these common network ensembles. In particular they are not well captured by small-world networks (Cotilla-Sanchez *et al.*, 2012). Though the clustering coefficient is similarly high, there is a much more pronounced connectivity at large scales. A Watts-Strogatz small-world network of such a low degree would very likely end up being disconnected for moderately sized networks, and the non-local links in power grids tend to be much more clustered (Wang *et al.*, 2010).

In order to capture the full topological structure of power grids, we need to define novel network ensembles: probability distributions on the space of networks that capture the notion of, what looks like a power grid and what does not. This is typically done by specifying a random process that produces networks, either by rewiring links or by iteratively growing networks. Given such an embedded topology, typical power line parameters can then be used to derive the power grids properties I.

In (Wang *et al.*, 2010) a rewiring based process was proposed with the aim to stay close in spirit to the construction of small world networks, while taking some specific identified properties of power grids into account. In contrast, growth based models, starting with (Schultz *et al.*, 2014b) grow the grid with random node placements and new connections. The model of (Schultz *et al.*, 2014b) mimics the trade off between global resilience and economy in the growth process, and is able to recreate the exponential degree distribution. Having these trade-offs explicitly allows, for example, to study trade-offs of dynamic and structural stability in (Plietzsch *et al.*, 2016). A growth model for hierarchical networks is proposed and analyzed in (Ódor and Hartmann, 2018).

Reference (Soltan and Zussman, 2016) considers node placement in addition to line generation. It considers average path length, clustering coefficient, the slope of node degree distributions and the line length distributions and shows that their algorithm matches those in various North American power grids.

In these models the growth process makes use of topological and embedding information, but does not consider the resulting energy flows in the growth stage. Birchfield *et al.* (2017, 2018) add consideration of power flows in DC approximation and voltage profiles to the iterative growth of synthetic grids. In (Soltan *et al.*, 2018) the growth process is fitted by using a Gaussian mixture model. Espejo *et al.* (2018) present a model that focuses instead on historical plausibility of the growth process and economy vs. robustness trade-offs.

Besides generating topologies from scratch, it is also possible to take an existing topology and vary it while keeping many aspects of it fixed. Such surrogate ensembles for spatial infrastructure networks were described in (Wiedermann *et al.*, 2016). A difficult open question is to find a fully satisfactory model for the co-generation of a variety of networks (Hackl and Adey, 2018), or hierarchies of networks (Schultz *et al.*, 2016).

C. Network datasets

The availability of real grid data is limited. Thus, a variety of test cases has been compiled for scientific use. Some are based on available data of real world grids. Some are synthetic, trying to mimic structural properties of real-world grids. In the following, we list resources which provide grid data, without claim of completeness.

- The classical IEEE test cases are probably the most heavily studied power grids at all, some having been implemented decades ago. The datasets are partly synthetic and partly derived from real grids and can be obtained at the repository (Christie, 1999).

- Several online repositories have been created in recent years to provide larger, more diverse and more recent test cases, focusing on transmission grids (Amro M. Farid et al., 2019; Birchfield, 2016; Pacific Northwest National Laboratory and National Rural Electric Cooperative Association, 2017) or distribution grids ('feeder') (K. P. Schneider et al., 1991; Kavasseri and Ababei, 2021). In addition, several papers review such repositories and the methodologies, see e.g. (Birchfield *et al.*, 2017; Coffrin *et al.*, 2014; Schneider *et al.*, 2018). Again these repositories include both synthetic grids and approximate models of real grids, with a focus on Northern America. Large test grids with properties typical for European grids have been provided by the Pegase project (Villella *et al.*, 2012).
- The IEEE and Pegase test grids are included with others in the latest version of the popular software package Matpower (Zimmerman *et al.*, 2011).
- Many test cases are restricted to static properties and do not include the parametrization necessary for dynamic simulations. In order to analyze the dynamics of these systems some heuristic assumptions about present or future parameters are necessary. Realistic dynamic test cases mostly come in form of small synthetic test cases developed by IEEE, that can be found in repositories (Amro M. Farid et al., 2019; Pacific Northwest National Laboratory and National Rural Electric Cooperative Association, 2017). The European Network of Transmission System Operators for Electricity (ENTSO-E) provides semi-synthetic grid models mimicking the European grid (Semerow *et al.*, 2015), but access is limited. A notable exception is the synthetic model of the North Eastern US published by (Birchfield, 2016), which includes a 25.000 node dynamic system, validated in the sense of (Xu *et al.*, 2018). A heuristic dynamical parametrization of the ENTSO-E based system (Wiegmans, 2016) was recently published in (Pagnier and Jacquod, 2019c).
- Recently, several initiatives started to map out power grids from publicly available data. A model of the German power grid was extracted from Open Street Maps (Medjroubi *et al.*, 2015), and a model of the European grid was extracted from the ENTSO-E interactive grid map (Wiegmans, 2016). A variety of related datasets can be found on the community websites (Open energy Modelling Initiative, 2017; Open Power Systems Data, 2017). A collection of grid frequency time series has been published in (Gorjão *et al.*, 2020b).

V. DYNAMICS OF ELEMENTARY NETWORKS AND BUILDING BLOCKS

We introduce basic aspects of power system dynamics and stability for an elementary grid containing one transmission line. We first consider its static operation and its limitations before we turn to the dynamic stability.

A. Static solutions and voltage stability

We consider the steady state of an elementary circuit with one load node and one generator connected by a single transmission line to understand which factors limit the power transmission in different types of grids. The generator s is treated as a slack node, so that $V_s = 1$ and $\delta_s = 0$ are fixed (cf. Sec. III.A.3). Most load nodes draw reactive power Q_n at a fixed ratio to the real power, which is commonly specified in terms of the *power factor* $\cos(\vartheta)$ defined via the relations $P_n = \sqrt{P_n^2 + Q_n^2}\cos(\vartheta)$ and $Q_n = \sqrt{P_n^2 + Q_n^2}\sin(\vartheta)$. We here analyze the operation as a function of the real power demand $P_n < 0$.

To obtain the voltage magnitude V_n and phase angle δ_n at the load node, we then have to solve the AC load flow Eqs. (25), which are rewritten using the addition theorems of the sine and cosine

$$\begin{aligned} P_n &= G_{nn} V_n^2 + V_n V_s \sqrt{B_{ns}^2 + G_{ns}^2}\sin(\delta_n - \gamma_{ns}) \\ Q_n &= -B_{nn} V_n^2 + V_n V_s \sqrt{B_{ns}^2 + G_{ns}^2}\cos(\delta_n - \gamma_{ns}), \end{aligned} \quad (91)$$

where the angle γ_{ns} is defined via

$$\cos(\gamma_{ns}) = \frac{-B_{ns}}{\sqrt{B_{ns}^2 + G_{ns}^2}}, \quad \sin(\gamma_{ns}) = \frac{-G_{ns}}{\sqrt{B_{ns}^2 + G_{ns}^2}}.$$

We can then separate the equation for the voltage magnitude using $\sin^2 + \cos^2 = 1$ which yields

$$\begin{aligned} 0 &= (B_{nn}^2 + G_{nn}^2) V_n^4 + (P_n^2 + Q_n^2) \\ &\quad - (B_{ns}^2 V_s^2 + G_{ns}^2 V_s^2 - 2B_{nn} Q_n + 2G_{nn} P_n) V_n^2, \end{aligned} \quad (92)$$

which is easily solved for V_n^2. The phase angle can then be obtained by solving one of the Eqs. (91).

To understand the behavior of the system and the limitations to power transmission in more detail, we plot voltage V_n as function of the real power demand $|P_n|$ in Fig. 6 (a) for different values of the power factor. This plot is often referred to as the 'nose curve' in power engineering (Machowski *et al.*, 2008). First, one observes that the quadratic Eq. (92) can have two solutions, where only the branch with the higher magnitude is relevant as the other branch is unstable. Second, power transmission is generally limited. Physical solutions of Eq. (92) exist only if the real power demand does not exceed the limit

$$P_n^2 \leq \frac{1}{4} B_{ns}^2 V_s^4 + B_{ns} V_s^2 Q_n \, , \quad (93)$$

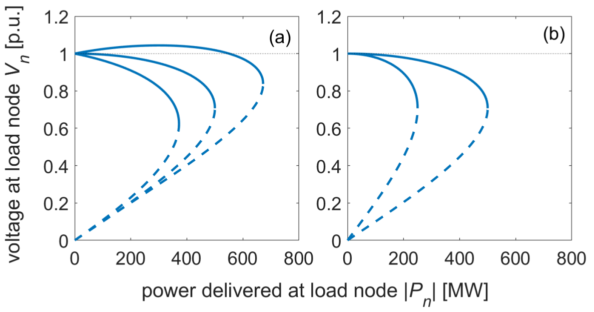

FIG. 6 The nose curve. (a) Voltage at the load node as function of transmitted power for three different power factors: $\tan(\vartheta) = +0.3, 0, -0.3$ (from left to right). (b) for $\tan(\vartheta) = 0$ in the initial state (right) and after half of the connectivity is lost, i.e. B_{ns} is halved (left). Parameters are $S_{\text{base}} = 100$ MW, $V_s = 1$ pu and $B_{ns} = 10$ pu. Solid (dashed) lines indicate stable (unstable) solutions of the load-flow equations.

which depends on the reactive power. The limit as well as the voltage magnitude V_n is lower when the load draws reactive power ($Q_n > 0$, $\tan(\vartheta) > 0$). However, if the load node supplies reactive power instead ($Q_n < 0$, $\tan(\vartheta) < 0$), the voltage at the load node can be even larger than V_s and the transmittable real power is strongly enhanced. Grid operators hence aim to keep $\tan(\vartheta)$ small or even negative by supplying reactive power near the loads – a procedure referred to as 'reactive power compensation'

Let us further consider how a 'voltage instability' can arise in elementary power grids. Let us assume that two parallel transmission lines exist and that one of them is lost in a contingency situation. As a consequence, the effective susceptance B_{ns} is halved and the nose curve contracts as shown in Fig. 6 (b). Further effects depend on the grid loading. If the real power demand $|P_n|$ is not too high (e.g. 200 MW in the figure), a solution of the power flow equations still exists, albeit at a lower voltage. The consumers will thus experience a rapid drop of the voltage level. However, if the real power demand is too large (e.g. 300 MW in the figure), no static equilibrium solution exists any more and a voltage collapse emerges in which voltages decline as governed by the power system dynamics. A comprehensive analysis of voltage stability in power grids can be found in the text book (Van Cutsem and Vournas, 2007).

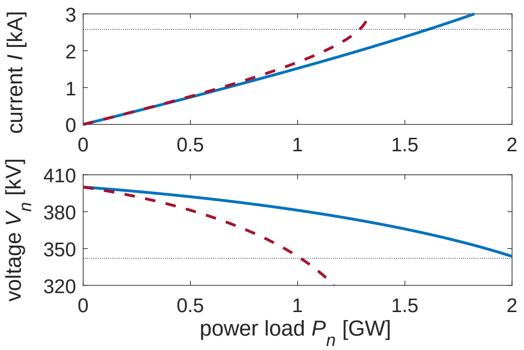

FIG. 7 Factors limiting real power transmission in AC power grids for two different characteristic cases (blue: Short line with $l = 100$ km, dashed red: long line with $l = 200$ km). We consider a single transmission line connecting one power plant to a substation. Shown is the current $|I|$, the voltage magnitude $|V_n|$ and the voltage angle δ_n at the load node as a function of the real power load P_n. The dotted line shows the limits I_{th} and V_{lim} for the current and the voltage.

B. Flow and voltage limits

Power transmission in current highest-voltage grids is typically limited by other factors than the ones discussed above. Most grids are constantly monitored and thoroughly regulated. Security limits have been formulated for current and voltage (see, e.g., (European Network of Transmission System Operators for Electricity, 2004)) and emergency shutdowns are carried out when these limits are violated. Hence, the physical limits of power transmission are rarely met during normal operation.

In particular, extreme currents can lead to an Ohmic heating and eventually to a dangerous bending of overhead transmission lines due to thermal elongation. During the 2003 power outages in North America (U.S.-Canada Power System Outage Task Force, 2014) and Italy (Union for the Co-ordination of Transmission of Electricity, 2004) transmission lines hit trees leading to a short-circuit fault. Hence, grid operators typically impose 'thermal limits' for the currents and overloaded lines switch off automatically. Similarly, upper and lower limits for the voltage magnitude are imposed to guarantee power quality and avoid the danger of a complete voltage sack.

To see how these regulations limit power transmission in highest-voltage grids, we solve the load flow equations (91) as a function of P_n assuming a fixed power factor, which is set to a typical value of $\cos(\vartheta) = 0.95$ with $\vartheta > 0$. We use typical parameters for a 380 kV transmission line in Western Europe with $r/l = 0.03\,\Omega/\text{km}$ and $x/l = 0.246\,\Omega/\text{km}$ and a thermal limiting current of $I_{\text{th}} = 2.58$ kA (Oeding and Oswald, 2016), l being the length of the line. We use the notation of the previous section, but give all quantities in physical units for better accessibility.

Figure 7 shows the results for two characteristic cases. First we consider a transmission line of length of $l = 100$ km connecting the load node and a generator node, which has a fixed voltage magnitude $V_g = 400$ kV slightly above the nominal voltage level of 380 kV. The current

$$|I_{ng}| = \left| \frac{|V_n| e^{\mathrm{i}\delta_n} - |V_g|}{r + \mathrm{i}x} \right| \tag{94}$$

increases approximately linear with transmitted power. For $P_n \geq 1.61$ GW the current exceeds the thermal line limit, which would lead to emergency measures, whereas the voltage magnitude stays well above the lower limit of $V_{\rm lim} = 0.9 \times 380$ kV. This illustrates that in densely populated areas with short lines mainly the thermal limit for the current limits the operation of a transmission line. In fact we find a good estimate for the maximum transmittable real power by

$$P_{\rm max} \approx 3 \frac{380\,{\rm kV}}{\sqrt{3}} \times I_{\rm th} = 1.698\,{\rm GW}. \qquad (95)$$

Voltage stability can be an issue if generators are located far away from loads. Fig. 7 shows the current and voltage at the load node for a longer line with $l = 200$ km. The voltage limit $V_{\rm lim}$ is hit already for $P_n \geq 1.01$ GW, where the current is still well below the thermal limit.

Voltage limit violations can be handled to some extend using reactive power compensation as discussed in the previous section. Decreasing the power angle ϑ at the load node allows for a higher power transmission. In contrast, the current limit represents a more severe limitation. A rather simple way to extend power transmission is dynamic line rating, where the thermal limiting current $I_{\rm th}$ is adapted to the ambient conditions (Douglass and Edris, 1996). On cold, windy days a higher current is acceptable without risking an overheating.

C. Dynamic stability

1. Local stability of a single generator

We now turn to the question of dynamical stability, starting with the most elementary setup: a single generator coupled to an infinite grid. The grid is assumed to be so large that it is not affected by generator dynamics, such that its voltage magnitude V and phase angle ϕ are fixed. We here consider the question of angular stability and thus assume that the generator voltage is constant at the steady state value E°. If the phenomenon of voltage collapse occurs, voltages drop dynamically such that a more refined treatment is necessary.

Assuming a lossless connection of the machine to the grid with the susceptance x, the real power flow from the machine to the grid is given by $P_{\rm el} = K \sin(\delta - \phi)$ and the swing Eq. (49) reads

$$\frac{2H}{\omega_R} \ddot{\delta} + D \dot{\delta} = P_{\rm mech} - K \sin(\delta - \phi), \qquad (96)$$

where $K = V E^\circ / x$ is an effective coupling strength. In normal operation the machine rotates with the frequency ω_R and a fixed phase difference to the grid to supply a constant real power. Hence we are interested in the *fixed points* of the Eq. (96) given by

$$\delta^\circ = \phi \pm \arcsin\left(P_{\rm mech}/K\right). \qquad (97)$$

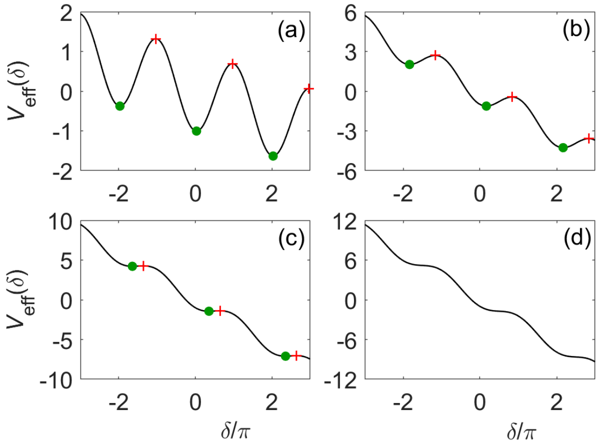

FIG. 8 The tilted washboard potential (98) as a mechanical analog to the dynamics of a single generator in the 2nd order model for (a) $P_{\rm mech} = 0.1\,K$, (b) $P_{\rm mech} = 0.5\,K$, (c) $P_{\rm mech} = 0.9\,K$, (d) $P_{\rm mech} = 1.1\,K$. The potential $\mathcal{V}_{\rm eff}$ is given in units of K. Green disk indicate stable fixed points, red crosses indicate saddle points.

One finds that the +-solution is linearly stable, while the other branch is unstable. The solutions vanish in a saddle node on a circle-bifurcation when $P_{\rm mech} = P_{\rm crit} = K$. Hence, the power the machine can receive and transmit to the grid is limited to a maximum value of $P_{\rm crit}$.

The nature of this bifurcation becomes more obvious by a mechanical analog. Consider a point particle with effective mass $m_{\rm eff} = 2H/\omega_R$ and friction coefficient $\eta = D$ moving in a *tilted washboard potential*

$$\mathcal{V}_{\rm eff}(\delta) = -P_{\rm mech}\delta - K\cos(\delta - \phi), \qquad (98)$$

where δ denotes the particle position. Then, Newton's equation for the particle, $m_{\rm eff}\ddot{\delta} = -\eta\dot{\delta} - \partial\mathcal{V}_{\rm eff}/\partial\delta$, is equivalent to the swing Eq. (96). The tilted washboard potential is shown in Fig. 8 for different values of tilting $P_{\rm mech}$. For low tilting, stable/unstable fixed points exist in the local minima/maxima of the potential (green and red dots). As the tilting increases, minima and maxima approach each other and finally vanish for $P_{\rm mech} > P_{\rm crit}$. The tilted washboard potential has been studied in great detail in statistical physics, in particular in the presence of noise, see (Risken, 1996) and references therein.

2. Bifurcations

To obtain a comprehensive understanding of the dynamics of a single generator, we also analyze its *global stability* properties. Given an initial state $\delta(0), \dot{\delta}(0)$, what happens for long times? Does the generator relax to the stable fixed point discussed above?

A global phase space portrait of the single machine system is shown in Fig. 9 for different values for $P_{\rm mech}/K$. One observes that in most cases a limit cycle exists, which

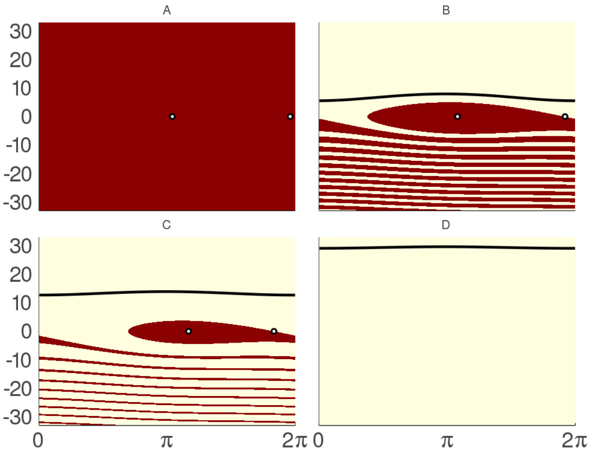

FIG. 9 Basin of attraction (red) of the stable fixed point of Eq. (96), in the δ - $\dot\delta$ plane. Parameters are $\frac{2H}{\omega_R} = 1$, $D = 0.3$, $K = 8$ and A) $P_{\rm mech} = 1$, B) $P_{\rm mech} = 2$, C) $P_{\rm mech} = 4$, D) $P_{\rm mech} = 9$. The white dots are the stable and unstable fix points. The black line gives the limit cycle.

corresponds to a desynchronized generator. The generator cannot exchange real power with the grid in this state as $P_{\rm el} = K\sin(\delta - \phi)$ is oscillating and averages out to zero. The mechanical input power accelerates the generator until this input is balanced by the damping such that it has a higher frequency than the grid, $\dot\delta > 0$.

We thus find three parameter regions with different global stability properties, cf. Figs. 9 and 10. For $P_{\rm mech}/K > 1$ no fixed point exists and the system will always converge to the limit cycle. If $P_{\rm mech}/K$ is small or the damping η is large, the system is globally stable: It converges to the attractive fixed point for almost all initial states. In the remaining part of the parameter space the fixed points and the limit cycle coexist such that the long term dynamics depends on the initial state.

An analytical approximation for the border between the globally stable and the coexistence regime can be obtained in the low-friction limit using Lyapunov's second method (Manik *et al.*, 2014; Parks, 1992; Risken, 1996). We define an energy functional $\mathcal{E} = \frac{m_{\rm eff}(\dot\delta)^2}{2} - K\cos(\delta)$, setting $\phi = 0$ for the sake of simplicity. Using the equation of motion for δ, we obtain

$$\frac{d\mathcal{E}}{dt} = m_{\rm eff}\ddot\delta\dot\delta + K\sin(\delta)\dot\delta = P_{\rm mech}\dot\delta - \eta(\dot\delta)^2. \tag{99}$$

If $\mathcal{E}$ decreases on average for all initial conditions, the system is in the globally stable regime. The condition for the border between the globally stable and the coexistence regime is therefore obtained by setting $\overline{d\mathcal{E}/dt}^T = 0$, where the bar denotes the average over one period T. Evaluating this condition yields

$$P_{\rm mech}\overline{\dot\delta}^T = \eta\overline{(\dot\delta)^2}^T. \tag{100}$$

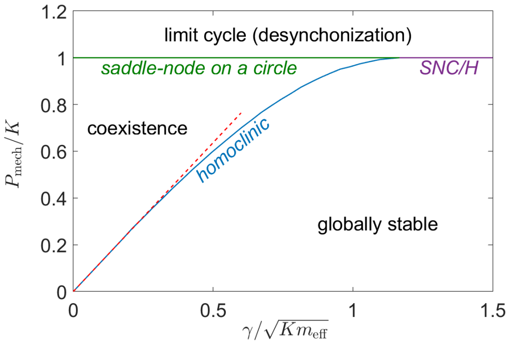

FIG. 10 Stability map of a single generator coupled to an infinite grid in the 2nd order model. Three different parameter regions exist: A globally stable fixed point, a globally attractive limit cycle and a region of coexistence of fixed point and limit cycle. Bifurcations between these regions are shown as colored lines. The red dashed line is the approximation (102) for low friction. See (Manik *et al.*, 2014; Risken, 1996) for a more detailed analysis.

We can now calculate $\overline{\dot\delta}^T = 2\pi/T$ and

$$\begin{aligned}\overline{(\dot\delta)^2}^T &= \frac{1}{T}\int_0^T (\dot\delta)^2 dt = \frac{1}{T}\int_{-\pi}^{\pi}\dot\delta d\delta \\ &= \frac{1}{T}\int_{-\pi}^{\pi}\sqrt{\frac{2}{m_{\rm eff}}}\sqrt{\mathcal{E}(\delta,\dot\delta) + K\cos(x)}\, d\delta. \end{aligned}\tag{101}$$

At the bifurcation, when a globally stable fixed point loses stability, there is a trajectory which satisfies $\dot\delta = 0$ at each successive peak of the potential landscape. This trajectory has $\mathcal{E}_{\rm peak} = K$, which can be assumed to be constant in the low friction limit. Replacing $\mathcal{E}(\delta,\dot\delta) \approx K$, the integral in (101) can be evaluated in closed form and the border between the globally stable and the coexistence region (100) is given by

$$P_{\rm mech} = \frac{4\eta\sqrt{K}}{\pi\sqrt{m_{\rm eff}}}. \tag{102}$$

This approximation matches the results from a direct numerical evaluation for small values of η as shown in Fig. 10. For large values of η it slightly overestimates the globally stable parameter region.

3. Probabilistic stability measures

Elementary systems allow for a comprehensive understanding of the bifurcation structure and global stability. However, this approach is no longer feasible for high-dimensional networked systems, such that more versatile methods are needed. Recently, probabilistic approaches have gained strong interest (Menck *et al.*, 2013). For instance, one can quantify the stability of a dynamical system by the probability of returning to the desired fixed point after a random perturbation. The set of all initial states guaranteeing convergence, the basin of attraction, is shown in Fig. 9 for a single generator and different system parameters. While the geometry of the basin can be rather intricate in higher dimensions, its size is easy to measure by randomly drawing a sufficient number of initial states from a predefined set $\mathcal{A}$ and numerically simulating their dynamics. Then, it is the same as Monte-Carlo integration of the indicator function $1_{\mathcal{B}}$ on the basin of attraction:

$$\hat{\mathcal{P}} = \mathcal{P}(x(\infty) = x^*|x(0) \in \mathcal{A}) = \frac{1}{|\mathcal{A}|}\int_{\mathcal{A}} 1_{\mathcal{B}}(x)dx. \quad (103)$$

Different aspects of stability can be understood by choosing an appropriate set $\mathcal{A}$. For instance, restricting perturbations to a single node reveals weak spots in the grid (Menck *et al.*, 2014).

The process of sampling such a probability is a Bernoulli process. Its sampling uncertainty decreases with the number of samples N, which is asymptotically given by the binomial confidence interval

$$\hat{\mathcal{P}} \pm \sqrt{\hat{\mathcal{P}}(1-\hat{\mathcal{P}})/N}\ . \quad (104)$$

though better estimates are possible for small values of N (Agresti and Coull, 1998). Most importantly, the number of samples needed does not increase with the dimension of the problem, whereas the individual samples are typically more expensive to obtain.

The asymptotic convergence to a fixed point is an important aspect of stability, but it is not sufficient in the context of power grids. One can generalize the current approach, requiring that a trajectory does not exceed certain operational limits, or equivalently, that it does not not leave a 'survival' region $\mathcal{S}$. This leads to the definition of the survivability (Hellmann *et al.*, 2016)

$$\mathcal{P}(x(t) \in \mathcal{S}\ \forall\ t|x(0) \in \mathcal{A}). \quad (105)$$

Survivability requires the specification of a survival region $\mathcal{S}$, as shown in Fig. 11 for a single generator, assuming that the survival region is given by $|\dot{\delta}| \leq \pm 5\,\mathrm{rad}/s$. This assumption is useful in the study of power grids, as generators have many protection circuits, that would switch them off to avoid mechanical damage. Probabilistic measures have also been generalized to cover the case of repeated perturbations and stochastic systems (Lindner and Hellmann, 2019; Schultz *et al.*, 2018). Furthermore, the uniform sampling from the set $\mathcal{A}$ can be replaced by more general distributions of initial states.

4. Stochastic stability

Up to now, we have analyzed the stability of the swing equation for fixed system parameters. But real-world systems will typically face disturbances and noise. How does this affect the stability of the system?

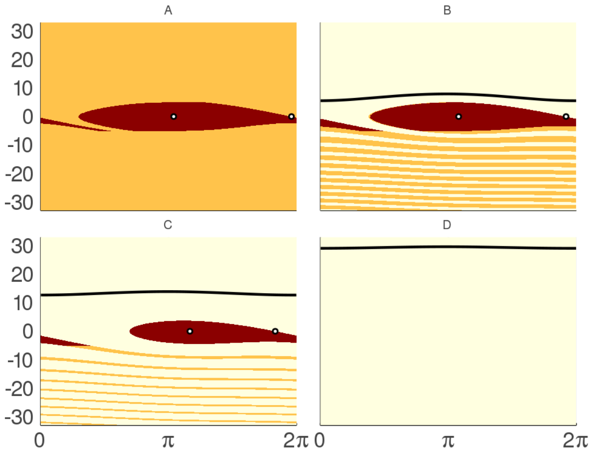

FIG. 11 Survivability region (red) of the stable fixed point of Eq. (96), with survival region given by the region between the lines $\dot{\delta} = \pm 5\,\mathrm{rad/s}$. The basin of attraction of 9 is shaded in (orange). Parameters are $\frac{2H}{\omega_R} = 1$, $D = 0.3$, $K = 8$ and A) $P = 1$, B) $P = 2$, C) $P = 4$, D) $P = 9$. The white dots are the stable and unstable fixed points. The black line gives the limit cycle.

We now analyze how the stability of the swing equation (96) is affected if the mechanical input power of a machine fluctuates in time as

$$P_{\mathrm{mech}}(t) = \bar{P} + \xi(t). \quad (106)$$

Notably, this problem can be solved almost fully analytically in the case of white noise $\xi(t)$ using Kramers' escape rate theory (Risken, 1996). Using the analogy to a particle moving in a tilted washboard potential (98), the main question is: Can the particle overcome the potential barrier and thus escapes the vicinity of the stable fixed point as illustrated in Fig. 12 (a,b)? What is the probability for such a desynchronization event?

Kramers' theory gives the average time $\bar{\tau}$ until a particle escapes (van Kampen, 2007; Schäfer *et al.*, 2017)

$$\bar{\tau} = \frac{2\pi\varrho}{\sqrt{\mathcal{V}''_{\mathrm{eff}}(\delta_{\min})\,|\mathcal{V}''_{\mathrm{eff}}(\delta_{\max})|}}\exp\left(\frac{2\eta\,\Delta\mathcal{V}_{\mathrm{eff}}}{\sigma^2}\right), \quad (107)$$

where σ^2 is the variance of the Gaussian white noise, $\eta = D$ the effective friction and $2\varrho = \eta + \sqrt{\eta^2 + (8H/\omega_R)|\mathcal{V}''_{\mathrm{eff}}(\delta_{\max})|}$ for intermediate damping. The quantities $\mathcal{V}''(\delta_{\min,\max})$ are the second derivatives of the potential evaluated at the local minimum and maximum $\delta_{\min,\max}$, respectively, and

$$\Delta\mathcal{V}_{\mathrm{eff}} = \mathcal{V}_{\mathrm{eff}}(\delta_{\max}) - \mathcal{V}_{\mathrm{eff}}(\delta_{\min}) \quad (108)$$

is the potential barrier that the particle has to overcome. Numerical simulations show an excellent agreement with this prediction as shown in Fig. 12(c).

Kramers' formula (107) reveals how the system parameters affect the stability. The main factors are noise

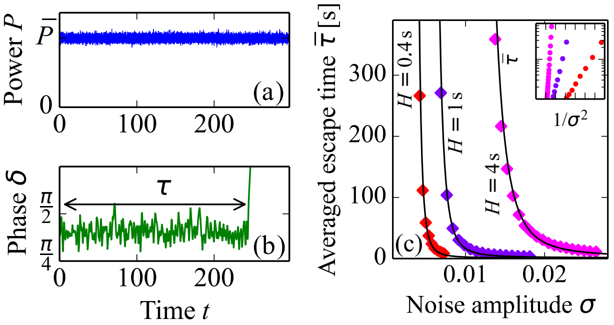

FIG. 12 Desynchronization of the swing equation due to a fluctuating power input. (a,b) When the input power P_{mech} fluctuates, the generator can lose synchrony to the grid after an escape time τ. (c) Kramer's escape rate theory predicts the escape process for Gaussian white noise. The theoretical prediction, (107) (black lines) well predicts the mean escape times $\bar{\tau}$ obtained from direct numerical simulations averaged over 2000 sample processes (symbols). Results are shown for an extremely loaded connection with $K = 1$ and $\bar{P} = 0.95$ and a damping coefficient of $D = 8 \times 10^{-5}\,\mathrm{s}^{-1} \times \omega_R$ (intermediate damping). Figure reproduced from (Schäfer *et al.*, 2017).

strength σ, damping parameter D and potential barrier $\Delta\mathcal{V}_{\mathrm{eff}}$, which enter Kramers' formula exponentially. In contrast, $\bar{\tau}$ depends less sensitively on the inertia H which enters only algebraically.

The barrier is determined by the effective tilting of the potential, i.e. the loading of the grid and vanishes as $\bar{P} \to P_{\mathrm{crit}}$. Fig. 12 demonstrates the escape process for an extreme load, whereas $\bar{\tau}$ is longer by orders of magnitude for realistic loading levels. However, $\bar{\tau}$ can be drastically reduced if the noise is no longer Gaussian but intermittent which is typical for wind power systems (Schmietendorf *et al.*, 2017). In larger power grids, different escape routes can exists, corresponding to different parts of the grid loosing synchrony (Schäfer *et al.*, 2017). In section VIII.D we will reconsider the stability of the swing equation under several generalizations.

VI. SYNCHRONIZATION AND STEADY STATES IN COMPLEX GRIDS

A. The need for synchrony

The stable steady operation of a power grid requires perfect phase-locking of all synchronous machines throughout the grid (Dörfler *et al.*, 2013; Motter *et al.*, 2013; Rohden *et al.*, 2012). That is, all machines in a connected network have to run at the same frequency with a well defined phase difference between them – otherwise no steady power flow is possible. From Eq. (73) we find that, if the nodes operate at their nominal voltage amplitude $E_j = 1$, the real power flow between two nodes j and k is determined by their phase difference

$$P_{i\to j} = K_{ij}(\sin(\gamma_{ij}) + \sin(\delta_i(t) - \delta_j(t) - \gamma_{ij})), \qquad (109)$$

where $Y^{\mathrm{eff}}_{ij} = K_{ij}e^{\mathrm{i}(\gamma_{ij}+\pi/2)}$ is the effective nodal admittance and the term $\sin(\gamma_{ij})$ comes from the diagonal of Y^{eff}. The same expression is used for the aggregated model introduced in section III.C.9 with $\gamma_{ij} = 0$.

Under fault conditions, a fast transient instability can occur where a group of machines accelerates relative to the others. Then the relative phases $\delta_{i,j}(t)$ between the groups are no longer locked and there is no steady power flow $P_{i\to j}$. If the fault clears, another transient may either diverge or converge. Transient instabilities on time scales of cycles typically lead to the shut down ("tripping") of both transmission lines and generators.

Furthermore, violations of perfect phase-locking are observed during 'inter-area oscillations', where electric power oscillates across the grid at low frequencies of 0.1 Hz - 10 Hz (Klein *et al.*, 1991; Rogers, 2012). Inter-area oscillations occur repeatedly after disturbances such as the loss of a generator and are typically damped out in minutes. However, oscillations may also grow in exceptional cases, eventually leading to a system split or blackout. For instance, a cascade of failures led to the tripping of several transmission lines and the loss of the stable steady state during 2006 European power outage (Union for the Coordination of Transmission of Electricity, 2007). Oscillations grew rapidly and finally the grid separated into three mutually asynchronous areas.

We are thus led to a fundamental question of power system stability: Do the equations of motion admit a stable solution where all nodes are perfectly phase-locked,

$$\delta_j(t) = \Omega t + \delta_j^\circ, \qquad \text{for } j \in \{1, \dots, \mathtt{N}\}, \qquad (110)$$

given the network topology and the power injections? Synchrony is about phase dynamics, therefore it is natural to focus on the phases as dynamic variables in the following. To simplify the analysis, we will neglect voltage dynamics for the time being and assume that the phase dynamics at the nodes is well described by the swing equation (49). As discussed in the previous sections, this equation is very generic and arises similarly for single synchronous machines, grid-forming inverters with power control and aggregated dynamical models. Absorbing the various factors in front of $\ddot{\delta}_i$ and $\dot{\delta}_i$ into reduced inertia J_i and damping D_i coefficients, the central equation in question then reads

$$J_i\ddot{\delta}_i = P_i - D_i\dot{\delta}_i - \sum_j K_{ij}(\sin(\gamma_{ij}) + \sin(\delta_i - \delta_j - \gamma_{ij})). \qquad (111)$$

The general problem of synchronization and dynamical stability with voltage dynamics is more involved, and we will present a short outlook at the end of this section.

Versions of this model have also been studied in the theoretical physics literature under the name second order Kuramoto model, cf. (Rodrigues *et al.*, 2016, Chapter 7). However, it should be noted that different aspects of synchronization have traditionally attracted more attention in theoretical physics. Starting from the seminal work of Kuramoto (Kuramoto, 1975) many researchers have investigated the transition from incoherence to partial synchronization, where some nodes lock their frequencies. This is clearly not sufficient for power systems. Furthermore, many essential results on partial synchronization have been obtained in a large-N mean-field limit. A generalized large-N limit for complex networks and the problem of full synchronization has been treated only recently in (Kuehn and Throm, 2019).

B. Linear Stability of the phase dynamics

We begin by assuming that a solution to the static equations is given. Then, we study whether its phase dynamics is stable to small perturbations. Consider a small perturbation around the synchronous fixed point, $\delta_i(t) = \Omega t + \delta_i^\circ + \alpha_i(t)$. To linear order perturbations evolve according to

$$J_i \ddot{\alpha}_i = -D_i \dot{\alpha}_i - \sum_{j=1}^{\mathtt{N}} \Lambda_{ij} \alpha_j \tag{112}$$

with the matrix $\Lambda \in \mathbb{R}^{\mathtt{N}\times\mathtt{N}}$ defined as

$$\Lambda_{ij} = \begin{cases} -K_{ij}\cos(\delta_i^\circ - \delta_j^\circ - \gamma_{ij}) & \text{if } i \neq j \\ \sum_{n\neq i} K_{in}\cos(\delta_i^\circ - \delta_n^\circ - \gamma_{ij}) & \text{if } i = j. \end{cases} \tag{113}$$

The fixed point is linearly stable if all perturbations $\boldsymbol{\alpha}$ are damped. We note that power grid synchrony is not affected if all angles δ_i are shifted by a constant. Thus, this mode is excluded from the stability analysis. One can show that stability is primarily determined by Λ: The synchronous state is linearly stable if all eigenvalues of Λ are positive, except for the one corresponding to a global shift of all phases. This criterion becomes especially simple if line losses can be neglected. Then $\gamma_{ij} = 0$ and Λ is a weighted, symmetric Laplacian matrix, cf. section II. Stability is guaranteed as long as the 'weights' $K_{ij}\cos(\delta_i^\circ - \delta_j^\circ)$ are positive for all links (i,j), i.e. if no line is overloaded,

$$|\delta_i^\circ - \delta_j^\circ| < \pi/2. \tag{114}$$

This criterion is sufficient, but generally not necessary. It can be viewed as a generalization of the stability criterion for a single generator discussed in section V.C.1.

The situation becomes more involved when line losses can not be neglected. The condition $|\delta_i^\circ - \delta_j^\circ - \gamma_{ij}| < \pi/2$ is then not sufficient and more subtle necessary conditions were derived (Skar, 1980). Further effective criteria for the definiteness of signed Laplacians were given in (Chen *et al.*, 2016; Song *et al.*, 2015). Lyapunov exponents and vectors for this system have been studied in (Bosetti and Khan, 2017). It should be noted that phase differences in transmission grids are typically much smaller. Other factors limit power transmission, at least for short transmission lines (cf. Fig. 7).

Stability can be lost if a parameter of the network is varied, e.g. if power injections and grid loads increase or transmission lines fail (Coletta and Jacquod, 2019). Eventually, the second Laplacian eigenvalue tends to zero and the fixed point is lost in an inverse saddle-node bifurcation on a circle (Manik *et al.*, 2014). Notably, bifurcation sets and linear stability properties become much more intriguing if voltage dynamics is included (Ma *et al.*, 2016; Schmietendorf *et al.*, 2014; Sharafutdinov *et al.*, 2018), or in inverter based grids (Schiffer *et al.*, 2014). An overview of different aspects of dynamical stability is provided in (Gajduk *et al.*, 2014a).

C. Existence, multiplicity and properties of synchronous states

We now turn back to the question whether a stable synchronous state exists for a given power grid. We first review some important properties of synchronous states and then review a theoretical approach to systematically compute and classify all such states.

1. Properties of synchronous states

The proper operation of a power grid requires perfect phase locking according to Eq. (110). Substituting into the equations of motions (111) yields the fundamental condition for the phases and active power flows in the synchronous state of a power grid,

$$0 = P_i - D_i\Omega - \sum_j K_{ij}(\sin(\gamma_{ij}) + \sin(\delta_i^\circ - \delta_j^\circ - \gamma_{ij})). \tag{115}$$

We note that the flows are asymmetric for $\gamma \neq 0$ due to Ohmic losses. In fact, one can express the losses at a transmission line (i,j) as

$$P_{ij}^{\text{loss}} = P_{i\to j} + P_{j\to i} = 2K_{ij}\sin(\gamma_{ij})\big[1 - \cos(\delta_i^\circ - \delta_j^\circ)\big].$$

Losses vanish when $\gamma_{ij} = 0$ and when there is no power flowing on the line, i.e. when $\delta_i^\circ = \delta_j^\circ$.

Synchrony does not necessarily imply that the grid operates exactly that the reference frequency of 60/60 Hz. In fact, we can determine the equilibrium frequency directly from Eq. (115). Summing over all nodes $i \in \{1,\ldots,\mathtt{N}\}$ and solving for Ω yields

$$\Omega = \frac{\sum_i P_i - \sum_{i<j} P_{ij}^{\text{loss}}}{\sum_i D_i}. \tag{116}$$

We recall that the effective parameters D_i include both damping and the action of primary load-frequency control, such that the current result is equivalent to Eq. (89).

The deviation from the reference frequency Ω is given by the ratio of the power imbalance, including losses and the cumulative primary control strength. We will come back to the analysis of the bulk frequency in section VIII.A.

2. Phase cohesiveness and necessary conditions

We are particularly interested in synchronous states where angle differences are small, cf. the discussion in section V.A. Small angle differences are also essential for many analytic results on the stability of the swing equation, cf. for example the linear stability condition (114). To state this aspect more precisely we define the *cohesiveness*: A state is called phase cohesive if all phases δ_i° lie in an arc of length $\zeta \in [0, \pi/2)$ denoted as $\mathfrak{A}(\zeta)$.

The definition can be applied to derive necessary conditions for synchronization. For the sake of simplicity, assume that the power in the grid is balanced and that we have no losses $\sum_i P_i = 0$, $\gamma_{ij} = 0$. Hence, we have $\Omega = 0$ in Eq. (110) and the condition for phase locking in the second-order power grid model (111) reads

$$P_i = \sum_{n=1}^{\mathtt{N}} K_{in} \sin(\delta_i^\circ - \delta_n^\circ). \tag{117}$$

For a phase cohesive sync state, the magnitude of the sum can be bounded from above by $\sin(\zeta) \sum_n K_{in}$ such that Eq. (117) can be satisfied only if for all $i \in \{1, \ldots, \mathtt{N}\}$

$$|P_i| \leq \sin(\zeta) \sum_{n=1}^{\mathtt{N}} K_{in} \tag{118}$$

Furthermore we can consider any two nodes i, j of the grid and evaluate the difference of the conditions (117). Again we can bound the sums on the right-hand side which yields the condition for all $i, j \in \{1, \ldots, \mathtt{N}\}$

$$|P_i - P_j| \leq \sin(\zeta) \sum_{n=1}^{\mathtt{N}} K_{in} + K_{jn}. \tag{119}$$

The two conditions are necessary for a cohesive sync state to exist, but they are not sufficient by all means. Nevertheless, they reveal two important facts: (i) Synchronization requires a sufficient connectivity of the grid, while a strong divergence of the P_i impedes synchronization (ii) If the phase divergence ζ shall be reduced, we have to increase the coupling or decrease the divergence of the P_i. Further generalizations and refinements are discussed in (Ainsworth and Grijalva, 2013; Chopra and Spong, 2009; Dörfler *et al.*, 2013).

3. Existence of solutions and multistability

We now turn to the question whether solutions to the power flow equations exist. Notably, power grids can admit multiple stable and unstable states of operation, even when power injections are fixed. Sudden changes of the power injections or the grid topology can trigger transitions between theses states with drastic consequences for grid operation and stability. Circulating power flows can emerge, which are generally undesired as they increase line loads and Ohmic losses. A classic example of such circulating power flows is the Lake Erie loop in North America (Coletta *et al.*, 2016; Jafarpour *et al.*, 2019). If the system finds itself in a situation in which no stable synchronous state exists, system collapse is an inevitable consequence. We begin with the simplest case of a power grid without Ohmic losses such that the fixed points are determined by Eq. (117). The central question is now: When does this equation have multiple solutions that correspond to a dynamically stable power flow and why?

We start with an elementary example: a simple ring network where $P_i = 0$ for all nodes $i \in \{1, \ldots, \mathtt{N}\}$ and homogeneous line parameters K (Schröder *et al.*, 2017). One can easily verify that the fixed points of this network are given by $\delta_i^* = 2\pi i m/\mathtt{N}$ with a parameter $m \in \{-\mathtt{N}/2, -\mathtt{N}/2+1, \ldots, +\mathtt{N}/2\}$. Fixed points with $m \in (-\mathtt{N}/4, +\mathtt{N}/4)$ satisfy (114) and are guaranteed to be dynamically stable, all other fixed points are potentially unstable. This simple example already suggests the fundamental features of multiplicity of sync states. Power flow solutions in lossless grids can differ in *cycle flows*. In fact, each fixed point corresponds to a flow $f = K \sin(2\pi m/\mathtt{N})$ around the cycle. The number of stable fixed points increases with the size of the loop, being limited to one if $\mathtt{N} \leq 4$.

Using these insights, we introduce a general method to construct all (stable) fixed points of a generic lossless power grid, following (Manik *et al.*, 2017b). The main idea is to shift the focus from nodes to the edges and cycles of the network. Hence, we define a vector of flows on the network's edges

$$\boldsymbol{F} = B_d \sin(E^\top \boldsymbol{\delta}) \in \mathbb{R}^{\mathtt{L}}, \tag{120}$$

where E denotes the node-edge incidence matrix (4) and the sine function is taken element-wise. The steady state conditions (117) then become

$$\boldsymbol{P} = E\boldsymbol{F}\,. \tag{121}$$

Fixed points are now obtained via a step-wise procedure: We first construct all solutions of Eq. (121) and then reject those which are incompatible with Eq. (120).

The first step is based on the following observation: The kernel of the incidence matrix E corresponds exactly to *cycle flows* in the network. Hence, the general solution of Eq. (121) can be written as

$$\boldsymbol{F} = \boldsymbol{F}^{(s)} + C\boldsymbol{f}, \tag{122}$$

where $\boldsymbol{F}^{(s)} \in \mathbb{R}^{\mathtt{L}}$ is a specific solution, $\boldsymbol{f} \in \mathbb{R}^{\mathtt{L}-\mathtt{N}+1}$ gives the strength of the cycle flows, and the matrix C is the

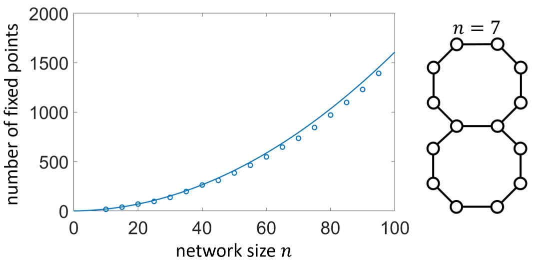

FIG. 13 Multiplicity of sync states: Scaling of the number stable fixed points in a grid with two cycles. The grid consists of two rings with $(n-1)$ nodes sharing one edge, such that $\mathtt{N} = 2n$. Edge weights are assumed to be homogeneous and loads vanish, $P_i = 0$. The analytic scaling result $0.1576(n^2 + 2n)$ (solid line) well matches the numerically exact results (circles). Figure adapted from (Manik *et al.*, 2017b).

cycle-edge incidence matrix (5). For each flow vector $\boldsymbol{F}$, we can construct the associated nodal phases as follows. Start at the slack node s and set $\delta_s^\circ = 0$. Then proceed to a neighbouring node j. Assuming that the connecting edge $e \hat{=} (j, s)$ is oriented from node s to node j, the phase value reads $\delta_j^\circ = \delta_s^\circ + \Delta_e$, where the phase difference Δ_e is reconstructed from the flow F_e by inverting Eq. (120), which yields two possible solutions

$$\begin{aligned} \Delta_e^+ &= \arcsin(F_e/K_e) \quad \text{or} \\ \Delta_e^- &= \pi - \arcsin(F_e/K_e). \end{aligned} \tag{123}$$

We must choose one of the solutions and we keep track of this choice by decomposing the edge set as $\mathtt{E} = \mathtt{E}_+ \cup \mathtt{E}_-$ where $\mathtt{E}_\pm = \{e \in \mathtt{E} \mid \Delta_e = \Delta_e^\pm\}$ Not all solutions obtained this way are physically correct. We can get the physically correct ones by making sure that the sum of the phase differences around any fundamental cycle yields zero or an integer multiple of 2π, which is expressed via the winding number condition,

$$\varpi_c = \frac{1}{2\pi} \sum_{e=1}^{\mathtt{L}} C_{e,c} \Delta_e^\pm \in \mathbb{Z} \tag{124}$$

Fixed points with $\mathtt{E}_- = \emptyset$ satisfy (114) and are always stable, while states with $\mathtt{E}_- \neq \emptyset$ are typically unstable (Delabays *et al.*, 2017; Manik *et al.*, 2017b, 2014).

The cycle flow approach yields numerous analytical insights into the occurrence of multiplicity of sync states:

- No multiplicity in trees: In a lossless tree network, either there is no fixed point or there are $2^{\mathtt{N}-1}$ fixed points of which one is stable and $2^{\mathtt{N}-1}$ are unstable (Manik *et al.*, 2017b).

- Similarly, multiplicity is ruled out in very dense networks as the fundamental cycles are too small (Taylor, 2012). Hence all fixed points except one include edges with $|\delta_i^\circ - \delta_j^\circ| > \pi/2$.

- In a simple ring network, one can derive explicit upper and lower bounds for the number of fixed points. Generally, the number of fixed point increase with the size of the ring and decreases with the loading of the grid (Delabays *et al.*, 2016; Manik *et al.*, 2017b; Ochab and Gora, 2010).

- In plane networks, one can show that the winding vector is unique. That is, two fixed points cannot have the same winding vector and the same decomposition $\mathtt{E} = \mathtt{E}_+ \cup \mathtt{E}_-$. This can be used to derive upper bounds for the number of (stable) fixed points (Delabays *et al.*, 2017; Manik *et al.*, 2017b).

- One can derive estimates for the number of stable fixed points using scaling relations (Manik *et al.*, 2017b), an example being shown in Fig. 13. Further numerical results for large sparse networks are discussed in (Mehta *et al.*, 2015; Xi *et al.*, 2017).

The previous approach can be generalized to include Ohmic losses (Balestra *et al.*, 2019). Again one first focuses on the lines and considers the flows F_{ij} and the losses $L_{ij} = g_{jk}\left[1 - \cos(\delta_i^\circ - \delta_j^\circ)\right]$ as basic variables. The power balance equation is linear in these variables and one can construct the general solution of this set of equations. Among this huge set of solutions candidates the correct solutions are found by imposing the winding number conditions (124) and the additional constraint

$$\left(\frac{F_{ij}}{b_{ij}}\right)^2 + \left(\frac{L_{ij}}{g_{ij}} - 1\right)^2 = 1 \quad \text{for all edges } (i,j), \tag{125}$$

which follows from $\sin^2 + \cos^2 = 1$. One then finds that Ohmic losses can have two conflicting effects on the existence and number of stable steady states: On the one hand, high losses must be compensated by higher power flows, which may decrease their number. On the other hand, Ohmic losses can stabilize certain solution branches and thus foster multistability.

D. Nonlinear stability and explicit synchronization criteria

The existence of a phase-locked state is a prerequisite for the stable operation of a power grid. But even in elementary networks phase-locked states and limit cycles can coexist, see Fig. 9, and it depends on the initial conditions whether phases lock or not. In the following, we review explicit criteria for synchronization based on the dynamics (111) and discuss the main factors determining a network's synchronization capability. A comprehensive overview is provided in the excellent review article (Dörfler and Bullo, 2014).

1. Sufficient criteria for dense networks

We first present a sufficient condition for dense networks, which arise naturally in power system models after Kron reduction (cf. Sec. III.C.6). We are mainly interested second-order power grid model dynamics (111), but it is simpler to start with the overdamped limit,

$$D_i\dot{\delta}_i = P_i + \sum_j K_{ij}(\sin(\gamma_{ij}) - \sin(\delta_i - \delta_j - \gamma_{ij})). \quad (126)$$

Dörfler and Bullo have proven that this system achieves phase cohesiveness and frequency synchronization if the coupling is strong compared to the differences in natural frequencies $\omega_i^{\mathrm{nat}} = P_i + \sum_j K_{ij}\sin(\gamma_{ij})$ (Dörfler and Bullo, 2012). They quantify these two opposing forces in terms of the parameters

$$\Gamma_{\min} := \mathtt{N}\min_{i\neq j}\left(\frac{K_{ij}}{D_i}\cos(\gamma_{ij})\right), \quad (127)$$

$$\Gamma_{\mathrm{critical}} := \frac{1}{\cos(\gamma_{\max})}\left(\max_{i\neq j}\left|\frac{\omega_i^{nat}}{D_i} - \frac{\omega_j^{nat}}{D_j}\right| + 2\max_i\sum_{j=1}^{\mathtt{N}}\frac{K_{ij}}{D_i}\sin(\gamma_{ij})\right). \quad (128)$$

Furthermore, they define $\zeta_{\min} \in [0, \pi/2 - \gamma_{\max})$ and $\zeta_{\max} \in (\pi/2, \pi]$ as the solutions of the equation $\sin(\zeta_{\min}) = \sin(\zeta_{\max}) = \cos(\gamma_{\max})\Gamma_{\mathrm{critical}}/\Gamma_{\min}$ whenever this solution exists.

Then they derive the following theorem: If $\Gamma_{\min} > \Gamma_{\mathrm{critical}}$ and the angles are initially not too different (all $\delta_i(0)$ are in the arc $\mathfrak{A}(\zeta_{\max})$), then the network will achieve exponential frequency synchronization, i.e. all frequencies $\dot{\delta}_i$ converge exponentially fast to a common frequency Ω. The phases remain cohesive and all $\delta_i(t)$ reach the arc $\bar{\mathfrak{A}}(\zeta_{\min})$.

Dörfler and Bullo further generalize this result to the second-order power system model (111) if the damping is high enough. More precisely, if the ratio $\epsilon = J_{\max}/D_{\min}$ is lower than a critical value ϵ^*, the solution of the second-order model is well approximated by the solution of the first-order Kuramoto model up to an error of order ϵ. They further argue that for actual power systems ϵ is of the order of 0.1 if one takes into account the control system in the effective damping constant D_i.

Let us sketch the main idea of the proof of these theorems. For each point in time t we identify the nodes m and n with the largest and smallest angles. That is, all angles $\delta_i(t)$ are in the arc $[\delta_n(t), \delta_m(t)]$ and

$$\mathfrak{V}(t) = \delta_m(t) - \delta_n(t) \quad (129)$$

denotes the length of the arc. One can then compute the derivative $d\mathfrak{V}/dt$ explicitly and finds that this expression is strictly non-positive if

$$\Gamma_{\min}\sin(\zeta) \geq \cos(\gamma_{\max})\Gamma_{\max}. \quad (130)$$

If this condition is satisfied, the arc $\mathfrak{A}(\zeta)$ cannot grow and the angles remain cohesive. Frequency synchronization is shown in a second step by differentiating Eq. (126) with respect to time,

$$\begin{aligned}\frac{d}{dt}\dot{\delta}_i &= -\sum_{j=1}^{\mathtt{N}}\frac{K_{ij}}{D_i}\cos(\delta_i - \delta_j - \gamma_{ij})(\dot{\delta}_i - \dot{\delta}_j)\\ &= -\sum_{j=1}^{\mathtt{N}}\tilde{\Lambda}_{ij}(t)\delta_j. \end{aligned} \quad (131)$$

Under the condition of phase cohesiveness, the matrix $\tilde{\Lambda}(t)$ is a time-varying directed Laplacian. Hence, Eq. (131) describes a *contraction* and all frequencies $\dot{\delta}_n$ must converge exponentially to a common value Ω. Finally, the generalization to the second-order power system model is analyzed within singular perturbation theory.

2. Sufficient criteria for sparse networks

The sufficient criterion presented above holds for all networks, but is of little use if the topology is sparse since we then have $\Gamma_{\min} = 0$. A different approach is needed in this case. One family of sufficient criteria for the existence of a phase locked state uses a method introduced by Jadbabaie et al (Jadbabaie *et al.*, 2004). The steady state condition (117) is reformulated in a vectorial form

$$\boldsymbol{P} = \tilde{\Lambda}(\boldsymbol{\delta})\boldsymbol{\delta}, \quad (132)$$

where $\tilde{\Lambda}(\boldsymbol{\delta})$ is a state-dependent Laplacian with edge weights $w_{ij} = K_{ij}\sin(\delta_i - \delta_j)/(\delta_i - \delta_j)$. One can then apply fixed point theorems to derive conditions which guarantee that Eq. (132) has a solution. For instance, one can formulate a condition in terms of the algebraic connectivity of the network (cf. section II), which yields a sufficient condition for the existence of a synchronized state (Dörfler and Bullo, 2012)

$$\lambda_2(\Lambda) > \left(\sum_{(i,j)\in\mathtt{E}}|P_i - P_j|^2\right)^{1/2}, \quad (133)$$

where $\lambda_2(\Lambda)$ is the algebraic connectivity of the ordinary weighted graph Laplacian. We note that one has to be careful about the domain when applying fixed points theorems. In particular, the sufficient conditions do *not* guarantee uniqueness of a solution, as discussed in (Manik *et al.*, 2017b).

Another approach uses cycle flow arguments as introduced in section III.A.6. Denoting the sine of the phase difference along the line ℓ as ψ_ℓ we have the general relation (36). It has been shown that the cycle flow contribution $\boldsymbol{f}$ is actually negligible in most cases such such that

$\boldsymbol{\psi} \approx E^\top \Lambda^* \boldsymbol{P}$ (Dörfler *et al.*, 2013). Hence a synchronous state with a phase cohesiveness ζ exists if

$$\sin(\zeta) \geq \|\boldsymbol{\psi}\|_\infty \approx \|E^\top \Lambda^* \boldsymbol{P}\|_\infty . \tag{134}$$

This equation provides a rigorous sufficient condition for many elementary networks and an excellent approximate condition for actual power grid topologies (Dörfler *et al.*, 2013). Recently, generalized types of Lyapunov function were derived for lossless power grids (111), allowing to derive sufficient conditions for global stability of synchronous states (Schiffer *et al.*, 2018, 2019).

E. Probabilistic analysis of nonlinear stability

The synchronous state of a power grid can be globally stable in favorable cases, but typically several different asymptotic attractors exist. This includes for example limit cycles as shown in Fig. 9 for a single generator. In this section we explore the nonlinear stability of different attractors of the swing equation using probabilistic methods introduced in Sec. V.C.3. We note that the swing equation is a simplified model of power system dynamics in the vicinity of the synchronized state. Hence, non-synchronous attractors of this model do not faithfully describe asymptotic states of real systems. Nevertheless, they show when system properties that are accurately captured by the swing equation, inertia and primary control action, are insufficient to stabilize the system.

1. Limit cycles and other attractors

A large variety of only partially understood attractors exist in power system models. Limit cycles similar to the ones discussed for a single machine in Sec. V.C.2) are among the most common non-synchronous attractors. These states can be understand as arising from a partial decoupling limit. Consider a network consisting of two disconnected parts $\mathtt{V}_l$ and $\mathtt{V}_r$. Both parts can synchronize independently at respective frequencies Ω_l and Ω_r according to (116).

If the two parts are weakly coupled, the equations of motion include terms proportional to $\sin((\Omega_l - \Omega_r)t)$, which average out in time. The limit cycle with separate frequencies Ω_l and Ω_l persists, but the coupling causes perturbations leading to oscillations around the mean frequencies (Gelbrecht *et al.*, 2020). When the coupling increases, the basin size of these attractors (the variance of the frequency time series) may even increase until the attractors eventually becomes unstable. Figure 14 illustrates the nonlinear stability of such states in a network with two populations of oscillators with power injections $P_i = \pm 1$, effective damping $D_i = 0.1$ and homogeneous line parameters K. For weak coupling the oscillators always rotate freely at $\dot{\delta} = P_i/D_i$. When the coupling increases, a large variety of attractors come into being, most of them with negligible basin size (referred to as outliers). Two partially synchronous states of the type discussed above occur more often. The basin size first increases with K, but then the fully synchronized state becomes dominant. Its basin size increases rapidly for $K \geq 4$, reaching unity for $K \gtrsim 8$.

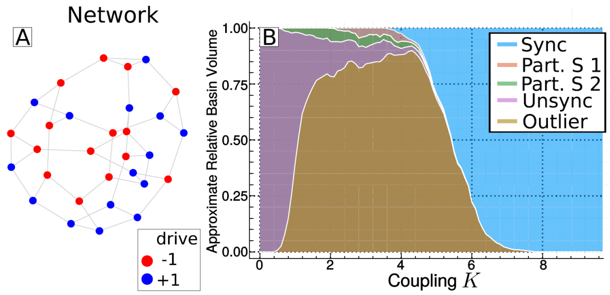

FIG. 14 Nonlinear stability of different attractors in a small ample network. (A) Structure of the network with two classes of nodes with injections $P_i = \pm 1$. (B) The basin bifurcation diagram for the system with the synchronized, partially synchronized and synchronized regimes.

The occurrence of similar states was already studied from the point of view of hysteresis in (Olmi *et al.*, 2014). However, not all asymptotic states with appreciable basin have this form. Olmi (2015) found that complex chimeras are possible, and Nitzbon *et al.* (2017) saw that perturbations at some types of nodes lead to limit cycles with a frequency not given by (116). The impact of noise, inertia and network topology on different limit cycles and the hysteresis behavior was studied in (Tumash *et al.*, 2018).

2. The impact of network structure

We now turn back to the synchronized state and investigate its nonlinear stability with respect to localized perturbations in terms of the single-node basin stability. In particular, the set of initial state $\mathcal{A}$ is chosen such that all nodes except one are at the fixed point values initially. This measure is of high practical relevance, as actual failures or disturbances are typically limited to a single machine or a small subnetwork. Further, it reveals the vulnerable nodes in a grid. A numerical analysis for sparse networks (Menck *et al.*, 2014) showed that the local network features have a substantial impact on the single node basin stability. In particular, dead ends tend to cause exceptionally poor single node basin stability. Nodes at which the dead end is connected to the rest of the grid must be viewed as the most vulnerable spots with respect to dynamical perturbations.

The more detailed study of Schultz *et al.* (2014a), based on a more realistic network ensemble introduced in (Schultz *et al.*, 2014b) identified detours as stabilizing features and showed that there is a statistically robust re-

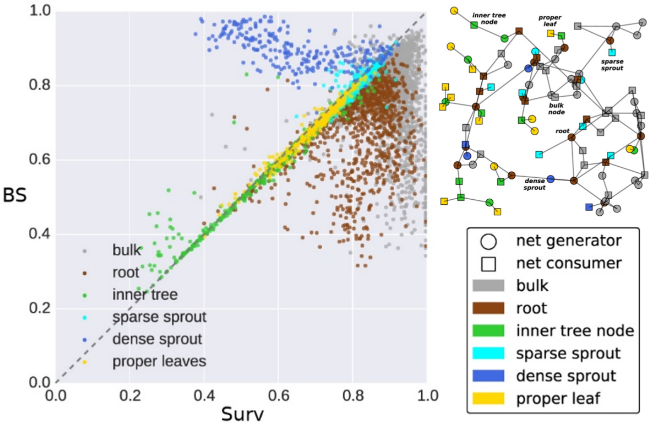

FIG. 15 Topological properties determine the single node basin stability and survivability. Left: Survivability (Surv) and Basin Stability (BS) for nodes in a synthetic power grid network ensemble, showing pronounced differences in the behaviors of various node types. Right: Node classification according to Nitzbon *et al.* (2017). Edges that are not in any cycles are trees. The nodes in trees are distinguished into roots (part of a cycle and a tree), sprouts (degree 1 nodes next to a root), leaf (degree 1 nodes not next to roots) and inner tree nodes. Sprouts are further distinguished according to their neighbour degree into dense ($k_{av} > 5$) and sparse ($k_{av} \leq 5$). Figures adapted from (Nitzbon *et al.*, 2017).

lationship between network features and node robustness. Kim *et al.* (2015) showed that the community structure of the system determines which nodes reach a high single node basin stability first, when increasing the coupling strength. In (Kim *et al.*, 2016) a systematic exploration of the impact of network motifs on single node basin stability finds that betweenness and degree matter specifically. Kim *et al.* (2018) and (Kim *et al.*, 2016) show that there exists strong non-monotonic behavior of basin stability with increasing coupling strength. Finally, Kim *et al.* (2019) introduced Integrated Basin Stability as a way to understand the transition to global synchrony as a function of increasing coupling strength.

A more detailed picture emerges if we add survivability, the probability that a perturbation does not lead to a violation of transient operational bounds. Hellmann *et al.* (2016) showed a strong direct dependence of single node survivability on the node degree, with high degree nodes being particularly unstable. Combining survivability and basin stability. Nitzbon *et al.* (2017) showed a detailed picture of various single node stabilities as a function of topology. Key for this is a node classification into those in a loop and those on a tree. Further subdividing the tree nodes into leaves, inner tree nodes, and sprouts of high and low neighbor degree identified classes of nodes that show qualitatively different stability behavior, see Fig. 15. Perturbations at some of these nodes were shown to result in novel asymptotic states already, mentioned in the previous section, that can not be explained through a decoupling limit.

3. The necessity of realistic models

When identifying the imprint of network structure on the stability properties of individual nodes one usually proceeds by simplifying the system. In order to isolate the impact of topology, other factors are taken out. For example, most above studies assume homogeneous node parameters and neglect voltage dynamics and losses. We can use probabilistic methods to understand how much these assumptions actually alter the picture.

Wolff *et al.* (2018) show that both inhomogeneity of the nodes, and the details of the coupling of generators into the grid actually have a profound impact on the single node stability. They evaluate the basin stability and the return times to the sync state for power grids with a fixed topology, but using a variety of models including the heterogeneity in the node and line parameters and the more detailed coupling of generators, where the generator is located at an internal node, coupled by a line to the system bus. The grid is completely stable for homogeneous parameters, but exhibited instability when introducing heterogeneity. The coupling of generators at internal nodes was found to stabilize the system overall, however the location of unstable nodes also changed.

Taking higher order internal dynamics of the generators into account for single node stability analysis was considered by Auer *et al.* (2016). It was found that while single node survivability is well captured by the swing equation (111), voltage dynamics and internal nodes can lead to additional asymptotic instabilities once outside the survivability region. First results on basin stability of higher order generator models were obtained by Liu *et al.* (2018).

Finally, most of the works discussed above and much of the theoretical literature focus on lossless grids. Real transmission lines have a small but non-zero resistance (cf. Table I), and typical values of the parameter γ in Eq. (109) are around 0.24. While neglecting Ohmic losses is often justified for the power flow in the synchronized state, limit cycles and global stability properties are strongly affected (Hellmann *et al.*, 2020). Figure 16a-d shows the basin of attraction of the synchronous state (peach) in the slice of phase space belonging to a single node, centered on the sync state. As γ is increased from zero to realistic values, the basin first expands and then switches to the other half plane.

A key role in this change is played by 1-solitary states, in which the entire network stays close to synchrony except for one desychronized node. If the desynchronized node is rotating with the driving force $\langle \dot{\delta}_i \rangle / P_i > 0$ we speak of a normal solitary, if it is rotating against the local driving force, we denote this as an exotic solitary state. Figure 16e shows the average asymptotic single

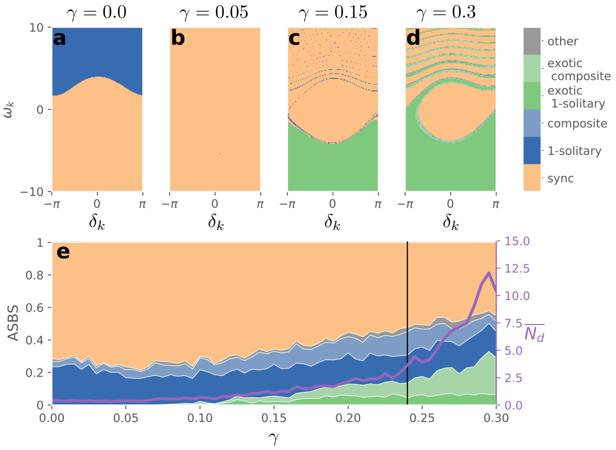

FIG. 16 The main results of (Hellmann *et al.*, 2020). Figure **a-d** show the slice of the phase space in the dimensions belonging to a node k. The different colours show different asymptotic states. Peach is the sync state, blue a solitary state, and green a solitary rotating against its power infeed. Figure **e** shows the average single node basin stability for the entire ensemble of networks, for the different types of asymptotic states, as well as the number of desynchronized oscillators following a perturbation (solid purple line). Figure adapted from (Hellmann *et al.*, 2020) CC-BY-3.0.

node basin stability for different types of asymptotic states: (i) peach for the sync state; (ii) dark blue for ordinary 1-solitary, (iii) dark green for exotic 1-solitary states, (iv) light green and blue for more complex asymptotic states that also contain individual desynchronized nodes, and (v) grey for other asymptotic states.

The presence of exotic solitary states can be understood by considering the decoupling limit for an individual oscillator from the rest of the grid. When completely decoupled it will rotate with a frequency $\Omega_{\text{sol}} = P_{\text{sol}}/D_{\text{sol}}$. If we now increase the coupling that state persists, but taking losses into account the power flow no longer averages to 0 but to $P_e = K_e \sin(\gamma_e)$ according to Eq. (109). Hence, in contrast to the lossless case, the coupling to the network will not just perturb the limit cycle but also shift its location to $\Omega_{\text{sol}} = (P_{\text{sol}} - K_e \sin(\gamma))/D_{\text{sol}}$. This picture is confirmed in detailed numerical experiments in (Hellmann *et al.*, 2020). Methods to restore synchronization from solitary states have been discussed in (Taher *et al.*, 2019).

We stress that the above results have been obtained for a particular power system model, and all models face certain limitations. For instance, the 1-solitary states are related to "pole slipping" transients in practice. They correspond to true limit cycles in the restricted model, but the dynamics is changed by the generator's protection systems, which are not included in the model. We conclude that care should be taken when interpreting models simulation results for real world situations. Models are useful in engineering power system stability. By construction, such models idealize certain real-world aspects and thus do not capture all details of real power system dynamics. In particular, many dynamical models do not account for the protection systems of changes in external conditions or control system. One advantage of probabilistic methods for stability assessment is that they can be straightforwardly adapted to models of different complexity and scope.

VII. STRUCTURAL STABILITY OF POWER GRIDS

Structural damages are the ultimate threat for power grid stability: "Typically, the blackout can be traced back to the outage of a single transmission (or generation) element" (Pourbeik *et al.*, 2006). Such an initial outage can trigger secondary outages and eventually a cascade of failures bringing down a power grid entirely. One of the most important security regulations is the $(N-1)$-rule, stating that "no single outage will result in other components experiencing flow or voltage limit violations" (Wood *et al.*, 2014). But obviously, this rule is violated occasionally, making a grid vulnerable and large scale blackouts possible.

In this section we will analyze the impact of structural damages focusing on outages of transmission elements. We mostly employ a quasi static picture, assuming that, after an outage, the grid rapidly relaxes to a new steady state (if it exists). But in this new state other transmission elements may be overloaded, leading to emergency shutdowns or short-circuit failures, and so on.

The key questions we address in the following are: (1) How do failures spread in the network? Given an transmission line failure, how and where are flows rerouted? (2) How does the entire network react to structural damages or other perturbations? Is there enough redundancy to cope with damages or do secondary failures take place? (3) Finally, how do large scale blackouts emerge? How do cascades propagate through the grid?

A. Quasi-static analysis of line outages

1. The line outage distribution factors

We first analyze the outage of a single line within the linearized load flow approximation, or DC approximation, introduced in section III.A.4. So assume that a line $\ell \hat{=} (r,s)$, that initially carries the flow $F_\ell^{(0)}$, fails. If the grid remains connected, the flow change at another transmission line $e \hat{=} (m,n)$ is linear in $F_\ell^{(0)}$,

$$\Delta F_e = \text{LODF}_{e,\ell}\, F_\ell^{(0)},$$

where the factor of proportionality is referred to as a line outage distribution factor (LODF) (Grainger and Stevenson Jr., 1994; Wood *et al.*, 2014).

We summarize the derivation of the LODFs following (Guo *et al.*, 2009; Strake *et al.*, 2018). As the line $\ell = (r,s)$ fails, the nodal susceptance matrix changes as

$$B \to B + \Delta B = B + b_{rs}\boldsymbol{\nu}_{rs}\boldsymbol{\nu}_{rs}^{\top}, \tag{135}$$

where the vector $\boldsymbol{\nu}_{rs} \in \mathbb{R}^{\mathtt{N}}$ is $+1$ at position r, -1 at position s and zero otherwise. This causes a change of the nodal phase $\boldsymbol{\theta} \to \boldsymbol{\theta}' = \boldsymbol{\theta} + \boldsymbol{\alpha}$. Subtracting the linearized load flow equations (32) for the perturbed and unperturbed grid then yields

$$(B + \Delta B)\boldsymbol{\alpha} = -\Delta B\,\boldsymbol{\theta}, \tag{136}$$

which can be solved for $\boldsymbol{\alpha}$ and used to compute the change of the line flows as

$$\Delta \boldsymbol{F} = B_d E^{\top}\boldsymbol{\alpha} = -B_d E^{\top}(B+\Delta B)^{*}\Delta B\,\boldsymbol{\theta}, \tag{137}$$

with $*$ the Moore-Penrose pseudo-inverse. This expression can be greatly simplified using the Woodbury matrix identity which finally yields

$$\Delta \boldsymbol{F} = B_d E^{\top} B^{*}\boldsymbol{\nu}_{rs}(1 - b_{rs}\boldsymbol{\nu}_{rs}^{\top}B^{*}\boldsymbol{\nu}_{rs})^{-1}F_{rs}^{(0)}\,. \tag{138}$$

and thus $\mathrm{LODF}_{e,\ell} = b_{mn}\nu_{mn}^{\top}B^{*}\boldsymbol{\nu}_{rs}(1 - b_{rs}\boldsymbol{\nu}_{rs}^{\top}B^{*}\boldsymbol{\nu}_{rs})^{-1}$.

This procedure is readily generalized to multiple line outages (Güler *et al.*, 2007; Kaiser *et al.*, 2020b). Assume that the lines $\ell_1, \ell_2, \ldots, \ell_{\mathtt{M}}$ fail, but the network remains connected. We define a projection matrix from the space of all links onto the subset of failing links $\mathfrak{P} \in \mathbb{R}^{\mathtt{M}\times\mathtt{L}}$,

$$\mathfrak{P}_{me} = \begin{cases} 1 & \text{if}\, e = \ell_m \\ 0 & \text{otherwise.} \end{cases}$$

We define projections of the node-edge incidence matrix, the branch reactance matrix, and initial flow vectors as

$$\begin{aligned} \mathcal{D} &:= \mathfrak{P}E \in \mathbb{R}^{\mathtt{N}\times\mathtt{M}}, \\ B_{\mathrm{out}} &:= \mathfrak{P}B_d\mathfrak{P}^{\top} = \mathrm{diag}(b_{\ell_1}, b_{\ell_2}, \ldots, b_{\ell_{\mathtt{M}}}) \in \mathbb{R}^{\mathtt{M}\times\mathtt{M}}, \\ \boldsymbol{F}_{\mathrm{out}}^{(0)} &= \mathfrak{P}\boldsymbol{F}^{(0)} = (F_{\ell_1}^{(0)}, \ldots, F_{\ell_{\mathtt{M}}}^{(0)}) \in \mathbb{R}^{\mathtt{M}}. \end{aligned}$$

One can then proceed as for a single failing line. Using the Woodbury matrix identity one obtains

$$\Delta \boldsymbol{F} = B_d E^{\top} B^{*}\mathcal{D}\left(1 - B_{\mathrm{out}}\mathcal{D}^{\top}B^{*}\mathcal{D}\right)^{*}\boldsymbol{F}_{\mathrm{out}}^{(0)}. \tag{139}$$

In this formulation, we only have to invert an $\mathtt{M}\times\mathtt{M}$-matrix in addition to the inversion of the initial matrix B^{*}. If $\mathtt{M}$ is small, the inverse can be evaluated explicitly and we obtain a set of generalized LODFs.

We note that contingency analysis via LODFs can be improved by a modification of the linearization procedure. One starts from the non-linear expression $F_{j\to k} = b_{jk}\sin(\theta_j - \theta_k)$ for the real power flow and carries out the linearization only at a later stage (Jung and Kettemann, 2016; Manik *et al.*, 2017a). One then obtains the same results as above, but with reweighted line susceptances

$$b_{jk} \to b_{jk}\cos(\theta_j - \theta_k). \tag{140}$$

Related approaches are sometimes referred to as a 'hot start DC approximation'.

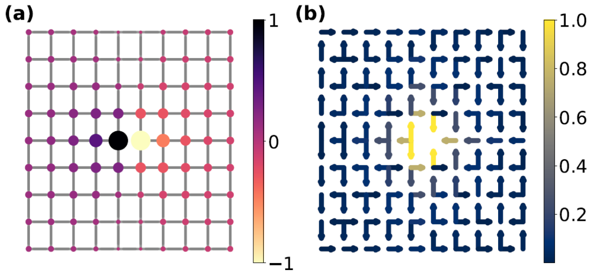

FIG. 17 Impact of a link failure in a square lattice with uniform edge weights. (a) Normalized change of the nodal potentials α_n for a single failing link located in the center of the network. Both the size of the nodes as well as the colorcode represent α_n. (b) Normalized change of the link flows F_j for the same topology. Arrows and color represent direction and strength of flow changes, respectively. Figure reproduced from (Strake *et al.*, 2018).

2. Spreading of failures

A deeper physical insight into the network flow rerouting problem is obtained by an analogy to discrete electrostatics. Using again the Woodbury matrix identity, Eq. (136) can be recast into the form

$$B\,\boldsymbol{\alpha} = \boldsymbol{q} \tag{141}$$

with the source term

$$\boldsymbol{q} = (1 - \underbrace{b_{rs}\boldsymbol{\nu}_{rs}^{\top}B^{*}\boldsymbol{\nu}_{rs}}_{=:\chi_{rs}})^{-1}F_{rs}^{(0)}\boldsymbol{\nu}_{sr}\,. \tag{142}$$

As the matrix B is a Laplacian matrix and the right-hand side is non-zero only at positions r and s with opposite sign, Eq. (141) is a *discrete Poisson equation* with a dipole source and $\boldsymbol{\alpha}$ is a dipole potential, see Ref. (Biggs, 1997). Indeed, if we compute the outage of a line in a rectangular square grid, we just recover a discretized version of the familiar electric dipole field as illustrated in Fig. 17. Thus, $\mathrm{LODF}_{e,\ell}$ depends on the orientation of the two lines e and ℓ and decreases as distance^{-2}.

Understanding the impact of line outages for arbitrary grid topologies is much more challenging. The main complexity arises from the network topology encoded in the Laplacian B, which can be highly irregular. Still we can get some insight using tools from algebraic graph theory (Kaiser and Witthaut, 2021a; Strake *et al.*, 2018).

Before we proceed to spatial failure spreading, we have a more detailed look at the right hand side of the Poisson equation (141). The strength of the dipole $|\boldsymbol{q}|$, more precisely the factor χ_{rs}, can be understood from the grid topology: If a unit power is injected at node r and withdrawn at node s, then χ_{rs} is the flow via the direct link (r,s) and $1-\chi_{rs}$ the flow via other non-direct pathways. Hence, we can view $1-\chi_{rs}$ as a measure of redundancy of line (r,s). Indeed, it can be rigorously related to topological redundancy measures (Guo *et al.*, 2021; Strake *et al.*,

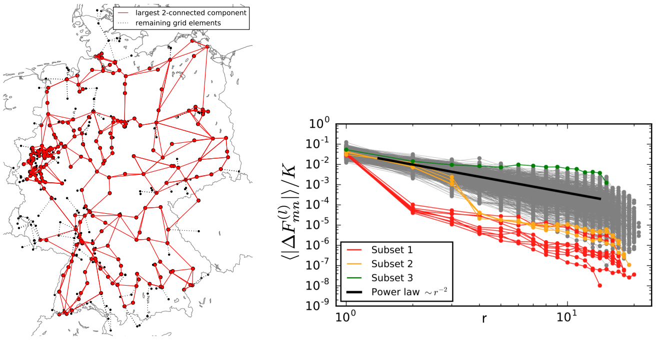

FIG. 18 Left: German transmission grid topology (220 and 380 kV)(Medjroubi *et al.*, 2015). Right: Double-logarithmic plot of transmitted power change $\langle|\Delta F_{mn}^{(\ell)}|\rangle(r)$ as function of distance r when a transmission line (ℓ) between 880 different pairs of nodes i, j was added. We averaged this quantity over all edges with the same distance r to the added line (ℓ), and perform an ensemble average over $R = 100$ realizations with randomly distributed generators and loads. For comparison the power law expected for a 2-dimensional regular grid $\Delta F \sim r^{-2}$ is shown (black line). The colored data belong to special subsets of added edges as discussed in the text. Error bars: 95% confidence level (Jung and Kettemann, 2016).

2018). An alternative approach to line outage problems has been introduced in (Ronellenfitsch *et al.*, 2017). Flow changes due to a failure can be decomposed into cycle flows as $\boldsymbol{\Delta F} = \boldsymbol{C f}$ using the edge cycle-incidence matrix (5). The cycle flows strength $\boldsymbol{f}$ is again determined by a discrete Poisson equation, now formulated on the dual graph.

3. Locality and the importance of distance

Intuitively, a transmission line outage should affect nearby lines more heavily than remote ones. In a regular square lattice, flow changes decay as distance^{-2} as discussed above. But how can we quantify this statement and what does nearby mean in a network with complex topology? These questions were studied using a spectral approach in (Jung and Kettemann, 2016; Kettemann, 2016; Labavic *et al.*, 2015; Rohden *et al.*, 2016).

The discrete Poisson equation (141) can be formally solved by decomposing the Laplacian B into its eigenvectors defined as $B\boldsymbol{\Phi}_j = \lambda_j \boldsymbol{\Phi}_j$ with indices $j = 1, \dots, \mathtt{N}$. Assuming the failure of a line (r, s) we obtain

$$\alpha_m = -\Delta b_{rs} \sin(\theta_r - \theta_s) \sum_{j=2}^{\mathtt{N}} \frac{\Phi_{jm}(\Phi^*_{jr} - \Phi^*_{js})}{\lambda_j}, \qquad (143)$$

using the generalized 'hot-start' linear response with edge weights (140), see also (Haehne *et al.*, 2019). Similarly, the flow changes at the remaining links are given by

$$\begin{aligned}\Delta F_{mn} =& b_{mn} \cos(\theta_m - \theta_n) \Delta b_{rs} \sin(\theta_r - \theta_s) \\ & \times \sum_{j=2}^{\mathtt{N}} \frac{(\Phi_{jm} - \Phi_{jn})(\Phi^*_{jr} - \Phi^*_{js})}{\lambda_j}. \end{aligned} \qquad (144)$$

For a regular grid of degree $2d$ the eigenvectors $\boldsymbol{\Phi}_j$ are plain waves and the eigenvalues λ_j can be obtained exactly, yielding (Kettemann, 2016)

$$\Delta F_{mn} \sim A_{mn} \Delta b_{rs} c_d \, |m - r|^{-d}. \qquad (145)$$

Here, c_d are constants. For $d = 2$, a regular square grid, the power law decay os with exponent 2 and $c_2 = 2\pi$. For a random graph one finds exponentially localized eigenstates, and thus an exponentially decaying response (Torres-Sánchez *et al.*, 2020), so that the disturbance due to the outage affects the power grid only in a finite range around the outage (Kettemann, 2016). This phenomenon is well known and originates from random scattering from nodes with random degree (Hata and Nakao, 2017) and/or random parameters (García-Mata *et al.*, 2017), so called Anderson localization (Anderson, 1958).

Numerical calculations based on the AC load flow equations, were found to be in very good agreement with Eq. (143), see (Jung and Kettemann, 2016). This study considers an addition of a new transmission line and confirms the generic power law decay of the change in transmitted power $\Delta F \sim$ distance^{-2} up to finite size corrections. As a more realistic grid topology, the effect of a change in transmission line capacity was studied in a model of the German transmission grid (Medjroubi *et al.*, 2015) shown in Fig. 18 (left). The largest 2-connected component of this grid was considered, with $\mathtt{N} = 260$ nodes and $\mathtt{L} = 479$ edges, homogeneous line parameter b_{ij} and power injections randomly chosen from a binary distribution, $P_i \in \{-P, P\}$. Distance is defined as the geodesic distance, see Sec. II. The resulting response behavior depends strongly on the location of the added line. Most locations result in a long range power law decay with an exponent, that is on average close to 2. However, there are certain classes of locations, denoted in the figure as subset 1 and subset 2, where the change results in an exponential decay beyond a certain length scale. Notably the regions around subset 2 are weakly connected to the remaining grid, forming weakly connected islands, explaining the fact that the disturbance decays exponentially at distances beyond these islands.

A different approach to understand the spatial pattern of flow rerouting is to adapt the measure of distance to the respective problem (Kaiser and Witthaut, 2021a; Strake *et al.*, 2018). Consider the line outage distribution factors $LODF_{e,\ell}$ for the IEEE 30-node test grid shown in Fig. 19, fixing a failing link ℓ in the right part of the network. The LODFs decay with the geodesic distance of two links, but the correlation is only moderately pronounced. This is not surprising as the geodesic distance

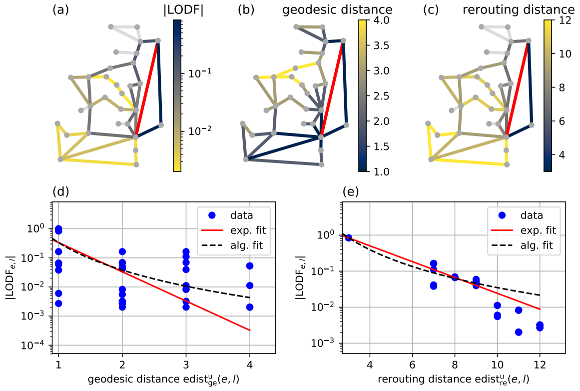

FIG. 19 Localization of the impact of line failures as seen with different distance measures. (a) Flow changes after the outage of a single line (marked red) in the IEEE 30-bus test grid. (b) Geodesic distance to the failing link. (c) Rerouting distance to the failing link well predicts the spatial distribution of the flow changes. (d,e) Flow changes $|\Delta F_e|$ vs. distance to the failing link ℓ on a logarithmic scale. One clearly observes that the rerouting distance used in (e) yields a higher correlation than ordinary geodesic distance shown in (d).

does not take into account the fact that flow rerouting requires *two* paths between the links ℓ and e, one to and one fro. We can define an alternative distance measure, the rerouting distance, which seeks for the shortest path from one end of link ℓ via e to the other end of the link ℓ. Numerical studies show that the correlation of rerouting distance to the LODFs is much stronger than for the geodesic distance (Strake *et al.*, 2018).

To find a perfect measure of distance requires to take into account all details of the Laplacian B, not just a single shortest paths. Indeed, the resistance distance (Klein and Randić, 1993) provides such a measure of distance and can be applied to line outages (Tyloo *et al.*, 2019). However, as this distance is calculated from the full matrix B, it does not offer a direct topological interpretation as a shortest path distance does.

4. The importance of community structures

Some power grids show a pronounced community structure. In the Scandinavian grid for example, Finland is connected to its neighbors only via two AC lines (Fig. 20 a). This weak topological connectivity induces also a weak electric connectivity: LODFs between two lines in different communities are significantly smaller than expected from their distance. This aspect is illustrated exemplary for the failure of a line in Sweden (Fig. 20 b). For most lines in Finland the respective LODFs are of the order of 10^{-7}, only some lines in the north near the connection to Sweden are slightly more affected. A more quantitative analysis is provided in Fig. 20 c, showing that LODFs between different communities are significantly suppressed, up to several order of magnitude, compared to LODFs within a community. Hence, a splitting into communities can strongly impede the spreading of failures (Kaiser *et al.*, 2021b). Remarkably, several other topological structures have similar or even stronger effects on failure spreading (Kaiser *et al.*, 2021a; Kaiser and Witthaut, 2021a): If the coupling between two parts of a grid can be described by an adjacency matrix of unit rank, then all mutual LODFs vanish exactly and the spreading of failures and cascades is suppressed entirely. The simplest realization of such a unit-rank coupling is given by a bridge (Guo *et al.*, 2021; Ronellenfitsch *et al.*, 2017), which is exploited in recent proposals for emergency measures to contain cascading failures (Bialek and Vahidinasab, 2021; Zocca *et al.*, 2021). These results emphasize the importance of structural features for the general robustness of electric power grids.

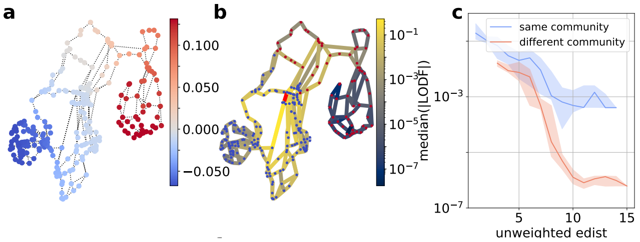

FIG. 20 The importance of community structures in the spreading of failures. (a) Community structure of the Scandinavian power grid obtained by spectral clustering. (b) Magnitude of the LODFs for a failing link at the border between Southern Norway and Sweden (red line). (c) Magnitude of the line outage distribution factors $|\mathrm{LODF}_{j\ell}|$ as a function of the unweighted edge distance of the transmission lines j, ℓ, comparing the cases when j and ℓ are in the same or in different communities. The line gives the median, the shaded area the 25%-75%- quantile. The grid data was taken from (Hörsch *et al.*, 2018a).

5. Multiple outages and collective effects

When two lines k and ℓ fail we cannot simply superpose the flow changes, but have to account for collective effects. To see this, assume that k and ℓ fail successively. In calculating the impact of the failure ℓ we must take into account that the flow F_ℓ already has changed due to the failure of k. The correct result for the impact of multiple line outage was derived in Sec. VII.A.1, which for two lines reduces to

$$\Delta F_e^{(k,\ell)} = \begin{pmatrix} \mathcal{L}_{e\ell} & \mathcal{L}_{ek} \end{pmatrix} \begin{pmatrix} 1 & -\mathcal{L}_{\ell k} \\ -\mathcal{L}_{k\ell} & 1 \end{pmatrix}^{-1} \begin{pmatrix} F_\ell^{(0)} \\ F_k^{(0)} \end{pmatrix}, \quad (146)$$

using the short-hand $\mathcal{L}_{e\ell} = LODF_{e,\ell}$ and denoting the failing lines in the superscript. Collective effects can have

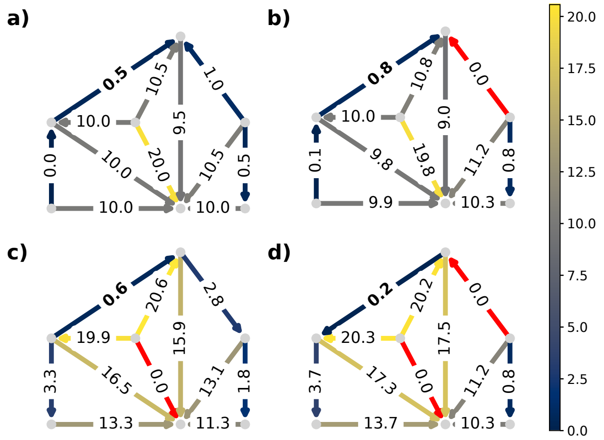

FIG. 21 Collective effects can lead to a complete reversal of the flow changes in an $N-2$ failure. The colour code on lines indicates the magnitude of flow, where red indicates failing links. (a) Flows in the initial unperturbed grid. (b),(c) Flow changes after individual failure of two links (ℓ and k respectively, marked red). In both cases, the flow on the top left link (e, bold font) is greater than in the unperturbed grid; $\Delta F_l^{(\ell)} \approx 0.3$, $\Delta F_l^{(k)} \approx 0.1$. (d) Flows after the simultaneous failure of both links ℓ and k. The flow on the top left link is *smaller* in magnitude than in the unperturbed grid and even changes its direction: $\Delta F_e^{(\ell,k)} \approx -0.7$. Figure reproduced from (Kaiser *et al.*, 2020b).

surprising consequences. First, the impact of a line failure may be partly compensated by the intentional removal of a second line. So suppose that the failure of line ℓ has led to an increase of the flow on a critical line e. In many cases we can find another line k such that

$$|F_e^{(k,\ell)}| \leq |F_e^{(\ell)}|. \tag{147}$$

This concept was previously discussed in (Motter, 2004; Witthaut and Timme, 2015) for different types of flow networks and we will come back to this in section VII.D. More surprisingly, we can find cases where the collective impact of two outages is opposite to the impact of two isolated outages, i.e.

$$\Delta F_e^{(k)}, \Delta F_e^{(\ell)} > 0 \quad \text{but} \quad \Delta F_e^{(k,\ell)} < 0. \tag{148}$$

An example of this effect is shown in Fig. 21 and a more detailed discussion can be found in (Kaiser *et al.*, 2020b). A further analysis shows that collective effects are particularly strong whenever the mutual LODFs, more precisely the expression $\sqrt{\mathcal{L}_{k\ell}\mathcal{L}_{\ell k}}$, is large.

B. Robustness of power grids and critical infrastructures

The outage of a transmission element leads to rerouting of currents and power flows as analyzed in the previous section. This may eventually cause secondary failures of other transmission elements, which can result in a large scale cascade affecting the entire grid. In this section we investigate the grid vulnerability to secondary failures and analyze the weak spots of a network.

1. Why secondary failures?

If the current on a overhead transmission line is too large, it will heat up due to Ohmic losses, which may lead to line sag and eventually a short-circuits fault as discussed in section V.B. Commonly, strict security rules are implemented to avoid such faults such that the current on a line ℓ may not exceed a certain limit, the line rating, $|I_\ell| \leq I_\ell^{\max}$. If voltages are close to the setpoint and losses are small, this directly translates into an upper limit for the real power flow,

$$|F_\ell| \leq F_\ell^{\max}. \tag{149}$$

A violation of this limit typically leads to an emergency shutdown if the line is appropriately monitored. The line will not be damaged, but it is no longer available for power transmission. In practice, one differentiates between short-term and long-term loads of a transmission line. A higher loading may be acceptable on short terms, such that a higher line rating applies. Furthermore, not only currents but also voltages are important for grid stability. Strict security rules apply to the voltage level at every substation, which must remain within a certain interval around the grid reference level. A decreasing voltage may indicate a looming voltage instability as discussed in section V.A.

2. Critical links: A graph theoretic perspective

Consider a heavily loaded power transmission grid which is no longer $(N-1)$-secure. Some transmission lines may be critical in the sense that, if they fail, secondary overloads occur. But which lines are critical and which lines are prone to secondary overloads? These question can be answered by extensive numerical simulations – but a better analytic understanding would clearly be helpful. Obviously, we expect outages of lines with a high load or flow to be more harmful, but this is certainly not the whole story. It is equally important whether the grid bears enough redundancy to cope with the failure. These aspects can quantitatively understood using tools from graph theory (Witthaut *et al.*, 2016).

So assume that a line (a,b) fails, which initially carried the real power flow $F_{a\to b}^{(0)}$ from node a to node b. After the failure, the power must be rerouted from a to b via different pathways. Graph theory now provides a necessary condition for this to be possible. The Edmonds-Karp algorithm yields the maximum flow that can be transmitted from a to b respecting the line limits, which we call

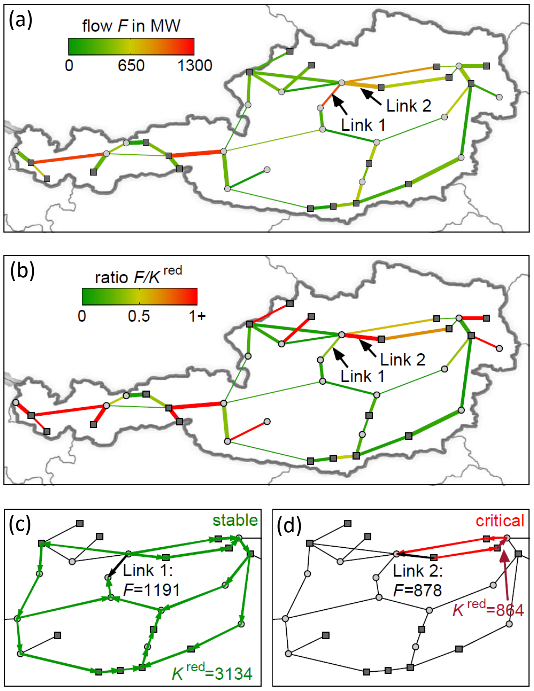

FIG. 22 (a) Real power flows F_{ab} in MW in a test grid based on the Austrian grid topology. The two marked links are investigated in detail. (b) The ratio of the flow and redundant capacity $F^{(0)}_{a\to b}/K^{\rm red}_{a\to b}$ provides a powerful indicator for critical links. (c,d) Illustration of rerouting pathways after the outage of link 1 and 2, respectively. Several rerouting pathways exist for link 1 such that the redundant capacity $K^{\rm red}$ is rather high, a line failure is uncritical. In contrast, a failure of link 2 will cause secondary outages. The min-cut for the rerouting problem consists of a single link (marked by an arrow). This bottleneck has a free capacity of 864 MW such that a rerouting is impossible. Grid data is based on (Hutcheon and Bialek, 2013) with slight adaption of power injections. Austria was artificially islanded for illustrative purposes.

the *redundant capacity* $K^{\rm red}_{a\to b}$ of the line (a,b). The algorithm also yields the set of edges limiting the flow from a to b, referred to as the minimum cut in graph theory. Hence, we can obtain both a measure of redundancy and the locations of the bottlenecks in the grid.

In summary, a necessary condition for having a feasible power flow after the outage of line (a,b) is given by $|F^{(0)}_{a\to b}/K^{\rm red}_{a\to b}| \leq 1$. In practice, secondary overloads will typically occur earlier as power flows are generally not maximum flow network flows but have to respect Kirchhoff's laws. An example is shown in Fig. 22 for a semi-synthetic power grid based on the structure of the Austrian transmission grid. One of the marked links carries a high real power flow of about 1.2 GW. It is uncritical because it has a high redundant capacity. The second line has a lower flow (≤ 0.9 GW), but lacks redundancy. The ratio $|F^{(0)}_{a\to b}/K^{\rm red}_{a\to b}|$ is larger than one such that an outage of this line will always lead to secondary outages and a fragmentation of the grid. Applying Edmonds-Karp directly yields the bottleneck which limits the redundancy.

Extensive numerical tests for different power system models (Witthaut *et al.*, 2016) show that the ratio $|F^{(0)}_{a\to b}/K^{\rm red}_{a\to b}|$ is a powerful predictor for critical links. Furthermore, one can improve power system robustness by strengthening the bottlenecks (Rohden *et al.*, 2017).

3. Generation variability and critical fluctuations

Up to now we have investigated potential overloads and cascades assuming that the power injections are fixed and perfectly known. But even if we known the scheduled values, there are always some residual fluctuations of generation and demand. How do these fluctuation affect power system stability? Is it possible that the grid is safe on average, but that overloads occur during stochastic peaks which may eventually trigger a cascade?

These important question were addressed in (Nesti *et al.*, 2018) using a quasi-static picture. The power injections $\boldsymbol{P}$ are treated as Gaussian random variables with mean $\boldsymbol{\mu}_P$ and correlation matrix $\epsilon\Sigma_P$. The essential quantities in a security assessment are the relative line loads $L_\ell := F_\ell/F_\ell^{\max}$, which are determined by the power injections via

$$\boldsymbol{L} = \underbrace{\mathrm{diag}(F_1^{\max},\ldots,F_{\rm L}^{\max})^{-1} B_d E^\top B^*}_{=:\Upsilon} \boldsymbol{P}$$

using Eq. (33). Hence, the line loads $\boldsymbol{L}$ are also Gaussian random variables with mean $\boldsymbol{\mu}_L = \Upsilon\boldsymbol{\mu}_P$ and correlation matrix $\epsilon\Sigma_L = \epsilon\Upsilon\Sigma_P\Upsilon^\top$. A line ℓ gets overloaded if $L_\ell > 1$. In the limit of small fluctuations $\epsilon \to 0$ one can derive the probability for this event using large deviation theory

$$\mathcal{P}(|L_\ell| \geq 1) \approx \exp\left(- \frac{(1-|\mu_{L,\ell}|)^2}{2\epsilon\sigma_\ell^2} \right), \qquad (150)$$

where $\sigma_\ell^2 = (\Sigma_L)_{\ell\ell}$. While for non-vanishing fluctuations this is an approximation it was found that it is very useful for ranking purposes: The smaller the ratio $(1-|\mu_{L,\ell}|)^2/\sigma_\ell^2$ the more likely is an overload of a line ℓ.

An example of such a probabilistic contingency analysis is shown in Fig. 23 for the SciGrid model of the German power grid. The nominal power injections were determined via an OPF and the correlation matrix Σ_P was derived from a statistic analysis of actual generation time series. One finds that the vulnerable lines where $\mathcal{P}(|L_\ell| \geq 1)$ is largest, do not coincide with the most heavily loaded lines. High loads are one important indicator for vulnerability, but the network structure and the generation variability enter the overload probability on an equal footing via the effective variance σ_ℓ^2.

One can extend this analysis and ask which power injections typically lead to the failure of a single line. In mathematical terms: What is the conditional probability

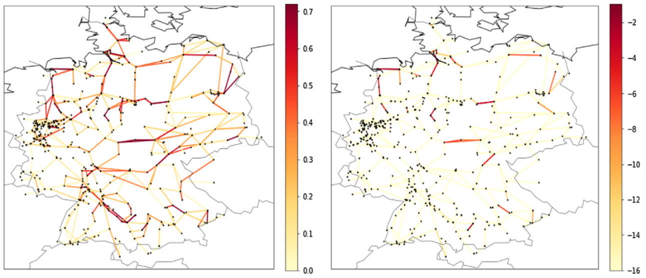

FIG. 23 Fluctuations of power generation and consumption can induce overloads of transmission lines (Nesti *et al.*, 2018). Left: Nominal line loads $|\mu_{L,\ell}| = |\langle L_\ell \rangle|$ in the Scigrid model of the German power grid. The nominal operation is determined from 1-hour averages of the renewable feed-in and load. The feed-in of the dispatchable power plants and the power flows are then computed via a linear OPF (see Sec. III.B). Right: Probability of a transmission line overloads $\mathcal{P}(|L_\ell| \geq 1)$ when the true power injections fluctuate around the nominal values. Vulnerable line are identified by small values of the indicator $(1 - |\mu_{L,\ell}|)^2/\sigma_\ell^2$. Figure reproduced from (Nesti *et al.*, 2018).

distribution of $\boldsymbol{P}$ given that $|L_\ell| \geq 1$, i.e. given that the line ℓ is overloaded? For $\epsilon \to 0$ this probability distribution gets sharply concentrated around the vector

$$\boldsymbol{P}^{(\ell)} = \boldsymbol{\mu}_P + \sigma_\ell^{-2}[\mathrm{sgn}(\mu_{L,\ell}) - \mu_{L,\ell}]\Sigma_P \Upsilon^\top \boldsymbol{e}_\ell, \qquad (151)$$

where sgn denotes the sign function and $\boldsymbol{e}_\ell$ is the ℓth unit vector. That is, there is a typical injection pattern leading to an overload of a line given that fluctuations are small but non-zero – which is plausible assumption for large power transmission grids. An important conclusion is that a line failure is *not* necessarily triggered by large fluctuations in the neighborhood, but can be triggered by the cumulative effects of small unusual fluctuations in the entire network. Correlations of the power injections, for instance by a sudden large-scale increase in wind power generation, play a key role for such an outage.

C. Cascades of failures and large scale blackouts

The outage of a transmission line leads to a rerouting of power flows which may cause secondary overloads as discussed above. In this section we discuss how this mechanism leads to a cascade of failures and how such a cascade propagates through the grid.

1. Simulating cascading failures

Cascading failures are often simulated in a quasistatic picture. One computes a series of stationary states of the grid by solving the AC (25) or DC load flow equations (32), where the topology changes as elements of the grid fail. The basic steps of a cascade may be simulated with the following algorithm:

```
for all branches $t$ that may fail do
  Remove trigger link $t$
  repeat
    Solve AC/DC load flow equations
    for all branches $\ell$ do
      if branch $\ell$ is overloaded then
        Remove branch $\ell$ from grid
      end if
    end for
  until No further overloads or grid disconnected
end for
```

More advanced simulations can include aspects of voltage stability as well as actions by the grid operators, as for example load shedding, the immediate disconnection of consumers to reduce the grid load.

We note that a wide body of literature on cascading failures exists in the statistical physics literature. Purely topological approaches based on percolation theory are particularly popular as they allow for analytic solutions (see, e.g. (Albert *et al.*, 2004, 2000; Newman, 2012)). However, the applicability of topological models to power grid stability is limited as discussed in (Bompard *et al.*, 2015; Hines *et al.*, 2010; Korkali *et al.*, 2017). Topological models and measures can provide some general insights into the vulnerability of networks (see, e.g. (Galindo-González *et al.*, 2020)), but they may be misleading when applied to particular grids. In particular, they neither capture the physics of power flows nor the heterogeneity and localization of power generation and consumption.

2. Local versus non-local propagation

How do cascading failures propagate through a power grid? Do subsequent failures occur in close proximity or can they jump to remote areas of a grid?

A prime example of a locally propagating cascade has been observed during the 2006 Western European Blackout (Union for the Coordination of Transmission of Electricity, 2007). The cascade was triggered by the shutdown of a line and a switching event in North-western Germany. In every step of the cascade, flow was rerouted to the next available routes in the southeastern direction causing secondary failures along these routes.

However, secondary outages can also take place at rather long distances from the initial failure. A rather simple reason is that also small flow changes can cause a line outage, if a line was already heavily loaded before. In particular, a failure of line ℓ causes a secondary overload of line e if (assuming that $F_e^{(0)} > 0$ w.l.o.g.)

$$F_e^{(0)} + LODF_{e,\ell} F_\ell > F_e^{\max} \Leftrightarrow LODF_{e,\ell} F_\ell > F_e^{\max} - F_e^{(0)}. \qquad (152)$$

Hence, a secondary outage occurs if either the flow change $\Delta F_e = LODF_{e,\ell} F_\ell$ is large or the line e was heavily loaded before the outage such that $F_e^{\max} - F_e$ is small.

While the flow changes ΔF_e are strongest in the vicinity of the failing line ℓ, little can be said about the initial line loadings $F_e^{(0)}$. They are determined by the grid topology as well as the power injections $\boldsymbol{P}$ and thus change in every hour. Hence, also the weak spots of a grid do vary.

The situation becomes more involved if we go beyond the linear DC Approximation. For instance, voltage instabilities have played an important role during the blackout in the Western USA in July 1996, where strongly nonlocal impacts were observed (Hines *et al.*, 2017; Venkatasubramanian and Li, 2004).

3. Influence graphs

Influence Graphs were proposed in (Hines *et al.*, 2017) to describe the propagation of cascades and understand non-local effects. This description is based on statistical analysis of a huge number of cascading failures simulated with a detailed physical model of the grid. The simulation data is used to determine the conditional probability $\mathcal{R}_{j,i,m}$ that a line j fails in generation $m+1$ of a cascade given that line i failed in generation m. It turns out that probabilities do not change much with m as long as $m \geq 1$. Only the first generation $m = 0$ is different, as the grid in the initial state is typically $(N-1)$-secure such that failures are less probable. Hence cascading failures are readily characterized using two matrices $\mathcal{R}_0, \mathcal{R}_1 \in \mathbb{R}^{\mathtt{L}\times\mathtt{L}}$ with elements $\mathcal{R}_{j,i,0}$ and $\mathcal{R}_{j,i,1+}$ respectively. An elementary example of a power grid and the reconstructed influence graph is shown in Fig. 24. A refined treatment including multiple line outages as separate states in a Markov chain model, was proposed in (Zhou *et al.*, 2020).

The influence graph can be used to identify critical lines as follows. If $\mathcal{P}_{i,m}$ is the probability that line i fails in generation m, then in the following generation

$$\mathcal{P}_{j,m+1} = \sum_i \mathcal{R}_{j,i,m}\mathcal{P}_{i,m}. \tag{153}$$

Introducing a vectorial notation, $\boldsymbol{\mathcal{P}}_m = (\mathcal{P}_{1,m}, \ldots, \mathcal{P}_{\mathtt{L},m})^\top$ the probabilities evolve as $\boldsymbol{\mathcal{P}}_1 = \mathcal{R}_0\boldsymbol{\mathcal{P}}_0$ and $\boldsymbol{\mathcal{P}}_{m+1} = \mathcal{R}_1\boldsymbol{\mathcal{P}}_m$ for all following steps $m = 1, 2, \ldots$. The probability that a line j failed at some time during a long cascade is thus given by

$$\boldsymbol{\mathcal{P}}_\infty = \boldsymbol{\mathcal{P}}_0 + \sum_{m=0}^{\infty} \mathcal{R}_1^m \mathcal{R}_0 \boldsymbol{\mathcal{P}}_0.$$

We can now analyze which elements have the largest impact on cascading failures. To this end one can calculate how the cumulative failure rate $\mathcal{P}_{\text{tot}} = \sum_j \mathcal{P}_{\infty,j}$ changes if a single row i of the matrices is $\mathcal{R}_0, \mathcal{R}_1$ is modified, representing an upgrade of the respective line i. One find that most upgrades have little effect, but some lines lead to a drastic change of $\mathcal{P}_{\text{tot}}$. The corresponding lines represent the critical lines of the grid.

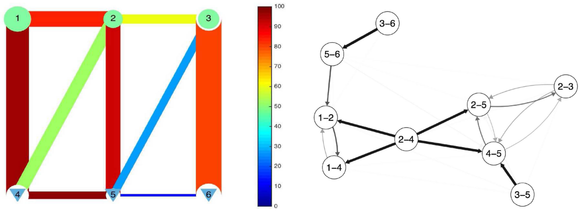

FIG. 24 Influence graphs are used to describe the propagation of cascading failures and to identify critical infrastructures: Left panel: Power flows in an elementary test grid consisting of six nodes. Right panel: Influence graph summarizing the likeliness that failure of one line induces the failure of another line. The nodes of this influence graph correspond to the lines in the original grid as identified by their endpoints. Figure adapted from (Hines *et al.*, 2017).

4. Statistical analysis of cascading failures

The preceding sections have provided a microscopic picture of how flows are rerouted and how cascades propagate in electric power grids. But how do these aspects manifest in real-world large scale grids under various operating conditions? A large scale statistical analysis of these questions was recently provided by Yang et al. (Yang and Motter, 2017) using a high quality model of the three North-American synchronous power grids (Eastern, Western and Texas Interconnection). The utilized cascade model was significantly extended in comparison to the elementary model of Sec. VII.C.1 including load shedding, generator adaption and a model for transmission line overheating. A huge number of cascades was simulated for a variety of different snapshots of the grid: different points in time with generation and load patterns. All cascades were triggered by the simultaneous failure of three lines randomly selected from the entire grid (Western, Texas) or from a certain grid area (Eastern Interconnection). The authors then evaluated the probability $\mathcal{P}_\ell^{(p)}$ that a line ℓ fails during a cascade as well as the probability $\mathcal{P}_\ell^{(s)}$ that a line ℓ is disconnected from the grid carrying no load after the cascade.

The first important result of the statistical analysis is that coreness is an important factor that determines the probabilities $\mathcal{P}_\ell^{(p,s)}$ (see Fig. 25). Links with a higher coreness are more strongly connected and thus offer more options for flow rerouting. As a consequence they are more likely to suffer failures (the fraction of links with $\mathcal{P}_\ell^{(p)} > 0$ increases with the coreness) and they also have a higher average value of $\langle\mathcal{P}_\ell^{(p)}\rangle$. In contrast the probability to become disconnected (i.e. the fraction of links with $\mathcal{P}_\ell^{(s)} > 0$) decreases with the coreness: Links with coreness 1 can be disconnected by a single failure while links with higher coreness have multiple connections to the grid and are thus hardly disconnected. Notably, the average $\langle\mathcal{P}_\ell^{(s)}\rangle$ still increases with the coreness. In this

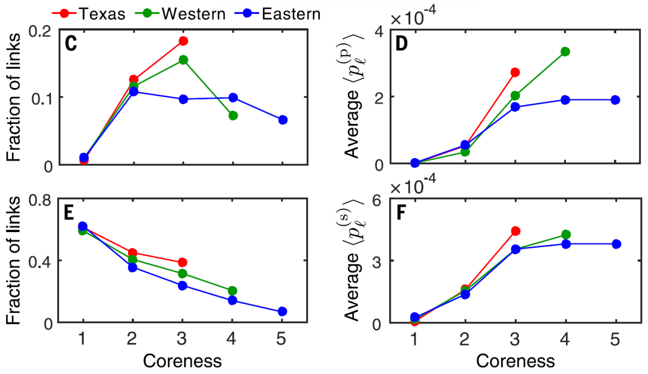

FIG. 25 Statistical analysis of cascading failures: The coreness of a link determines its vulnerability to fail (upper panels) or to be disconnected (lower panels) in a cascade of failures (Yang and Motter, 2017). The panels show the fraction of lines that (C) fail or (E) get disconnected in at least one cascade. (D) probability of failure $\langle \mathcal{P}_\ell^{(p)} \rangle$. (F) probability of disconnection $\langle \mathcal{P}_\ell^{(c)} \rangle$ averaged over all cascades and operating conditions. Simulations were carried out for the three North American grids for various operating conditions, see text for details. Figure adapted from (Yang and Motter, 2017).

analysis it should be noted that the vast majority of all links have a coreness of 2.

In a second step, the authors investigated the vulnerable lines of the grids, i.e. lines with a high probability of failure $\mathcal{P}_\ell^{(p)} > 0.0005$. It was found that the set of vulnerable lines is surprisingly small, including for instance only 48 out of 7637 lines in the Texas interconnection. Moreover, there is a significant overlap of the vulnerable sets between different grid snapshots. That is, generation and load patterns determine the vulnerability only to a limited extend – many lines are vulnerable for various different operating conditions. These findings raise the hope that grid stability can be significantly extend with comparably few grid extensions.

Finally, we are led to the question which trigger events are particularly critical for grid stability. To answer this question the authors analyzed all cascades causing a load shedding above 300 MW. It was found that in these cases, the three trigger events are typically rather close to each other and close to the vulnerable set of the grid both in terms of geodesic network distances and geographic distances. This corresponds to our prior findings that flow rerouting is predominantly local.

5. The size of cascading failures

Cascades of failures can cause large scale power outages. Statistics of the size of power outages are available for a variety of power grids as shown in Fig. 26 for the North-American power system. One observes that large scale outages are actually *not* rare events, that is, the likeliness $\mathcal{P}$ of an outage vanishes 'slowly' with the size of the outage $N_{\rm out}$. Indeed, it has been claimed that the distribution shows a power-law behavior

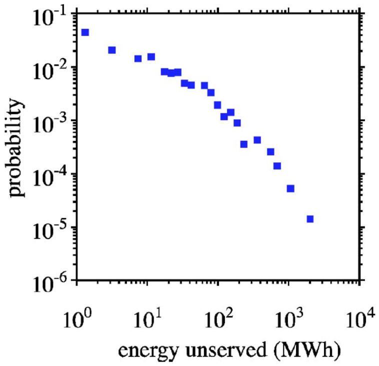

FIG. 26 Statistics of power outages in the North American power grids (1984-1998): the empirical probability of a power outage as function of the outage size on a logarithmic scale. The data suggests a power law distribution with exponent $1.3 \leq \beta \leq 2.0$. Figure reproduced from (Dobson *et al.*, 2007).

$$\mathcal{P} \sim N_{\rm out}^{-\beta}$$

for large $N_{\rm out}$ with an exponent $1.3 \leq \beta \leq 2.0$ for various grids (Dobson *et al.*, 2007). While it is generally hard to strictly establish a power law from empirical data (Clauset *et al.*, 2009), the statistics clearly indicate that large-scale outages occur regularly.

A detailed analysis of the statistics of cascading failures including empirical statistics was provided by Dobson and colleague and is summarized in (Dobson *et al.*, 2007). They have analyzed outage statistics both in detailed numerical models as well as in coarse-scaled model admitting a closed form solution (Dobson *et al.*, 2005). This model reduces a cascade to three essential elements:

- Many elements with heterogeneous loading: The model considers N infrastructure elements whose initial load L_0 is drawn at random from a uniform distribution in the interval $[0, L_{\rm max}]$. For simplicity we normalize all quantities such that $L_{\rm max} = 1$.

- Cascade mechanism: If the loading of an element exceeds a limit $L \geq L_{\rm fail}$, then this element fails and the loading is distributed to other elements. For simplicity we assume that the loading of all other elements then increases by the value ΔL_1.

- Initial trigger: The cascade is triggered by some initial failures increasing the initial load of all elements by an amount ΔL_0.

For $L_{\rm fail} = 1$, $\Delta L_0 + \Delta L_1 N \leq 1$ the number of failing elements N_{out} follows a quasi-binominal distribution

$$\mathcal{P}(N_{\text{out}} = k) = \binom{N}{k} \Delta L_0 (\Delta L_0 + k \Delta L_1)^{k-1} \times (1 - \Delta L_0 - k \Delta L_1)^{N-k} . \qquad (154)$$

If $\Delta L_1 \ll 1/N$ this distribution is strongly peaked around the mean. But if ΔL_1 increases and approaches the value $1/N$ the system approaches a critical point with a power law distribution

$$\mathcal{P}(N_{\text{out}} = k) \sim k^{-1.5}, \qquad (155)$$

providing a fair fit to the empirical results.

But why should a power system remain critical over many years? Dobson et al argue that criticality emerges in a self-organized way (Dobson *et al.*, 2007). The loads in the system are increasing year by year, in terms of the model L_{fail} decreases and ΔL_1 increases. As the system approaches the critical point the probability and size of power outages increases and countermeasures are implemented, for instance via an extension of infrastructures. Hence, the system remains close to the critical point. This behavior has been reproduced in a detailed numerical model (Carreras *et al.*, 2002), where power dispatch and cascades occur on short time scales (cf. Sec. III.B and VII.C.1) and load and infrastructures evolve on much slower time scales. In the model, the slow dynamics brings the power system close to criticality and such large scale cascades become likely. It must be noted that the hypothesis of self-organized criticality is highly controversial as summarized in (Fairley, 2004). Different explanations were put forward in (Nesti *et al.*, 2020), relating power law distributions in outages sizes to power law distributions in city sizes, and in (Kaiser and Witthaut, 2021b).

6. Transient effects in cascading failures

Our previous analysis of cascading failures was restricted to a quasi-static picture. We considered the existence and the properties of the steady-state after the failure of a transmission line, neglecting any dynamic. However, the existence of a stable state after a line failure is only a necessary condition for grid stability, not a sufficient one. It is not a priori clear that the grid will end up in this state, but there are also other possibilities: (i) It is not guaranteed that the system relaxed to a fixed point after failure. Instead, it can also relax to a limit cycle or another attractor as discussed in section V.C.3. (ii) Second, even if the system relaxes to the desired steady state, it may violate operational constraints during the relaxation, which might also cause secondary outages. This relates to the aspect of survivability introduced in section V.C.3. As a consequence, transient effects can increase the vulnerability of grid and a quasi-static picture can miss important threats to stability (Simonsen *et al.*, 2008).

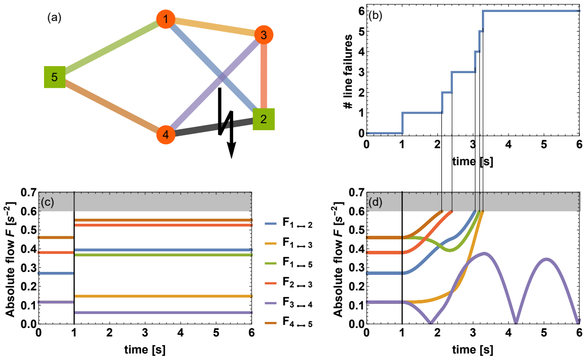

FIG. 27 Transient effects can increase the vulnerability of a grid to cascading failures. (a) An elementary test grid with two effective generators ($P = +1.5\,\text{s}^{-2}$, squares) and three effective consumers ($P = -1\,\text{s}^{-2}$, circles). All lines have $K_{ij} = 10/6$ and $F_{ij}^{\max} = 1$. At time $t = 1$ s, the line $(2, 4)$ fails. (b) In a full dynamical study, line ratings are exceeded transiently, leading to secondary line outages. Shown is the number of failed lines as a a function of time. (c) In a quasi-static picture, the grid immediately relaxes back to a stable steady state that respects the line ratings. Shown are the steady-state line flows $|F_\ell|$ before and after the initial failure. (d) Time evolution of line flows $|F_\ell(t)|$ taking into account both the continuous dynamics and the outage of lines. Figure reproduced from (Schäfer *et al.*, 2018).

A detailed analysis of cascading failures, including transient overloads, was provided in (Schäfer *et al.*, 2018). The dynamics was modelled in terms of the aggregated dynamical model of Sec. III.C.9 and a line was instantaneously removed from the simulation when the flow exceeded a line rating $|F_{ij}(t)| > F_{ij}^{\max}$. The impact of such a transient outage is illustrated for an elementary test grid in Fig. 27, where a cascade is triggered by the failure of a single line $(2, 4)$ (panel a). In a quasi-static picture, the grid immediately jumps to a new stable steady state (panel c). However, the line ratings are exceeded transiently, leading to secondary failures of line $(4, 5)$ and eventually to a cascade disconnecting the grid.

Whether transient overloads are important depends crucially on grid properties, the line ratings $F_{ij}^{\max}$ and initial trigger that starts the cascade. The strongest impacts have been observed for heavily loaded grids, where the likeliness of secondary overloads more than doubles.

D. Braess' paradox

The loss of a transmission line can cause a blackout, either directly as discussed in section V.A or indirectly via a cascade of failures. But remarkably, also the reinforcement of a transmission line or the addition of a new line can induce a loss of stability (Coletta and Jacquod, 2016;

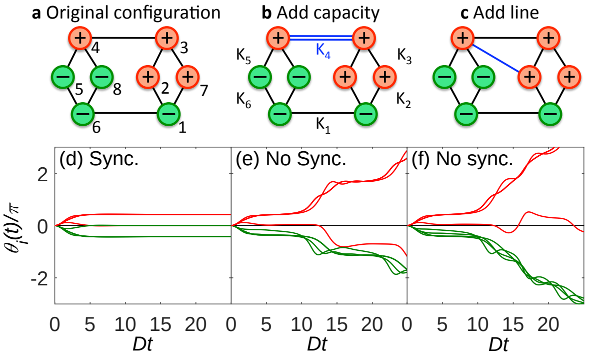

FIG. 28 Braess' paradox – Loss of the synchronous fixed point due to grid extensions. (a-c) Topology of the network. The vertices generate/consume the power $P_i = \pm P$, transmission lines have a capacity K. We consider the cases where (b) the capacity of one line is doubles and (c) a new line is added. (d-f) Dynamics of the grid given by the equations of motion 111 starting from the initial state $\theta_i(0) = \dot{\theta}_i(0) = 0$. The initial grid relaxes to a synchronized fixed point, while synchronization becomes impossible after the grid extensions. Parameters are $K = 1.03P$, $D = P$ and $J = 1$. Figure adapted from (Witthaut and Timme, 2012).

Witthaut and Timme, 2012). This surprising effect is demonstrated for an elementary test grid in Fig. 28. The initial grid relaxes to a synchronized fixed point, whereas synchronization becomes impossible after certain grid extensions, the synchronized fixed point has ceased to exist.

We can understand the loss of a fixed point using the cycle flow approach introduced in section VI.C.3. Increasing the capacity of a line as in Fig. 28 (b) will always lower the load on this specific line and thus relieve the grid. However, any fixed point must also satisfy the winding number constraint (124) for every cycle in the network. As a consequence all flows in the grid $\boldsymbol{F}$ are affected, which may cause the disappearance of synchronized phase-locked states, a prerequisite for normal grid operation. In particular, for the example shown in Fig. 28 (b) a cycle flow must be added in the counter-clockwise direction to still satisfy the constraint (124) after the line extension. But this would increase the load on lines $4 \to 5$ and $4 \to 8$ above the upper limit K which is not possible. The fixed point ceases to exist.

Remarkably, Braess' paradox can be used to improve grid stability. In certain situations it can be beneficial to shut down a transmission line on purpose to relieve another line (Motter, 2004; Witthaut and Timme, 2015), cf. Sec. VII.A.5. Similar effects were observed for other supply networks, starting from a seminal work on traffic networks by Dietrich Braess (Braess, 1968).

VIII. PERTURBATIONS, FLUCTUATIONS AND TRANSIENT DYNAMICS

Since the ascent of renewable energy sources, accompanied by increased trading and regulatory activities, power inputs and outputs increasingly fluctuate on time scales from seconds to hours and beyond. In addition, vastly more options for consumption patterns arise due to digitalization and globalization. Such perturbations and fluctuations require analyses of the state of a power grid as a driven, non-equilibrium system where voltages, voltage angles and flows are non-static and even non-stationary as they respond dynamically to time-varying signals.

In this section, we address key questions about perturbations and fluctuations in power grids. In a mathematical model for bulk grids, we illustrate in Sec. VIII.A how fluctuations of feed-in and consumed power translate to frequency fluctuations, highlighting their non-Gaussian statistics. We also highlight the impact of grid heterogeneities on non-Gaussian features and in Sec. VIII.B present driving response relations for networked systems explicitly taking into account any given grid topology. Beyond deriving the general form of linear response theory, we explain collectively emerging dynamic phenomena including resonances, bulk oscillations, localization and signal propagation in Sec. VIII.C. In Sec. VIII.D, we outline how the a Wentzel-Kramers-Brioullin (WKB) method helps to predict the probability of blackouts if rare but large fluctuations kick the system out of a stable phase-locked state. For fluctuations in production and consumption occurring simultaneously all over the grid, a natural implementation in the spirit of statistical mechanics amounts to consider ensembles of power grids (Sec. VIII.E) with possible applications to obtain macroscopic average quantities such as the market volume and market costs.

A. Frequency fluctuations from time series data

Dynamic driving signals continually change the overall state of a power grid. Due to fluctuations, the collective dynamics of electric power grids thereby is not only intrinsically out of equilibrium but also intrinsically non-stationary. Fluctuations often directly modify essential parameters of input and output and make them time-dependent, reflecting fluctuating power feed-in and consumption. One key example is a fluctuating power occurring as a time-dependent parameter $P_i(t)$, e.g. in the second order model (111). Such a driving signal especially impacts the frequency dynamics.

To analyze how the statistics of input power fluctuations influence the grid frequency, we first focus on the bulk frequency dynamics given by Eq. (87), assuming that the power imbalance is due to stochastic fluctua-

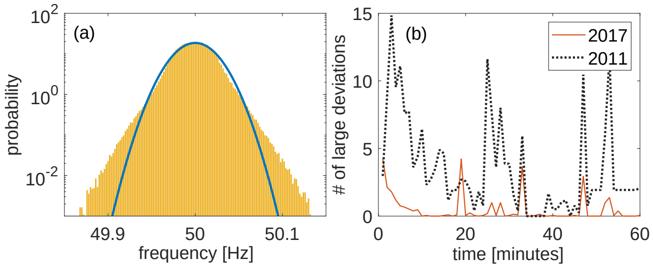

FIG. 29 Non-Gaussian frequency deviations, reduced number of extreme events. (a) Distribution of frequencies around set frequency (50Hz) in the Continental European Grid (yellow) deviates from best Gaussian distribution (parabolic blue solid line). In particular, the probability (per Hertz) of large events of more than 0.1 Hz frequency deviations is increased by more than a factor of ten compared to the Gaussian fit. (b) The counts of 'extreme events', i.e. number of frequency deviations larger than 0.1 Hz resolved for each minute, within full hours, accumulated for 2017 and 2011, respectively. Figure adapted from (Schäfer *et al.*, 2018) using data from (Reseau de Transport d'Electricite (RTE), 2017).

tions at at the grid nodes $i = 1, \ldots, \mathtt{N}$ with strength q_i,

$$\Delta P = \sum_{i=1}^{\mathtt{N}} q_i \xi_i(t) =: \bar{q}\bar{\xi}(t)\,. \tag{156}$$

In traditional analyses of power engineering, input fluctuations are either neglected or modeled to be of Gaussian nature, either white or colored noise, i.e. without any or with small temporal correlations, see e.g. (Schäfer *et al.*, 2017; Wood *et al.*, 2014; Zhang and Li, 2010). For Gaussian white noise power fluctuations, the resulting distribution of frequency deviations $\overline{\omega}$ is Gaussian with zero average and standard deviation $\sigma = \sqrt{\frac{\sum_i q_i}{2\eta J^2}}$. Such a Gaussian model neglects heavy tails observed in bulk frequency distributions (Gorjão *et al.*, 2020b; Schäfer *et al.*, 2018). As Fig. 29 illustrates, such heavy tails indicate that strong deviations from the reference frequency are orders of magnitude more frequent than a Gaussian model would predict.

Heavy-tailed frequency distributions may emerge either from heavy-tailed distributions of power fluctuations $\bar{\xi}(t)$ or the temporal variability of system parameters (Schäfer *et al.*, 2018). In particular, abrupt changes of power generation may cause large frequency deviations (Gorjão *et al.*, 2020a). Counting the number of 'extreme events' of the frequencies, defined as the frequency deviations of more than 100 mHz from the set frequency, and comparing these data between the years 2017 and 2011 reveals additional information (Fig. 29b), cf. (Schäfer *et al.*, 2018)). First, the total number of extreme events is reduced in 2017. Second, the number of these events is predominantly reduced in an interval of a few minutes after full hours. Third, the total number of threshold violations seems to still be substantial in the first few minutes as well as in about the 18th, the 33rd, and the 48th minutes after a full hour (each few minutes after a full quarter hour), hinting that switching the trading intervals from hourly (in 2011) to each quarter of an hour (in 2017), and thereby reducing the volume of trading per event together with changes in regulatory action, might have caused the reduction in the number of extreme frequency deviations. The histogram also hints at a characteristic time scale of response of frequency deviations at approximately two to four minutes delay. Both the details of such deviations as well as the generality of their occurrence remain poorly understood to date.

The resulting extreme events pose theoretical questions for analysis and serious practical challenges, e.g., for security assessment. Recent modeling work (Wolff *et al.*, 2019) illustrates that in power grids in which consumption, generation and transmission infrastructures are heterogeneous, fluctuating (wind) power injection at nodes that are weakly coupled to the grid particularly contribute non-Gaussian features to frequency deviations. Some further studies considered non-Gaussian effects, either focusing on theoretical aspects of how they may emerge or numerical evaluation of individual wind and solar data, see e.g. (Anvari *et al.*, 2016; Kashima *et al.*, 2015; Schmietendorf *et al.*, 2017; Totz *et al.*, 2020). In particular, the intermittent nature of short term wind fluctuations cause novel types of frequency and voltage fluctuations and thereby influence stability properties of grid dynamics (Schmietendorf *et al.*, 2017). Wind power induced fluctuations, quantified in terms of frequency deviation variance, moreover propagate along interconnected chains of synchronous machines in a characteristic way, with exponentially decaying amplitudes (Haehne *et al.*, 2019).

B. Network linear response theory for fluctuating power

How does the collective grid dynamics respond to input fluctuations? We review the general linear response theory valid for small perturbations with arbitrary time dependence (Haehne *et al.*, 2019; Zhang *et al.*, 2019, 2020). Consider a small perturbation $\delta P(t) = (\delta P_1(t), \ldots, \delta P_{\mathtt{N}}(t))^{\mathsf{T}}$ that at all nodes i results in phase deviations $\alpha_i(t)$ To first order in the deviation α_i, perturbations evolve according to the linear wave equation (112), as governed by the weighted graph Laplace matrix $L \in \mathbb{R}^{\mathtt{N}\times\mathtt{N}}$, defined in Eq. (113). For example, for homogeneous parameters, inertia $J_i = J$ and damping factor $D_i = D$ the response of the phase $\alpha_i(t)$ to dynamic perturbations, such as a change of power $\delta P_j(t)$ at node j, is given by (Haehne *et al.*, 2019),

$$\alpha_i(t) = \frac{J}{D^2\omega_R} \int_{-\infty}^{t} \sum_j \delta P_j(t') G_{ij}(t'-t) \frac{dt'}{\tau}, \tag{157}$$

with grid reference frequency ω_R, see section III.C.1. The propagator from node i to node j is defined by

$$G_{ij}(t'-t) = \sum_{n=1}^{\mathtt{N}} \sum_{\sigma=\pm 1} \frac{\phi_{ni}\phi^*_{nj}}{2\sqrt{1-\tilde{\Lambda}_n}}(-\sigma)e^{(1+\sigma\sqrt{1-\tilde{\Lambda}_n})\frac{t'-t}{\tau}}, \tag{158}$$

see Ref. (Haehne *et al.*, 2019) for the full derivation. Here, $1/\tau = D/J$ is the local relaxation rate (of a single node disconnected from other nodes) and $\tilde{\Lambda}_n = J/(D^2\omega_R)\Lambda_n$, where $\Lambda_n \in \mathbb{R}$ are eigenvalues and $\boldsymbol{\phi}_n \in \mathbb{C}^{\mathtt{N}}$ the corresponding eigenvectors of the generalized graph Laplacian matrix L Eq. (113), which is related to the stability matrix used in small signal stability analysis (Milano, 2010; Zhang *et al.*, 2012). For each eigenvalue of the generalized Graph Laplacian $\Lambda_n \in \mathbb{R}$ there are two eigenvalues of the linearized swing equations, Eq. (84), the linear wave equation (112), as given by $\varepsilon_{n\sigma} = -\mathrm{i}(1+\sigma\sqrt{1-\tilde{\Lambda}_n})/\tau$, where $\sigma = \pm$. Thus, the denominator in Eq. (158) is proportional to the difference of these eigenvalues, $2\sqrt{1-\tilde{\Lambda}_n} = \tau i(\varepsilon_{n+} - \varepsilon_{n-})$. Note that the relaxation rate of each mode is given by $\Gamma_{n\sigma} = -\mathrm{Im}\varepsilon_{n\sigma}$, which is identical to the local relaxation rate $1/\tau$ if $\tilde{\Lambda}_n > 1$, but differs by it by the term $\sigma\sqrt{1-\tilde{\Lambda}_n}/\tau$ if $\tilde{\Lambda}_n < 1$, yielding for the mode $\sigma = -1$ a slower relaxation in the grid than for individual nodes. This expression applies to any disturbance $\delta P_j(t)$ as long as its amplitude is sufficiently small (see Suppl. Eq. (S2) of (Tamrakar *et al.*, 2018) for a validity condition). Similar expressions can be obtained in response to a change of any of the system parameters, like a change of power capacitance $\delta K_{ij}(t)$ between nodes i and j (Kettemann, 2016; Manik *et al.*, 2017a; Witthaut *et al.*, 2016).

In the frequency representation of the linear response, we write the phase deviation $\alpha_i(t)$ as generalized Fourier series and expand its spatial dependence in terms of eigenvectors $\boldsymbol{\phi}_n$ of the generalized Laplacian L. Thereby we obtain (Auer *et al.*, 2017; Kettemann, 2016; Tamrakar *et al.*, 2018; Zhang *et al.*, 2019)

$$\alpha_i(t) = \int_{-\infty}^{\infty} \sum_{n=1}^{\mathtt{N}} c_n(\epsilon)\phi_{ni}e^{-\mathrm{i}\epsilon t}d\epsilon. \tag{159}$$

where $c_n(\epsilon)$ is the contribution strength of angular frequency ϵ at the n-th node. Likewise expanding the disturbance in a Fourier series, we obtain

$$\delta P_i(t) = \frac{D^2\omega_R}{J} \int_{-\infty}^{\infty} \sum_{n=1}^{\mathtt{N}} \eta_n(\epsilon)\phi_{ni}e^{-\mathrm{i}\epsilon t}d\epsilon. \tag{160}$$

Inserting these expansions for $\alpha_i(t)$ and $\delta P_i(t)$ into the linear wave equation (112) one finds, requiring that the equation is fulfilled for each term of the Fourier series, $\left(-\tau^2\epsilon^2 - \mathrm{i}2\tau\epsilon + \tilde{\Lambda}_n\right)c_n(\epsilon) = \eta_n(\epsilon)$. For a given disturbance, the Fourier component of the phase deviation $c_n(\epsilon)$ is thus given in response to the one of the disturbance $\eta_n(\epsilon)$. Inserting that expression for $c_n(\epsilon)$ back into the Fourier series one gets

$$\alpha_i(t) = \int_{-\infty}^{\infty} \sum_{n=1}^{\mathtt{N}} \left(-\tau^2\epsilon^2 - \mathrm{i}2\tau\epsilon + \tilde{\Lambda}_n\right)^{-1} \eta_n(\epsilon)\phi_{ni}e^{-\mathrm{i}\epsilon t}d\epsilon. \tag{161}$$

A linear response theory generalizing Eq. (157) to include inhomogeneous parameters and the presence of Ohmic losses has been derived in (Plietzsch *et al.*, 2019) and the case without inertia $J = 0$ has been analyzed in (Tyloo *et al.*, 2018). Zhang *et al.* (2019) disentangled the responses and analyzed spatio-temporal response patterns (see below) starting with a focus of driving one node at one frequency, i.e. $\eta_n(\epsilon) = \delta(\epsilon - \epsilon_0)\delta_{n,j}$ in Eq. (160) to obtain characteristics of linear response estimates analytically.

Given the phase deviation $\alpha_i(t)$ for time t and position i, one can calculate the temporal and spatial evolution of phase deviations, frequency deviations $(\delta f)_i(t) = \partial_t\alpha_i(t)$, and the rate of change of frequency deviations $\partial_t(\delta f_i(t))$ (Pagnier and Jacquod, 2019a) as well as time averaged moments of these quantities. Furthermore, moments of increments of frequency at node i, $f_{i\Delta t} = f_i(t+\Delta t) - f_i(t)$ (Haehne *et al.*, 2019) contain information about correlations at time scale Δt. In the following, we review the results obtained in linear response for these quantities for different types of non-stationary signals impinging on exemplary power grids structures.

C. Spatio-temporal responses from localized to resonant

1. Propagation of short duration disturbances

For disturbances that last for a short time compared to the local relaxation time $\tau = J/D$, the linear response at node i due to a power pulse

$$\delta P_k(t) = \delta P \delta_{kj}\tau\delta(t-t_0), \tag{162}$$

at time t_0 at node j by (157) yields, for times $t > t_0$

$$\alpha_i(t) = -\frac{J\delta P}{2D^2\omega_R}\sum_{n=1}^{\mathtt{N}}\sum_{\sigma=\pm 1}\frac{\phi_{ni}\phi^*_{nj}}{\sqrt{1-\tilde{\Lambda}_n}} \times e^{-(1+\sigma\sqrt{1-\tilde{\Lambda}_n})\frac{t-t_0}{\tau}}. \tag{163}$$

For meshed, spatially embedded grids and sufficiently large inertia analytical (Kettemann, 2016) and numerical results (Tamrakar *et al.*, 2018) show that disturbances propagate ballistically with velocity v such that the time $t > t_0$ when signals arrive at geometrical distance r from the position of the disturbance is given by

$$t - t_0 = r/v. \tag{164}$$

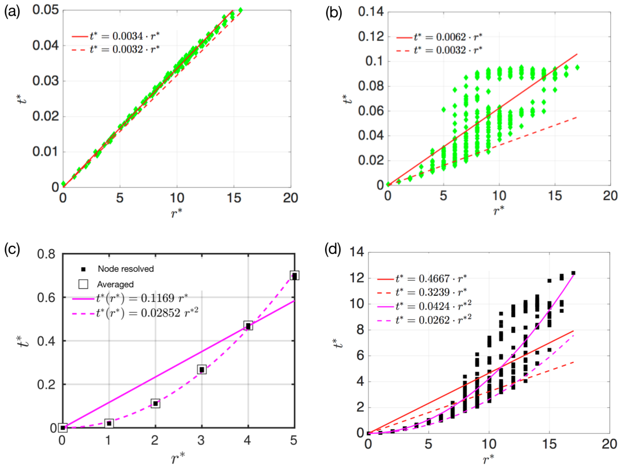

FIG. 30 Arrival time $t^* = (t - t_0)/\tau$ of a short pulse disturbance in units of $\tau = J/D$ versus geometric distance $r^* = r/a$ in units of transmission line length a. Green rhombi: numerical results for (a) square grid (b) German transmission grid topology, $KJ/(D^2\omega_R) = 10^5$, a realistic value for high voltage transmission grids. Ballistic Eq. (164) with fitted velocity v (Red line), and analytic velocity Eq. (165) (Red dashed line). Black squares: node resolved, unfilled squares: averaged over nodes at same distance (c) for Cayley tree with branching $b = 2$, (d) for German transmission grid. For (c) and (d) $KJ/(D^2\omega_R) = 10$. Diffusive Eq. (166) fitted (pink line) and with analytical Eq. (167) (pink dashed line). Ballistic Eq. (164) fitted (red line) and with analytic velocity (red dashed line). $\sigma = P/P_c = 0.1$ with critical power P_c for the respective grid. Figures modified from Ref. (Tamrakar *et al.*, 2018).

Here, the arrival time $t > t_0$ is defined as the time after an initial single-node disturbance in δP at time t_0, when phase deviations $\alpha_i(t)$ exceeds a threshold α_{th} (in the example of Fig. 30 $\alpha_{\text{th}} = 10^{-6} J\delta P/(D^2\omega_R)$ is chosen).

For homogeneous regular grids, the velocity v can be derived from response theory Eq. (163) (Kettemann, 2016; Tamrakar *et al.*, 2018)

$$v = a\sqrt{\frac{K}{J\omega_R}}\left(1 - \frac{P^2}{P_c^2}\right)^{1/4}, \tag{165}$$

with the length of a single transmission line a. $P < P_c$ where P_c is the critical power above which no stationary solution to the power flow equations exist. Remarkably, Eq. (165) gives lower bounds for the arrival times (164) both for regular square and German transmission grid topology (red dashed lines in Figs. 30 (a,b)). According to Eq. (165) the maximal velocity of disturbances in both regular and meshed real grid topologies increase with decreasing inertia J and decrease as $P \to P_c$.

For unmeshed grid topologies it was found in (Tamrakar *et al.*, 2018) that arrival times do not linearly but quadratically grow with distance r, resembling diffusion

$$t - t_0 = r^2/(4\mathcal{D}). \tag{166}$$

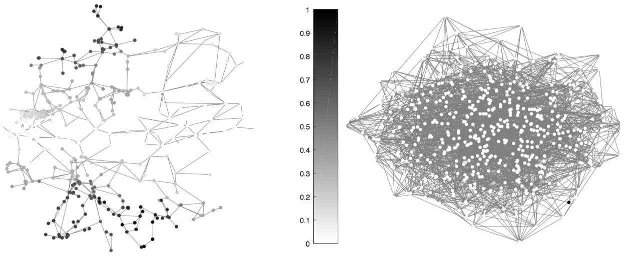

FIG. 31 Normalized Fiedler vector intensity $|\phi_{2,i}|/\max_n |\phi_{2,n}|$ relative to its maximum (visualised as black) for German transmission grid (left) featuring maximal intensity at the south and north borders and for a random grid with strong localization at a single node (black, on bottom right in right panel). Figures modified from Ref. (Torres-Sánchez *et al.*, 2020).

For Cayley tree graphs with branching number b the diffusion constant is derived as

$$\mathcal{D}(b) = \frac{\tau\Delta^2\sqrt{b}}{\sqrt{b} - 1}. \tag{167}$$

where $\Delta = (K/(J\omega_R))^{1/2}(1 - P^2/P_c^2)^{1/4}(\sqrt{b} - 1)$ is the positive Fiedler value, the spectral gap of the graph Laplacian, independent of the number of grid nodes `N`. This is confirmed by numerical calculations, illustrated in Fig. 30 (c) (dashed line). For low inertia $J < J_c$ the collective dynamics of coupled nodes results in diffusive spreading of disturbances also in meshed grids, see Fig. 30 (d). J_c is obtained from the condition that slow modes with small relaxation rate appear where the spectral gap (Fiedler value) Δ is smaller than local relaxation rate, $1/\tau = D/J$ (Tamrakar *et al.*, 2018). As Fig. 30 (d) illustrates, the spreading is more strongly delayed for some nodes and disturbances are localized in certain grid regions where nodes do not become excited above the threshold (at least within the observation time). Linear response theory may explain this feature as the response, Eq. (163) is proportional to the eigenvector amplitude of the Laplacian ϕ_{ni}. As noted above, the long time transient behavior is dominated by the Fiedler vector, the eigenvector with smallest nonzero eigenvalue, shown in Fig. 31 (left) for the German transmission grid topology, illustrating two geographic regions with high amplitudes. A similar result has been obtained in Ref. (Pagnier and Jacquod, 2019a) where the Fiedler vector of the weighted European transmission grid has been found to be localized at the southern and northern borders. Moreover, the global RoCoF was found to decay with increasing system inertia, which the authors related to the Fiedler vector intensity. In random graphs, the Fiedler vector can be strongly localized, even on a single node, Fig. 31 (right), so that single-node disturbances of sufficiently small amplitudes remain localized. Thus, strong randomness and inhomogeneity may result in localization of disturbances

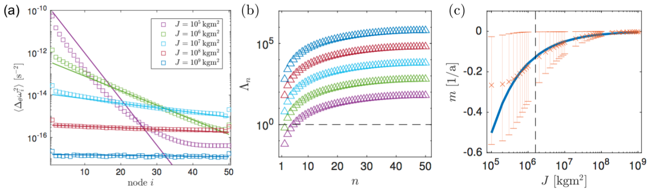

FIG. 32 (a) Variance of increments $\langle \hat{D}_{\Delta t}\omega_i^2 \rangle$ for chain of $\mathtt{N} = 50$ oscillators. Straight lines with slope $m = -1/\xi$ with Eq. (169). (b) Eigenvalues of Laplacian Λ_n for various inertia J. (c) Fits of slope m (orange) converge to analytical $m = -1/\xi$ Eq. (169) (blue) with increasing inertia J. Vertical dashed line: J_c. Error bars: 2σ confidence bound. Figures reproduced from Ref. (Haehne *et al.*, 2019).

as noted in Ref. (Kettemann, 2016), a phenomenon well known as Anderson localization (Anderson, 1958).

2. Propagation of stochastic disturbances

On large time scales, frequency control measures compensate feed-in fluctuations of renewable generators, as reviewed in Sec. III.D, thereby maintaining stable grid operation. However, on time scales below one second, grid frequency fluctuations increase with increasing wind power production (Haehne *et al.*, 2018). Moreover, the time scale separating local from inter-area modes is also of the order of one second (Zhang *et al.*, 2012). Are such fluctuations a local feature, for instance resulting from locally high wind power injection or do they affect grid dynamics over large ranges? To address this question, the sub-second grid frequency dynamics has been simulated by stochastically perturbing the grid. Model simulations of coupled nonlinear oscillator models with synthetically generated wind power feed-in time series (Haehne *et al.*, 2019) indicate that the variance of short-term fluctuations decays for large inertia exponentially with distance to the feed-in node. These findings hold both for linear chain networks and German transmission grid topology, see Fig. 32, in agreement with analytical results for the variance of frequency increment distributions

$$\langle (\hat{D}_{\Delta t}\omega_i)^2 \rangle = \frac{\langle (\hat{D}_{\Delta t}\delta P_1)^2 \rangle}{J K \omega_R} \exp\left(-\frac{d_{i,j}}{\xi}\right) \tag{168}$$

obtained by linear response theory, Eqs. (157, 158) for chain-like grids with $\mathtt{N} \gg 1$ nodes. Here $\hat{D}_{\Delta t} f(t) = f(t + \Delta t) - f(t)$ for any function f, and $\langle (\hat{D}_{\Delta t}\delta P_1)^2 \rangle$ is the second moment of the increment distribution of the disturbance at site $j = 1$. Thus, the second moment of the frequency increments decays exponentially with topological distance $d_{i,j} = i - 1$ from the position of the disturbance with correlation length

$$\xi = v\tau/2 = \sqrt{JK}/(2\sqrt{\omega_R} D). \tag{169}$$

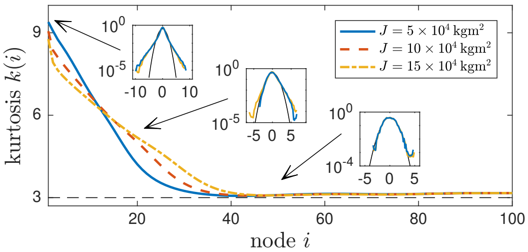

FIG. 33 Kurtosis k of frequency increment PDF in a chain of $\mathtt{N} = 100$ nodes. The frequency increment distribution $p(\hat{D}_{\Delta t}\omega_i)$ deforms only slowly towards an (almost) Gaussian distribution (insets, from left to right $i \in \{2, 20, 50\}$, $\theta = 0.01$ sec). Figure reproduced from Ref. (Haehne *et al.*, 2019).

Below a critical inertia, $J < J_c = \omega_R D^2 \mathtt{N}^2/\pi^2 K \approx 1.6 \cdot 10^6$ kgm^2, there are nonzero eigenvalues $\Lambda_n < 1$, cf. Fig. 32). According to Eq. (158) the amplitude of these modes decay with a rate smaller than $1/\tau$.

In sharp contrast, the kurtosis

$$k = \frac{\langle (\hat{D}_{\Delta t} f - \langle \hat{D}_{\Delta t} f \rangle)^4 \rangle}{\langle (\hat{D}_{\Delta t} f - \langle \hat{D}_{\Delta t} f \rangle)^2 \rangle^2}, \tag{170}$$

of frequency increments, quantifying deviations from Gaussian distribution ($k = 3$), is found to decay slowly, subexponentially, with distance from the disturbance. Thus, the non-Gaussian shape of frequency fluctuations, see Sec. VIII.A, persists over long ranges, Fig. 33.

In addition to these fundamental aspects, linear response arguments have been used in various applications. Using realistic grid models, it has analyzed how fluctuations affect the primary control effort (Tyloo and Jacquod, 2020), where additional inertia should be placed (Pagnier and Jacquod, 2019b) and which fluctuations source have the strongest impact on the grid (Gambuzza *et al.*, 2017).

3. Localization, distributed resonances and bulk oscillations

Which collective dynamical phenomena does linear response theory capture? Zhang et al. (Zhang *et al.*, 2019) analyzed the response dependence on grid topology, on the exact location of perturbed and responding nodes in the network, as well as on the frequency content of the power fluctuations driving the system and compared the results to the full nonlinear system dynamics. If a given node j is driven by power fluctuations at a given frequency ω, i.e. $\eta_n(\epsilon) = \delta(\epsilon - \omega)\delta_{n,j}$ in (160), three regimes with qualitatively different stationary responses emerge (see Fig. 34).

For large frequencies (compared to the range set by the Laplacian eigenvalues), the responses are strongly localized on the network, with amplitudes

$$c_i(\omega) \sim \mathsf{const} \times \omega^{-2d-1} \tag{171}$$

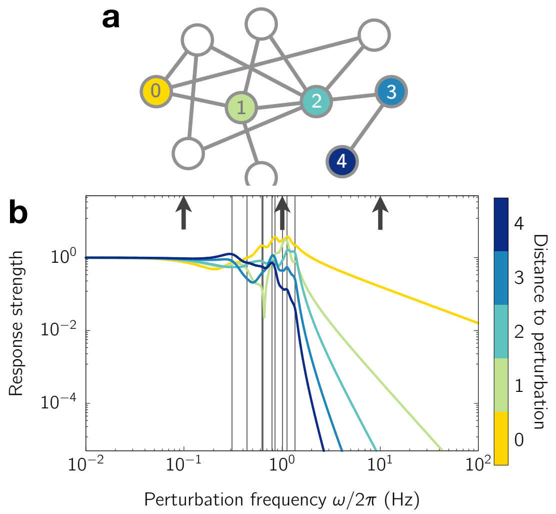

FIG. 34 Localization, distributed resonances and bulk oscillations. In a small network example (a), the joint implications on response strength (panel b) of driving one node (labeled 0) are illustrated as a function of driving frequencies (panels c,d,e) and at four selected response nodes (labeled 1, 2, 3, and 4). Whereas at high driving frequencies, responses are localized (algebraically in frequency, exponentially in inter-node distance), they are irregular across frequencies and among nodes in a resonance regime of intermediate driving frequencies. At low frequencies, globally homogeneous bulk oscillations emerge where the entire grid follows the driving signal (even if at only one node). All response strengths are quantified in terms of the amplitude of the frequency response relative to their low frequency limit as $\omega \to 0$. Figure courtesy of X. Zhang (cf. also (Zhang *et al.*, 2019)).

in Eq. (159) asymptotically (as $\omega \to \infty$) decaying exponentially with frequency and algebraically with graph-theoretical distance $d = d(i, j)$ response node i has from the driven node j. Here `const` is a constant independent of frequency yet contains information about eigenvector overlaps and the identify of the driving and response nodes. This result complements the findings on localization reported in Fig. 31 for short-duration perturbations to signals with arbitrary frequency content and asymptotically quantifies localization. Interestingly, an exact asymptotic expansion up to order ω^{-2d-1} shows that the entry (i, j) of all powers $m < d(i, j)$ of the Laplacian exactly equals zero, reflecting no existing paths from node j to i of length shorter than their topological distance $d(i, j)$ (see Supplement of Ref. (Zhang *et al.*, 2019)).

For intermediate frequencies in and near the range defined by the Laplacian eigenvalues, resonances occur that induce spatio-temporal responses that are strongly inhomogeneous both as a function of frequency ω and among response nodes i. Interestingly, near resonance frequencies relative response strengths substantially exceed those at low frequencies (see 34b as well as Fig. 2f of Ref. (Zhang *et al.*, 2019)). Here the interaction network topology plays a major role in selecting which nodes and frequencies responses are particularly strong (or weak), stressing the distributed nature of these resonances.

At low driving frequencies, the dynamics at all grid nodes follow the driving signal almost instantaneously, resulting in spatially homogeneous bulk oscillations.

Such analysis transfers to fluctuating signals with distributed frequency content and distributed driven nodes. For instance, grid models driven by purely random processes as well as those driven with power frequency fluctuations characteristic of photovoltaic or wind power generators are well characterized by linear response theory. Only above 95% transmission line loads, a regime to be avoided in real operations for various reasons, linear response theory yields substantial errors.

D. Blackouts as rare events due to large fluctuations

Dynamical instabilities of the power grid dynamics become increasingly important as fluctuations from renewable resources become more frequent and possibly stronger. How “close” is a given system to an unstable state, and thus, what is a typical time scale for fluctuations to kick the system out of its stable operating state? If strong fluctuations are relatively infrequent, it is desirable to quantify how “rare” they are. In addition, one would naively expect that fluctuations of power production with non-Gaussian distributions increase the risk of desynchronization, as large fluctuations are less suppressed in their broad tails. Interestingly, an analytic framework, pursued in (Hindes *et al.*, 2019), quantifies the risk of escape depending on the deviations from Gaussian fluctuations. This work generalizes analytic estimates of (Schäfer *et al.*, 2017) outlined in section V.C.4 in several aspects. It captures distributed dynamics of large grids and Poissonian (rather than Gaussian) noise suited to model fluctuations in real power production.

Hindes *et al.* (2019) employ a WKB-approach applied to classical stochastic systems (cf. also (Dykman *et al.*, 1994)). Interestingly, they find that the rate of desynchronization may exponentially speed up or slow down, depending on how the statistics of fluctuations combines with the least stable mode of the network, described by the Fiedler vector. In contrast to the Kramers-like formula for the escape rate (107), which only depends on the second moment, higher-order moments of the Poissonian noise are captured by the WKB-framework, and their impact on the escape rate may be counterintuitive. As argued below, the escape time $\langle T \rangle$ is proportional to $\exp\left(-(S^{(0)} + \Delta^{(n)} S)\right)$ with action S expanded in powers of the distance to the bifurcation point. Higher-order corrections $\Delta^{(n)} S$ to the leading term $S^{(0)}$ can have both signs, increasing or decreasing the escape time. We summarize the assumptions for this WKB-approach to sketch the main steps of deriving the escape time from a stable state. For detailed derivations see (Hindes *et al.*, 2019) and references therein.

Consider power grids described by the swing equation for synchronous machines, where an input power $\bar{P}_i$ is subject to fluctuations $p_i(t)$. Given histogram data, e.g. from turbulence induced wind-generated power increments, we construct a time series $p_i(t)$ of fluctuations reproducing the increments histogram with bins of size b. The ansatz is overdamped dynamics

$$\dot{p}_i = -\alpha p_i + \xi_i(t), \tag{172}$$

with damping rate α, and a statistical drive $\xi_i(t)$, so that large intermittent spikes are allowed as they are observed for wind and solar sources. The stochastic drive is given as $\xi_i(t) = \sum_{bn} g_{ib}\delta(t - t_{ib}[n])$, where the power increment g_{ib} at i is the average of the pulse amplitude over the bin $b \in \{1, 2, ..., M\}$ of the histogram, where averaged amplitudes are the measured increments $g_i = p_i(t+1) - p_i(t)$, and $t_{ib}[n]$ denotes the time at which the nth such increment in bin b at unit i occurs. For modeling, the driving signal is assumed to be Poisson shot noise, so the time between two events where unit i receives a power increment within bin b is exponentially distributed with a rate ν_{ib} consistent with the histogram.

Consider a synchronized phase-locked state that has emerged through an inverse saddle-node bifurcation as the coupling strengths increased, such that unstable, saddle phase-locked states are in the vicinity of it. Moreover, take typical fluctuations to be small compared to distances to the saddles and large fluctuations to be rare. Such fluctuations are not captured in the large-deviation approach of (Nesti *et al.*, 2018), described in section VII.B.3 where an overload may be also due to many small deviations that accumulate.

The picture behind the analytical approach of (Hindes *et al.*, 2019) is that a large fluctuation drives the system along a most-likely path in phase space. The path connects the stable phase-locked state with the saddle, while fluctuations and the network dynamics co-act as to maximize the probability of desynchronization. To derive the optimal path from classical mechanics, a generalized Fokker-Planck equation for the stochastic network dynamics is adapted to incorporate Poissonian noise. It determines the probability distribution ρ of finding oscillator phases $\mathbf{\Phi}$, phase velocities $\boldsymbol{v}$, fluctuations $\boldsymbol{p}$ at time t. To analyze large fluctuations that are rare we project on the exponential tails of ρ and insert a WKB-ansatz

$$\rho(\mathbf{\Phi}, \boldsymbol{v}, \boldsymbol{p}, t) = B \exp\{-S(\mathbf{\Phi}, \boldsymbol{v}, \boldsymbol{p}, t)\} \tag{173}$$

into the Fokker-Planck equation. Next, the action $S(\boldsymbol{X} + \delta\boldsymbol{X})$ with $\boldsymbol{X} \equiv (\mathbf{\Phi}, \boldsymbol{v}, \boldsymbol{p})$ is expanded in deviations $\delta\boldsymbol{X}$ about $\boldsymbol{X}$, (here the stationary state), where $S(\boldsymbol{X}) \gg 1$, while $|\delta\boldsymbol{X}| \propto 1$ is assumed and only leading order terms in the first derivatives $\partial_{\mathbf{\Phi}} S$, $\partial_{\boldsymbol{v}} S$, $\partial_{\boldsymbol{p}} S$ are kept. As a remark, this ansatz allows to analyze the shape of the probability distribution even in the remote tails for which $\delta\boldsymbol{X} \propto \Omega \gg \Omega^{1/2}$ if $\Omega^{1/2}$ is the typical size of a fluctuation in the stationary state, in contrast to typical and small fluctuations as considered in (106) in Kramers' escape theory or entering (150) as derived from large-deviation theory. Now, inserting (173) into the Fokker-Planck equation yields a Hamilton-Jacobi equation for an "action" $S(\mathbf{\Phi}, \boldsymbol{v}, \boldsymbol{p}, t)$, from which a classical Hamiltonian $H(\mathbf{\Phi}, \boldsymbol{v}, \boldsymbol{p}, \boldsymbol{\lambda}^{\Phi}, \boldsymbol{\lambda}^{v}, \boldsymbol{\lambda}^{p})$ can be read off. The Hamiltonian depends then on "coordinates" $\mathbf{\Phi}, \boldsymbol{v}, \boldsymbol{p}$, their conjugate momenta $\boldsymbol{\lambda}^{\Phi}, \boldsymbol{\lambda}^{v}, \boldsymbol{\lambda}^{p}$ equates to zero, $H(\mathbf{\Phi}, \boldsymbol{v}, \boldsymbol{p}, \boldsymbol{\lambda}^{\Phi}, \boldsymbol{\lambda}^{v}, \boldsymbol{\lambda}^{p}) = 0$. The action reduces to

$$S(\mathbf{\Phi}, \boldsymbol{v}, \boldsymbol{p}) = \sum_i [\int \lambda_i^{\Phi} d\Phi_i + \int \lambda_i^{v} dv_i + \int \lambda_i^{p} dp_i]. \tag{174}$$

The next goal is to determine the optimal (least action) path in phase space as a solution to the classical Hamilton's equations of motion, subject to the boundary conditions to connect the stable fixed point with the unstable saddle. The action along this optimal path is stationary (therefore we skipped already the explicit time dependence of S in (174)) and enables us to estimate the expected waiting time $\langle T \rangle$ for desynchronization via

$$\ln\langle T \rangle \sim S(\mathbf{\Phi}^s, \mathbf{0}, \mathbf{0}) + \mathsf{const}, \tag{175}$$

where $\mathbf{\Phi}^s$ denotes the stationary solution. To estimate $S(\mathbf{\Phi}^s, \mathbf{0}, \mathbf{0})$, the solution is determined for coupling strengths $K = K_{SN}(1 + \kappa)$ close to K_{SN} where saddle node bifurcation happens. To lowest order in κ, parameterizing the distance to the bifurcation point, the solution on the one-dimensional submanifold takes the form

$$\Phi_i(t) = \Phi_i^{\mathsf{SN}} + C\kappa^{1/2} r_i x(t) \tag{176}$$

with $x \in [-1, +1]$ such that for $x = -1$, $\Phi_i(t) = \Phi_i^{\mathsf{SN}} - C\kappa^{1/2} r_i = \Phi_i^*$ the stable fixed point is the starting point, and for $x = +1$ we have $\Phi_i(t) = \Phi_i^{\mathsf{SN}} + C\kappa^{1/2} r_i = \Phi_i^s$ the unstable saddle as the end point of the optimal path; r_i is the component i of the Fiedler mode of the Laplacian that encodes the network topology. This mode is most sensitive to external fluctuations and mediates the (unlikely) escape. The constant C is independent of x_i and κ and depends on the grid adjacency matrix, the phases at the bifurcation point Φ_i^{SN} and the Fiedler mode r_i.

As it turns out (Hindes *et al.*, 2019), to lowest order in κ, the action $S(\mathbf{\Phi}^s, \mathbf{0}, \mathbf{0})$ depends on the damping constant γ, the saddle node coupling K_{SN}, the damping rate of power fluctuations squared (α^2). Moreover, each node i of the grid contributes to S a term proportional to μ_2^{-1} with $\mu_2 = \sum_b \nu_{ib} g_{ib}^2$ being the fluctuation variance. This means that to lowest order in the distance κ to the saddle, the expected time to blackout $\langle T \rangle \propto e^{-S}$ is insensitive to higher-order moments μ_n, $n \geq 3$, of the fluctuations (for Poissonian noise). However, at higher orders in κ, the corrections to S, $\Delta^{(n)} S$, scale with κ according to $\kappa^{n-1/2}$. They depend on higher-order moments

μ_n and on the balance between the Fiedler's mode positive and negative components. For $n = 3$, for example, it is the product of the skewness of the power fluctuation distribution with the skewness of the Fiedler mode that determines whether the non-Gaussianity leads to an increase or decrease of the desynchronization rates, captured by $\Delta^{(n)}S$. Symmetric power fluctuations with μ_3 close to zero yield an increase in the desynchronization rate as naively expected. Overall, this result (Hindes *et al.*, 2019) demonstrates how the network topology interacts with the stochastic dynamics in a non-trivial way.

A further application of the relation between desynchronization and the Fiedler-mode values amounts to a dimensional reduction of the phase space. The phase space is usually high-dimensional for a power grid, but the possible desynchronization paths lie in a low-dimensional subspace under the given assumptions. For networks in which the saddle-node bifurcation is induced by a single overloaded edge with phase difference $\pi/2$ (see also (Fliscounakis *et al.*, 2013; Manik *et al.*, 2014; Rohden *et al.*, 2017)), a so-called synchronized subgraph approximation becomes exact ((Hindes *et al.*, 2019)). The Hamilton's equations of the two subsystems which desynchronize reduce to a single noisy oscillator system in relative phase-space coordinates. More generally, the subgraph approximation is sensible if the corresponding network partition is guided by approximately uniform Fiedler-mode values. Thus, rare desynchronization events become analytically predictable in spite of the high-dimensional phase space of the grid dynamics.

E. Ensembles of power grids for distributed fluctuations

In the previous sections the focus was on the spatio-temporal propagation of a perturbation applied to a single or a few nodes, or the addition or removal of individual lines. M. Mureddu (Mureddu *et al.*, 2015) introduced a suitable framework for estimating, for example, the overall energy mismatch between day-ahead estimates and real data of a whole grid that should be balanced by an appropriate trade on the energy balancing market, differences between production and consumption result from perturbations at all nodes simultaneously. The framework was later employed in different applications (Korjani *et al.*, 2018; Mureddu and Damiano, 2017; Mureddu and Meyer-Ortmanns, 2018).

1. Basic approach

The idea is to consider an ensemble of power grids in analogy to an ensemble of microstates in statistical mechanics. The power grids differ in their "microstates", which enter average values of global observables. Global observables may be the market volume, or the amount of energy that the energy balancing market must compensate or the costs for this amount of energy (Mureddu and Meyer-Ortmanns, 2018), the resilience of the grid (Mureddu and Damiano, 2017), or the optimal positioning of storage devices (Korjani *et al.*, 2018).

The individual "configurations" that represent the microstates are generated from a first reference configuration of producers and consumers that is representative for (part of) the considered region, a certain partition between renewable and conventional power generation, a certain time during the day or a season of the year. The reference configuration is chosen to satisfy the optimal power flow equations (OPF), it is regarded as the operation point of the system. For either transmission or distribution grids, the ensemble of microstates is generated by applying fluctuations in production and consumption relative to the reference configuration.

The fluctuations can be due to load fluctuations, forecast errors for renewables, intra-day electricity trading or others. In the simplest case, the fluctuations are chosen from a truncated Gaussian distribution. Gaussian-like forecast errors defined by standard deviations σ_i at nodes i and represent expected power variations at that node at a given time. For a load of type ℓ (where $\ell \in \{\mathsf{w}, \mathsf{pv} \ldots\}$ denotes wind, photovoltaic and other types of power generation) and power demand P_ℓ, the standard deviation of the forecasting error is denoted as σ_ℓ, and m_ℓ, M_ℓ are the minimum and maximum values of the support of the distribution ρ_ℓ of P_ℓ, respectively, representing power constraints of the different generators. Depending on the different assignments P_ℓ to nodes i, a microstate is sampled by adding a random value to the expected power production or consumption at every node i, where the random variable is extracted from the truncated probability density function $\rho_i^{\mathsf{t}}(x)$

$$\rho_i^{\mathsf{t}}(x) = \begin{cases} 0 & \text{if } x < m_i \\ \rho_i(x) & \text{if } m_i < x < M_i \\ 0 & \text{if } x > M_i \end{cases} \tag{177}$$

where the original densities (with support in all of $\mathbb{R}$) are $\rho_i(x) = \left(2\pi\sigma_i^2\right)^{-1/2} \exp\left(\frac{-x^2}{2\sigma_i^2}\right)$ for wind, photovoltaic or other generation at nodes i. For skewed distributions, modeling, e.g., power production by wind, we may choose a Weibull distribution

$$\rho^{\mathsf{Weibull}}(x; \lambda, a) = \begin{cases} \frac{a}{\lambda}\left(\frac{x}{\lambda}\right)^{a-1} e^{-\left(\frac{x}{\lambda}\right)^a}, & \text{if } x \geq 0 \\ 0, & \text{otherwise} \end{cases} \tag{178}$$

with $a = 2$ (Lun and Lam, 2000; Ning Lu *et al.*, 2013; Seguro and Lambert, 2000) and $\lambda = \frac{2P_{\mathsf{w}}}{\sqrt{\pi}}$, where P_{w} represents the wind power production of the reference configuration and Γ denotes the Gamma-function. Specific values of the parameters fixing the respective distribution depend on the load and the type of the renewable energy and are chosen from recorded data.

As a next step, quantities like the resulting mismatch P_i^j of power at node i in configuration j are measured and the P_i^j summed over all nodes. This way we obtain the total mismatch P^j in power production (the so-called market volume) for a given configuration j, which the market shall balance. To obtain representative values of the market volume, we sample a sufficiently large number of configurations to include in the ensemble. In particular, one can analyze how the distribution of the market volume over the volume size depends on the distribution of fluctuations (normal or Weibull), and – via the choice of the reference configuration – on the time of the day, the season, the geographical zone, and the percentage of renewables with respect to the total production (Mureddu and Meyer-Ortmanns, 2018). The distribution of this market volume enters the market costs, the average prices and the average profit per technology that is involved in the production.

2. A second network layer

To model the energy market and to determine market costs, prices and profit, a second network layer describes market trading. Here one option is agent-based modelling with network nodes representing agents (cf. (Han *et al.*, 2019)), such that the agents are the retailers, with one retailer per conventional power station of the physical grid. In (Mureddu and Meyer-Ortmanns, 2018), the agents first have to undergo a learning phase, in which they learn how to place optimal bids in competitive auctions with the aim of buying (or selling) in the most profitable way. To simulate how real market operators acquire knowledge about the market in time and adapt their decisions, a modified Roth-Erev algorithm (Mureddu *et al.*, 2015; Nicolaisen *et al.*, 2001) adjusts the offer propensities of agents in a self-consistent way with the goal of maximizing profits. The agents interact via a so-called market authority that provides the link between the physical grid and the market. The market authority knows the mismatch from the physical grid and takes the bids of the retailers, accepts or rejects these bids, informs the retailers about the decision and goes on until the required mismatch in energy is covered at the lowest possible costs.

If the energy balance is restored with energy provided by a subset of retailers who offered the energy at the lowest price, the feedback on the physical grid stability must be checked, since the economically best selection need not be reasonable from the viewpoint of grid stability. Lines might get overloaded if the conventional generators which were selected for selling the energy happen to spatially cluster together. Thus this framework of different network layers, coupled via a market authority, allows to analyze the feedback from economical (low costs) to physical (high stability) optimization objectives.

The physical grid stability is particularly endangered if the retailers behave like arbitrageurs when the reserve energy price falls below the price on the intraday market. In such a situation, retailers play a kind of minority game (Ritmeester and Meyer-Ortmanns, 2021). Modeling their behavior accordingly leads to suggestions of how to control arbitrage. For example, if the few big parties, contributing to the market (rather than the many small ones) are made risk-averse due to small penalties, it has a disproportionally large effect on reducing the abuse of price differences in terms of arbitrage. Moreover, from the remarkable analogy of the minority game with spin glasses it becomes understandable why a larger number of retailers may not at all reduce the fluctuations in arbitrage as one would naively expect. Related features of an underlying phase transitions are visible also in realistic markets.

3. Alternatives for treating uncertainties

A number of alternative approaches exist to deal with inherent uncertainties in power and demand. The goal is to derive distributions of induced fluctuations. Induced fluctuations may refer to the energy mismatch (as above), or to induced voltage or frequency fluctuations. An approach called chance-constrained AC optimal power flow (AC CC-OPF) is described in (Roald and Andersson, 2017) and references therein. In contrast to optimal power flow as summarized in section III.B, chance constraints ensure that the system constraints will be satisfied only with a specified probability. The framework of AC CC-OPF not only optimizes the scheduled dispatch with respect to costs, but also the procurement of reserve and voltage control during deviations from expected values. As outlined in (Roald and Andersson, 2017), a number of different options exist for solving this optimization problem under uncertainty. A first one is a one-shot optimization, where the optimal solution is found under respecting all constraints simultaneously (which is very demanding in view of the complexity of the problem). A second one is an iterative solution algorithm. A third option similar to the ensemble approach from above employs Monte Carlo simulations for deriving uncertainty margins and samples uncertainties in power and demand. Here the resulting power flows are calculated for a large number of sample realizations drawn from a given ensemble, leading to Monte-Carlo based uncertainty margins for, e.g., the voltage. For a comparison of the efficiency of the different approaches see (Roald and Andersson, 2017).

IX. SUMMARY AND OUTLOOK

Modern power grids are tasked with incorporating increasing shares of renewable energy sources. This ongoing drastic transformation is crucial to mitigate the climate crisis, but poses novel challenges to our understanding of the collective dynamics of power grid networks. Although the underlying equations have been known for a long time, the treatment of such grids on the systems level remains difficult, mainly due to their nonlinearities and distinct heterogeneities in the dynamics of the nodes and their interaction topology as well as the various kinds of perturbations and fluctuations appearing. Additionally, power grids are embedded in and interconnected to several other complex systems, such as energy markets, consumers, weather and many others. We have discussed here central challenges of decentralized and heterogeneous power grids and ways of how to analyze, understand, design, and influence them.

The review starts with a description of power grids based on principles of physics and the treatment of the most important node models. A crucial aspect here is that renewable sources are connected via electronic inverters. This requires an extension of the classic models and leads to fundamental changes of the dynamics of power grids. To study these models and the variety of analysis techniques, data sets on dynamical parameters and network topologies are necessary. However, data of real power grids are scarce and often incomplete. Therefore, we have presented in Chapter IV typical classes of synthetic models that mimic main properties of real grids, e.g. the classic IEEE test cases, but also more recent developments on generating novel network ensembles, which are often closer to real grids and emphasize the physics perspective. Chapter V discusses an elementary grid containing only one transmission line. This simple bi-stable system serves to introduce the most important static solutions and voltage limits, the bifurcations of the dynamics, and recent stability concepts such as basin stability and stochastic stability, providing a deeper understanding of stability with respect to large and sustained perturbations.

In chapter VI, recent achievements and insights for realistic networks are presented. To function as a power grid, the networked dynamics need to have a stable synchronous (phase-locked) state. However, power grids are typically multistable, exhibiting multiple synchronous yet also asynchronous states that are unsuitable for grid operation. This multistability increases substantially if the ubiquitous losses are included, leading to new types of both, synchronized and desynchronized states. We give an overview of the most successful analytic and probabilistic approaches for managing such rich variety of dynamics, as well as classic linearization-based methods.

The structural stability of grids is the topic of Chapter VII. In complex grids the outage of a single transmission element may induce cascades leading to a large-scale blackout. Such events are well documented in real grids all over the globe, among them several 'monster blackouts'. When a single element fails or is added, the network flows reroute in response. A main grid parameter influencing this rerouting is the network distance. But also the splitting of a grid into different communities has a strong impact. New mathematical descriptions of the rerouting process combining methods from statistical physics, nonlinear dynamics and graph theory are capable of describing these reroutings in new ways and of reliably predicting critical links in a network. It turns out that a local stability analysis is often not sufficient and may be even misleading. The occurrence of cascades following individual failures can also be enhanced by transient effects, showing that dynamical and structural aspects are deeply interwoven. Furthermore, reroutings may yield counterintuitive consequences if transmission elements are added or removed. For instance under certain conditions the reinforcement of a transition line or the addition of a new line may induce a loss of capacity and stability, a phenomenon known as Braess' paradox.

The power grid is subject to fluctuations. Chapter VIII discusses this essential problem with a particular focus on the characteristics introduced by renewables. The non-Gaussian nature of their fluctuations, often characterized by heavy tail distributions, e.g. due to the cloud structure, require new modeling and analysis approaches. First, a linear response theory has been developed to describe the collective spatio-temporal grid dynamics subject to both stationary and transient, non-stationary and distributed input fluctuations. This opens an efficient way of identifying vulnerability patterns. Next, the emergence of resonances, bulk oscillations, or localizations are explained. Recent research demonstrated by a WKB-ansatz that even desynchronization events in grids, which originate from strong, but rare fluctuations, can be predicted. The results revise the naive expectation that fat-tail distributions in fluctuating power production always increase the number of rare events of desynchronization. In real networks with renewable components, fluctuations in generation and consumption occur in parallel, i.e., one cannot restrict the robustness analysis to the failure of a single line. Statistical physics provides alternative approaches to treat this problem, such as the consideration of a whole ensemble of power grids, differing in the realization of fluctuations in its microstates, or by chance-constrained AC optimal power flow.

Aspects of power system control and monitoring were only briefly touched in this review, but will become increasingly important in future power grids with many distributed, fluctuating power sources and low inertia (Milano *et al.*, 2018). This field of research spans from single machines to entire energy system. Current challenges are the development of control systems for grid-forming inverters that guarantee (global) dynamic stability (Colombino *et al.*, 2019; Schiffer *et al.*, 2019) or virtual inertia systems that may replace the mechanic inertia of synchronous machines (Chen *et al.*, 2011; Kerdphol *et al.*, 2019). On the grid level, researchers thrive for a better understanding of the interplay of control systems and network dynamics (Totz *et al.*, 2020; Tumash *et al.*, 2019) and the development of new concepts for the control of complex networks (Cornelius *et al.*, 2013; Huang *et al.*, 2019). Finally, the operation of the large scale load-frequency control system is subject to multiple external influences including markets and regulations (Kruse *et al.*, 2021a,b).

This review demonstrates that the analysis and design of decentralized power grids needs an interdisciplinary approach, where techniques and concepts of power engineering and control theory are newly combined with those from statistical physics, complex dynamical systems, and network science. Such approach will continue to form the backbone for gaining a deeper understanding of all aspects discussed here and will inspire important future research directions.

Future, integrated studies will have to connect the power grid to a broader range of important aspects of the energy system such as the energy market, the information and communication infrastructure driving the control, consumer behavior, e-mobility, political and planning constraints etc. All these aspects point towards the nature of the power grid as part of a multilayered network of networks, embedded in and connected to other complex systems. It becomes increasingly clear that machine learning techniques have enormous potential in the study and control of complex heterogeneous systems. Specifically graph neural networks have vast untapped potential. The question of how to effectively combine such data-driven approaches with physics, engineering-based concepts and generic modeling remains open in the context of power grids.

Finally, a deeper understanding of fundamental concepts underlying the collective dynamics of power grids should enable not just an energy transition in highly developed countries with well-connected grid required to stop contributing to the climate crisis. It may also enable an implementation of sustainable power systems in rural areas of the Global South and in megacities that nowadays may be designed from scratch. Finally, it should improve an understanding of small scale energy islands that can play a crucial role in the sustainable electrification of local communities that still remain off-grid today.

Appendix A: Glossary of acronyms

EMF	Electromotive force
ENTSO-E	European Network of Transmission System Operators for Electricity
HVDC	high voltage directed current
LODF	line outage distribution factor
MILP	mixed integer linear program
OPF	optimal power flow
DC-OPF	linearized or DC optimal power flow
CC-OPF	chance constrained optimal power flow
PI law	proportional integral control law
PTDF	power transfer distribution factor
pu (system)	per unit (system of rescaled units)
RoCoF	Rate of Change of Frequency
WKB	Wentzel-Kramers-Brioullin

ACKNOWLEDGMENTS

This review was produced during our work in the collaborative research project "Kollektive Nichtlineare Dynamik Komplexer Stromnetze" (CoNDyNet) funded by the German Federal Ministry of Education and Research (BMBF grants no. 03EK3055 and 03SF0472). D.W. acknowledges support from the Helmholtz Association via the joint initiative "Energy System 2050 – A Contribution of the Research Field Energy" and the grant no. VH-NG-1025. J.K. was supported by the Russian Ministry of Science and Education Agreement No. 075-15-2020-808.

REFERENCES

Agresti, A., and B. A. Coull (1998), The American Statistician **52** (2), 119.

Ainsworth, N., and S. Grijalva (2013), IEEE Trans. Power Syst. **28** (4), 4310.

Albert, R., I. Albert, and G. L. Nakarado (2004), Phys. Rev. E **69**, 025103.

Albert, R., H. Jeong, and A. Barabási (2000), Nature **406**, 378.

Amro M. Farid et al., (2019), "Liines smart power grid test case repository," `http://amfarid.scripts.mit.edu/Datasets/SPG-Data/index.php`.

Anderson, P. W. (1958), Phys. Rev. **109**, 1492.

Anvari, M., F. Hellmann, and X. Zhang (2020), Chaos: An Interdisciplinary Journal of Nonlinear Science **30** (6), 063140.

Anvari, M., G. Lohmann, M. Wächter, P. Milan, E. Lorenz, D. Heinemann, M. R. R. Tabar, and J. Peinke (2016), New J. Phys. **18** (6), 063027.

Anvari, M., M. Wächter, and J. Peinke (2017), EPL (Europhysics Letters) **116** (6), 60009.

Auer, S., F. Hellmann, M. Krause, and J. Kurths (2017), Chaos: An Interdisciplinary Journal of Nonlinear Science **27** (12), 127003.

Auer, S., K. Kleis, P. Schultz, J. Kurths, and F. Hellmann (2016), Eur. Phys. J. Special Topics **225** (3), 609.

Balestra, C., F. Kaiser, D. Manik, and D. Witthaut (2019), Chaos: An Interdisciplinary Journal of Nonlinear Science **29** (12), 123119.

Bergen, A. R., and D. J. Hill (1981), IEEE Trans. Power App. Syst. **PAS-100**, 25.

Berner, R., S. Yanchuk, and E. Schöll (2021), Physical Review E **103** (4), 042315.

Bialek, J. W., and V. Vahidinasab (2021), IEEE Transactions on Power Systems.

Biggs, N. (1997), Bulletin of the London Mathematical Society **29** (6), 641.

Birchfield, A. (2016), "Electric grid test case repository," `https://electricgrids.engr.tamu.edu/`.

Birchfield, A. B., T. Xu, K. M. Gegner, K. S. Shetye, and T. J. Overbye (2017), IEEE Trans. Power Syst. **32** (4), 3258.

Birchfield, A. B., T. Xu, and T. J. Overbye (2018), IEEE Trans. Power Syst. **33** (6), 6667.

Bloess, A., W.-P. Schill, and A. Zerrahn (2018), Applied Energy **212**, 1611.

Bloomfield, H., D. J. Brayshaw, L. Shaffrey, P. J. Coker, and H. E. Thornton (2018), Environmental Research Letters **13** (5), 054028.

Bollobás, B. (1998), *Modern graph theory* (Springer Science & Business Media, New York).

Bompard, E., L. Luo, and E. Pons (2015), International Journal of Critical Infrastructures 7 **11** (1), 15.

Bosetti, H., and S. Khan (2017), IEEE Transactions on Power Systems **33** (2), 2078.

Böttcher, P. C., A. Otto, S. Kettemann, and C. Agert (2020), Chaos **30**, 013122.

Braess, D. (1968), Unternehmensforschung **12** (1), 258.

Brummitt, C. D., P. D. Hines, I. Dobson, C. Moore, and R. M. D'Souza (2013), Proceedings of the National Academy of Sciences **110** (30), 12159.

Carrasco, J. M., L. G. Franquelo, J. T. Bialasiewicz, E. Galván, R. C. PortilloGuisado, M. M. Prats, J. I. León, and N. Moreno-Alfonso (2006), IEEE Trans. Ind. Electron. **53** (4), 1002.

Carreras, B. A., V. E. Lynch, I. Dobson, and D. E. Newman (2002), Chaos: An Interdisciplinary Journal of Nonlinear Science **12** (4), 985.

Carvalho, R., L. Buzna, R. Gibbens, and F. Kelly (2015), New J. Phys. **17** (9), 095001.

Chen, W., D. Wang, J. Liu, T. Basar, K. H. Johansson, and L. Qiu (2016), IFAC-PapersOnLine **49-22**, 097.

Chen, Y., R. Hesse, D. Turschner, and H.-P. Beck (2011), in *2011 international conference on power engineering, energy and electrical drives* (IEEE) pp. 1–6.

Chopra, N., and M. W. Spong (2009), IEEE Trans. Autom. Control **54** (2), 353.

Christie, R. D. (1999), "Power systems test case archive," `http://www.ee.washington.edu/research/pstca/`.

Clauset, A., C. R. Shalizi, and M. E. Newman (2009), SIAM review **51** (4), 661.

Coffrin, C., D. Gordon, and P. Scott (2014), arXiv preprint arXiv:1411.0359.

Coffrin, C., P. Van Hentenryck, and R. Bent (2012), in *2012 IEEE Power and Energy Society General Meeting* (IEEE) pp. 1–8.

Coletta, T., R. Delabays, I. Adagideli, and P. Jacquod (2016), New J. Phys. **18** (10), 103042.

Coletta, T., and P. Jacquod (2016), Phys. Rev. E **93**, 032222.

Coletta, T., and P. Jacquod (2019), IEEE Transactions on Control of Network Systems **7** (1), 221.

Collins, S., P. Deane, B. Ó. Gallachóir, S. Pfenninger, and I. Staffell (2018), Joule **2** (10), 2076.

Colombino, M., D. Groß, J.-S. Brouillon, and F. Dörfler (2019), IEEE Transactions on Automatic Control **64** (11), 4496.

Cornelius, S. P., W. L. Kath, and A. E. Motter (2013), Nature communications **4** (1), 1.

Cotilla-Sanchez, E., P. D. Hines, C. Barrows, and S. Blumsack (2012), IEEE Systems Journal **6** (4), 616.

Creutzig, F., P. Agoston, J. Goldschmidt, G. Luderer, G. Nemet, and R. Pietzcker (2017), Nature Energy **2** (9), 17140.

Cuffe, P., and A. Keane (2015), IEEE Systems Journal **11** (3), 1810.

Delabays, R., T. Coletta, and P. Jacquod (2016), Journal of Mathematical Physics **57** (3), 032701.

Delabays, R., T. Coletta, and P. Jacquod (2017), Journal of Mathematical Physics **58** (3), 032703.

Dobson, I., B. A. Carreras, V. E. Lynch, and D. E. Newman (2007), Chaos: An Interdisciplinary Journal of Nonlinear Science **17** (2), 026103.

Dobson, I., B. A. Carreras, and D. E. Newman (2005), Probability in the Engineering and Informational Sciences **19** (1), 15.

Dörfler, F., and F. Bullo (2012), in *2012 IEEE 51st IEEE Conference on Decision and Control (CDC)* (IEEE) pp. 7157–7170.

Dörfler, F., and F. Bullo (2012), SIAM Journal on Control and Optimization **50** (3), 1616.

Dörfler, F., and F. Bullo (2013), IEEE Trans. Circ. Syst. I **60**, 150.

Dörfler, F., and F. Bullo (2013), in *2013 IEEE Power & Energy Society General Meeting* (IEEE) pp. 1–5.

Dörfler, F., and F. Bullo (2014), Automatica **50** (6), 1539.

Dörfler, F., M. Chertkov, and F. Bullo (2013), Proceedings of the National Academy of Sciences **110**, 2005.

Dörfler, F., J. W. Simpson-Porco, and F. Bullo (2018), Proceedings of the IEEE **106** (5), 977.

Douglass, D. A., and A.-A. Edris (1996), IEEE Trans. Power Del. **11** (3), 1407.

Dykman, M. I., E. Mori, J. Ross, and P. Hunt (1994), The Journal of chemical physics **100** (8), 5735.

Edenhofer, O., R. Pichs-Madruga, and Y. Sokona, Eds. (2011), *IPCC special report on renewable energy sources and climate change mitigation* (Cambridge University Press, Cambridge, UK).

Engelmann, A., T. Mühlpfordt, Y. Jiang, B. Houska, and T. Faulwasser (2017), IFAC-PapersOnLine **50** (1), 5536.

Erseghe, T. (2014), IEEE Trans. Power Syst. **29** (5), 2370.

Espejo, R., S. Lumbreras, and A. Ramos (2018), IEEE Systems Journal 10.1109/JSYST.2018.2865104.

European Network of Transmission System Operators for Electricity, (2004), "Continental europe operation handbook," `https://www.entsoe.eu/publications/system-operations-reports/operation-handbook`.

Fairley, P. (2004), IEEE Spectrum **41**, 22.

Fiaz, S., D. Zonetti, R. Ortega, J. M. Scherpen, and A. Van der Schaft (2013), European Journal of Control **19** (6), 477.

Fiedler, M. (1973), Czechoslovak Mathematical Journal **23**, 298.

Figueres, C., H. J. Schellnhuber, G. Whiteman, J. Rockström,

A. Hobley, and S. Rahmstorf (2017), Nature **546** (7660), 593.

Filatrella, G., A. H. Nielsen, and N. F. Pedersen (2008), Eur. Phys. J. B **61**, 485.

Fleer, J., and P. Stenzel (2016), Journal of Energy Storage **8**, 320.

Fliscounakis, S., P. Panciatici, F. Capitanescu, and L. Wehenkel (2013), IEEE Trans. Power Syst. **28**, 4909.

Frank, S., I. Steponavice, and S. Rebennack (2012a), Energy Systems **3** (3), 221.

Frank, S., I. Steponavice, and S. Rebennack (2012b), Energy Systems **3** (3), 259.

Gajduk, A., M. Todorovski, and L. Kocarev (2014a), The European Physical Journal Special Topics **223** (12), 2387.

Gajduk, A., M. Todorovski, J. Kurths, and L. Kocarev (2014b), New J. Phys. **16** (11), 115011.

Galindo-González, C. C., D. Angulo-García, and G. Osorio (2020), New Journal of Physics **22** (10), 103033.

Gambuzza, L. V., A. Buscarino, L. Fortuna, M. Porfiri, and M. Frasca (2017), IEEE Journal on Emerging and Selected topics in Circuits and Systems **7** (3), 413.

García-Mata, I., O. Giraud, B. Georgeot, J. Martin, R. Dubertrand, and G. Lemarié (2017), Phys. Rev. Lett. **118**, 166801.

Gelbrecht, M., J. Kurths, and F. Hellmann (2020), New J. Phys. **22** (3), 033032.

Gorjão, L. R., M. Anvari, H. Kantz, C. Beck, D. Witthaut, M. Timme, and B. Schäfer (2020a), IEEE Access **8**, 43082.

Gorjão, L. R., R. Jumar, H. Maass, V. Hagenmeyer, G. C. Yalcin, J. Kruse, M. Timme, C. Beck, D. Witthaut, and B. Schäfer (2020b), Nature Comm. **11**, 6362.

Grainger, J. J., and W. D. Stevenson Jr. (1994), *Power System Analysis* (McGraw-Hill, New York).

Gröger, O., H. A. Gasteiger, and J.-P. Suchsland (2015), Journal of The Electrochemical Society **162** (14), A2605.

Güler, T., G. Gross, and M. Liu (2007), IEEE Trans. Power Syst. **22** (2), 879.

Guo, J., Y. Fu, Z. Li, and M. Shahidehpour (2009), IEEE Trans. Power Syst. **24** (3), 1633.

Guo, L., C. Liang, A. Zocca, S. H. Low, and A. Wierman (2021), IEEE Transactions on Power Systems **36** (5), 4140.

Hackl, J., and B. T. Adey (2018), Journal of Complex Networks **7** (2), 254.

Haehne, H., K. Schmietendorf, S. Tamrakar, J. Peinke, and S. Kettemann (2019), Phys. Rev. E **99**, 050301.

Haehne, H., J. Schottler, M. Waechter, J. Peinke, and O. Kamps (2018), EPL (Europhysics Letters) **121** (3), 30001.

Han, C., D. Witthaut, M. Timme, and M. Schröder (2019), PLoS ONE **14** (11), e0225346.

Hata, S., and H. Nakao (2017), Sci. Rep. **7** (1), 1121.

Heide, D., L. von Bremen, M. Greiner, C. Hoffmann, M. Speckmann, and S. Bofinger (2010), Renewable Energy **35**, 2483.

Hellmann, F., P. Schultz, C. Grabow, J. Heitzig, and J. Kurths (2016), Sci. Rep. **6**, 29654.

Hellmann, F., P. Schultz, P. Jaros, R. Levchenko, T. Kapitaniak, J. Kurths, and Y. Maistrenko (2020), Nature Comm. **11** (1), 1.

Hindes, J., P. Jacquod, and I. B. Schwartz (2019), Phys. Rev. E **100**, 052314.

Hines, P., E. Cotilla-Sanchez, and S. Blumsack (2010), Chaos: An Interdisciplinary Journal of Nonlinear Science **20**, 033122.

Hines, P. D., I. Dobson, and P. Rezaei (2017), IEEE Trans. Power Syst. **32** (2), 958.

Hörsch, J., F. Hofmann, D. Schlachtberger, and T. Brown (2018a), Energy Strategy Reviews **22**, 207.

Hörsch, J., H. Ronellenfitsch, D. Witthaut, and T. Brown (2018b), Electric Power Systems Research **158**, 126 .

Huang, L., J. Coulson, J. Lygeros, and F. Dörfler (2019), in *2019 IEEE 58th Conference on Decision and Control (CDC)* (IEEE) pp. 8130–8135.

Huneault, M., and F. D. Galiana (1991), IEEE Trans. Power Syst. **6** (2), 762.

Hutcheon, N., and J. Bialek (2013), in *IEEE PowerTech (POWERTECH), 2013 Grenoble*.

IPCC, (2014), *Climate Change 2014: Mitigation of CLimate Change. Contribution of Working Group 3 to the Fifth Assessment Report of the Intergovernmental Panel on Climate Change* (Cambridge University Press, Cambridge, United Kingdom).

Jadbabaie, A., N. Motee, and M. Barahona (2004), in *Proceedings of the 2004 American Control Conference*, Vol. 5 (IEEE) pp. 4296–4301.

Jafarpour, S., E. Y. Huang, K. D. Smith, and F. Bullo (2019), arXiv preprint arXiv:1901.11189.

Joe H. Chow (Ed.), (2013), *Power system coherency and model reduction* (Springer, New York Heidelberg Dordrecht London).

Jung, D., and S. Kettemann (2016), Phys. Rev. E **94**, 012307.

K. P. Schneider et al., (1991), "IEEE PES AMPS DSAS Test Feeder Working Group," `http://sites.ieee.org/pes-testfeeders/`.

Kaiser, F., V. Latora, and D. Witthaut (2021a), Nature communications **12**, 3143.

Kaiser, F., H. Ronellenfitsch, V. Latora, and D. Witthaut (2021b), arXiv preprint arXiv:2105.06687.

Kaiser, F., H. Ronellenfitsch, and D. Witthaut (2020a), Nature Comm. **11**, 5796.

Kaiser, F., J. Strake, and D. Witthaut (2020b), New J. Phys. **22**, 013053.

Kaiser, F., and D. Witthaut (2021a), Physical Review Research **3** (2), 023161.

Kaiser, F., and D. Witthaut (2021b), IEEE Access **9**, 67364.

van Kampen, N. (2007), *Stochastic processes in physics and chemistry* (Elsevier, Amsterdam).

Kashima, K., H. Aoyama, and Y. Ohta (2015), in *2015 54th IEEE Conference on Decision and Control (CDC)* (IEEE) pp. 1852–1857.

Katifori, E., G. J. Szöllősi, and M. O. Magnasco (2010), Phys. Rev. Lett. **104**, 048704.

Kavasseri, R., and C. Ababei (2021), "Reds: Repository of distribution systems," `http://www.dejazzer.com/reds.html`.

Kerdphol, T., F. S. Rahman, M. Watanabe, Y. Mitani, D. Turschner, and H.-P. Beck (2019), IEEE Access **7**, 14422.

Kettemann, S. (2016), Phys. Rev. E **94**, 062311.

Kim, H., M. J. Lee, S. H. Lee, and S.-W. Son (2019), Chaos: An Interdisciplinary Journal of Nonlinear Science **29** (10), 103132.

Kim, H., S. H. Lee, J. Davidsen, and S.-W. Son (2018), New J. Phys. **20** (11), 113006.

Kim, H., S. H. Lee, and P. Holme (2015), New J. Phys. **17** (11), 113005.

Kim, H., S. H. Lee, and P. Holme (2016), Phys. Rev. E **93** (6), 062318.

Klein, D. J., and M. Randić (1993), Journal of Mathematical Chemistry **12**, 81.

Klein, M., G. J. Rogers, and P. Kundur (1991), IEEE Trans. Power Syst. **6** (3), 914.

Korjani, S., A. Facchini, M. Mureddu, G. Caldarelli, and A. Damiano (2018), Sci Rep **8** (1), 16658.

Korkali, M., J. G. Veneman, B. F. Tivnan, J. P. Bagrow, and P. D. Hines (2017), Sci. Rep. **7**, 44499.

Kruse, J., B. Schäfer, and D. Witthaut (2021a), arXiv preprint arXiv:2106.04341.

Kruse, J., B. Schäfer, and D. Witthaut (2021b), arXiv preprint arXiv:2109.04802.

Kuehn, C., and S. Throm (2019), SIAM Journal on Applied Mathematics **79** (4), 1271.

Kundur, P. (1994), *Power System Stability and Control* (McGraw-Hill, New York).

Kuramoto, Y. (1975), in *International Symposium on on Mathematical Problems in Theoretical Physics*, Lecture Notes in Physics Vol. 39, edited by H. Araki (Springer, New York) p. 420.

Labavic, D., R. Suciu, H. Meyer-Ortmanns, and S. Kettemann (2015), Eur. Phys. J.: Special Topics **223** (12), 2517.

Liang, X., and C. Andalib-Bin-Karim (2018), IEEE Transactions on Industry Applications **54** (4), 3100.

Lindner, M., and F. Hellmann (2019), Phys. Rev. E **100** (2), 022124.

Liu, H., Z. Hu, Y. Song, and J. Lin (2013), IEEE Trans. Power Syst. **28** (3), 3480.

Liu, Z., X. He, Z. Ding, and Z. Zhang (2018), IEEE Trans. Ind. Inf. **15** (3), 1450.

Lun, I. Y., and J. C. Lam (2000), Renew. Energy **20** (2), 145.

Ma, J., Y. Sun, X. Yuan, J. Kurths, and M. Zhan (2016), PLoS ONE **11** (11), e0165943.

Machowski, J., J. Bialek, and J. Bumby (2008), *Power system dynamics, stability and control* (John Wiley & Sons, New York).

Manik, D., M. Rohden, H. Ronellenfitsch, X. Zhang, S. Hallerberg, D. Witthaut, and M. Timme (2017a), Phys. Rev. E **95** (1), 012319.

Manik, D., M. Timme, and D. Witthaut (2017b), Chaos: An Interdisciplinary Journal of Nonlinear Science **27** (8), 083123.

Manik, D., D. Witthaut, B. Schäfer, M. Matthiae, A. Sorge, M. Rohden, E. Katifori, and M. Timme (2014), Eur. Phys. J. Special Topics **223** (12), 2527.

Medjroubi, W., C. Matke, and D. Kleinhans (2015), "Scigrid– an open source reference model for the european transmission network," `https://www.scigrid.de/`.

Mehrmann, V., R. Morandin, S. Olmi, and E. Schöll (2018), Chaos: An Interdisciplinary Journal of Nonlinear Science **28** (10), 101102.

Mehta, D., N. S. Daleo, F. Dörfler, and J. D. Hauenstein (2015), Chaos: An Interdisciplinary Journal of Nonlinear Science **25** (5), 053103.

Mehta, D., D. K. Molzahn, and K. Turitsyn (2016), in *2016 American Control Conference (ACC)*, pp. 1753–1765.

Menck, P. J., J. Heitzig, J. Kurths, and H. J. Schellnhuber (2014), Nature Comm. **5**, 3969.

Menck, P. J., J. Heitzig, N. Marwan, and J. Kurths (2013), Nature Physics **9**, 89.

Milan, P., M. Wächter, and J. Peinke (2013), Phys. Rev. Lett. **110**, 138701.

Milano, F. (2010), *Power system modelling and scripting* (Springer Science & Business Media).

Milano, F., F. Dörfler, G. Hug, D. J. Hill, and G. Verbič (2018), in *2018 Power Systems Computation Conference (PSCC)* (IEEE) pp. 1–25.

Momoh, J. A., R. Adapa, and M. El-Hawary (1999a), IEEE Trans. Power Syst. **14** (1), 96.

Momoh, J. A., M. El-Hawary, and R. Adapa (1999b), IEEE Trans. Power Syst. **14** (1), 105.

Motter, A. E. (2004), Phys. Rev. Lett. **93**, 098701.

Motter, A. E., and Y.-C. Lai (2002), Phys. Rev. E **66**, 065102.

Motter, A. E., S. A. Myers, M. Anghel, and T. Nishikawa (2013), Nature Physics **9**, 191.

Mureddu, M., G. Caldarelli, A. Chessa, A. Scala, and A. Damiano (2015), PLoS ONE **10** (9), e0135312.

Mureddu, M., and A. Damiano (2017), in *2017 IEEE 26th International Symposium on Industrial Electronics (ISIE)* (IEEE, Edinburgh, United Kingdom) pp. 2069–2074.

Mureddu, M., and H. Meyer-Ortmanns (2018), Physica A **490**, 1324.

Nesti, T., F. Sloothaak, and B. Zwart (2020), Phys. Rev. Lett. **125** (5), 058301.

Nesti, T., A. Zocca, and B. Zwart (2018), Phys. Rev. Lett. **120** (25), 258301.

Newman, M. E. (2012), Nature Physics **8** (1), 25.

Newman, M. E. J. (2010), *Networks – An Introduction* (Oxford University Press, Oxford).

Nicolaisen, J., V. Petrov, and L. Tesfatsion (2001), IEEE Trans. Evol. Computat. **5** (5), 504.

Ning Lu,, Ruisheng Diao, R. P. Hafen, N. Samaan, and Y. V. Makarov (2013), in *2013 IEEE Power & Energy Society General Meeting* (IEEE, Vancouver, BC) pp. 1–5.

Nishikawa, T., and A. E. Motter (2006), Phys. Rev. E **73** (6), 065106.

Nishikawa, T., and A. E. Motter (2015), New J. Phys. **17** (1), 015012.

Nitzbon, J., P. Schultz, J. Heitzig, J. Kurths, and F. Hellmann (2017), New J. Phys. **19** (3), 033029.

Ochab, J., and P. Gora (2010), Acta Phys. Pol. Ser. B, Proc. Suppl. **3**, 453.

Ódor, G., and B. Hartmann (2018), Physical Review E **98** (2), 022305.

Oeding, D., and B. R. Oswald (2016), *Elektrische Kraftwerke und Netze* (Springer).

Olmi, S. (2015), Chaos: An Interdisciplinary Journal of Nonlinear Science **25** (12), 123125.

Olmi, S., A. Navas, S. Boccaletti, and A. Torcini (2014), Phys. Rev. E **90** (4), 042905.

Open energy Modelling Initiative, (2017), `http://www.openmod-initiative.org/`.

Open Power Systems Data, (2017), `http://open-power-system-data.org/`.

Pacific Northwest National Laboratory and National Rural Electric Cooperative Association, (2017), "Data repository for power system open models with evolving resources," `https://egriddata.org/`.

Pagnier, L., and P. Jacquod (2019a), PLoS ONE **14**, e0213550.

Pagnier, L., and P. Jacquod (2019b), Ieee Access **7**, 145889.

Pagnier, L., and P. Jacquod (2019c), "PanTaGruEl - a pan-European transmission grid and electricity generation model," `https://doi.org/10.5281/zenodo.2642175`.

Parks, P. C. (1992), IMA journal of Mathematical Control and Information **9** (4), 275.

Pesch, T., H.-J. Allelein, and J.-F. Hake (2014), Eur. Phys.

J. Special Topics **223**, 2561.

Plietzsch, A., S. Auer, J. Kurths, and F. Hellmann (2019), arXiv preprint arXiv:1903.09585.

Plietzsch, A., P. Schultz, J. Heitzig, and J. Kurths (2016), Eur. Phys. J. Special Topics **225** (3), 551.

Pourbeik, P., P. Kundur, and C. Taylor (2006), IEEE Power and Energy Magazine **4** (5), 22.

Purchala, K., E. Haesen, L. Meeus, and R. Belmans (2005), in *International Symposium CIGRE/IEEE PES, 2005.*, pp. 362–369.

Reseau de Transport d'Electricite (RTE), (2017), "Network frequency," `https://clients.rte-france.com/lang/an/visiteurs/vie/vie_frequence.jsp`, retreived 02/2018.

Risken, H. (1996), *The Fokker-Planck equation* (Springer, Berlin Heidelberg).

Ritmeester, T., and H. Meyer-Ortmanns (2021), Physica A: Statistical Mechanics and its Applications **573**, 125927.

Roald, L., and G. Andersson (2017), IEEE Trans. Power Syst. **33** (3), 2906.

Rockström, J., O. Gaffney, J. Rogelj, M. Meinshausen, N. Nakicenovic, and H. J. Schellnhuber (2017), Science **355** (6331), 1269.

Rodrigues, F. A., T. K. D. Peron, P. Ji, and J. Kurths (2016), Physics Reports **610**, 1.

Rogelj, J., G. Luderer, R. Pietzcker, E. Kriegler, M. Schaeffer, M. Krey, and K. Riahi (2015), Nature Climate Change **5** (6), 519.

Rogers, G. (2012), *Power system oscillations* (Springer Science & Business Media).

Rohden, M., D. Jung, S. Tamrakar, and S. Kettemann (2016), Phys. Rev. E **94**, 032209.

Rohden, M., A. Sorge, M. Timme, and D. Witthaut (2012), Phys. Rev. Lett. **109**, 064101.

Rohden, M., D. Witthaut, M. Timme, and H. Meyer-Ortmanns (2017), New J. Phys. **19** (1), 013002.

Ronellenfitsch, H., D. Manik, J. Horsch, T. Brown, and D. Witthaut (2017), IEEE Trans. Power Syst. 10.1109/TPWRS.2017.2658022.

Sauer, P. W., M. A. Pai, and J. H. Chow (2018), *Power system dynamics and stability: with synchrophasor measurement and power system toolbox* (John Wiley & Sons, Hoboken (NJ)).

Schäfer, B., C. Beck, K. Aihara, D. Witthaut, and M. Timme (2018), Nature Energy **3** (2), 119.

Schäfer, B., M. Matthiae, X. Zhang, M. Rohden, M. Timme, and D. Witthaut (2017), Phys. Rev. E **95**, 060203.

Schäfer, B., M. Timme, and D. Witthaut (2018), in *2018 IEEE PES Innovative Smart Grid Technologies Conference Europe (ISGT-Europe)* (IEEE) pp. 1–5.

Schäfer, B., D. Witthaut, M. Timme, and V. Latora (2018), Nature Comm. **9** (1), 1975.

Schiffer, J., D. Efimov, and R. Ortega (2018), in *2018 IEEE Conference on Decision and Control (CDC)* (IEEE) pp. 800–805.

Schiffer, J., D. Efimov, and R. Ortega (2019), Automatica **109**, 108550.

Schiffer, J., R. Ortega, A. Astolfi, J. Raisch, and T. Sezi (2014), Automatica **50** (10), 2457.

Schlott, M., A. Kies, T. Brown, S. Schramm, and M. Greiner (2018), Applied Energy **230**, 1645.

Schmietendorf, K., J. Peinke, R. Friedrich, and O. Kamps (2014), Eur. Phys. J. Special Topics **223**, 2577.

Schmietendorf, K., J. Peinke, and O. Kamps (2017), Eur. Phys. J. B **90** (11), 222.

Schneider, K. P., B. Mather, B. C. Pal, C.-W. Ten, G. Shirek, H. Zhu, J. Fuller, J. L. R. Pereira, L. Ochoa, L. De Araujo, *et al.* (2018), IEEE Trans. Power Syst. **33** (3), 3181.

Schröder, M., M. Timme, and D. Witthaut (2017), Chaos: An Interdisciplinary Journal of Nonlinear Science **27** (7), 073119.

Schultz, P., J. Heitzig, and J. Kurths (2014a), New J. Phys. **16** (12), 125001.

Schultz, P., J. Heitzig, and J. Kurths (2014b), Eur. Phys. J. Special Topics **223** (12), 2593.

Schultz, P., F. Hellmann, J. Heitzig, and J. Kurths (2016), arXiv preprint arXiv:1701.06968.

Schultz, P., F. Hellmann, K. N. Webster, and J. Kurths (2018), Chaos: An Interdisciplinary Journal of Nonlinear Science **28** (4), 043102.

Seguro, J., and T. Lambert (2000), J. Wind Eng. Ind. Aerod. **85** (1), 75.

Semerow, A., S. Höhn, M. Luther, W. Sattinger, H. Abildgaard, A. D. Garcia, and G. Giannuzzi (2015), "Dynamic study model for the interconnected power system of continental europe in different simulation tools," .

Setreus, J., and L. Bertling (2008), in *Proceedings of the 10th International Conference on Probablistic Methods Applied to Power Systems* (IEEE) pp. 1–8.

Sharafutdinov, K., L. Rydin Gorjão, M. Matthiae, T. Faulwasser, and D. Witthaut (2018), Chaos: An Interdisciplinary Journal of Nonlinear Science **28** (3), 033117.

Simonsen, I., L. Buzna, K. Peters, S. Bornholdt, and D. Helbing (2008), Phys. Rev. Lett. **100**, 218701.

Simpson-Porco, J. W. (2017), IEEE Trans. Power Syst. **33** (3), 2477.

Skar, S. J. (1980), SIAM Journal on Applied Mathematics **39** (3), 475.

Solé, R. V., M. Rosas-Casals, B. Corominas-Murtra, and S. Valverde (2008), Phys. Rev. E **77** (2), 026102.

Soltan, S., A. Loh, and G. Zussman (2018), IEEE Systems Journal **13** (1), 625.

Soltan, S., and G. Zussman (2016), in *2016 IEEE Power and Energy Society General Meeting (PESGM)* (IEEE) pp. 1–5.

Song, Y., D. J. Hill, and T. Liu (2015), IEEE Conf. Control Applications (CCA) , 201 .

Staffell, I., and S. Pfenninger (2018), Energy **145**, 65.

Stott, B. (1979), Proceedings of the IEEE **67** (2), 219.

Stott, B., J. Jardim, and O. Alsac (2009), IEEE Trans. Power Syst. **24** (3), 1290.

Strake, J., F. Kaiser, F. Basiri, H. Ronellenfitsch, and D. Witthaut (2018), New J. Phys. **21**, 053009.

Taher, H., S. Olmi, and E. Schöll (2019), Physical Review E **100** (6), 062306.

Tamrakar, S., M. Conrath, and S. Kettemann (2018), Sci. Rep. **8**, 6459.

Taylor, R. (2012), Journal of Physics A: Mathematical and Theoretical **45** (5), 055102.

Torres-Sánchez, L., G. T. Freitas de Abreu, and S. Kettemann (2020), Phys. Rev. E **101**, 012313.

Totz, C. H., S. Olmi, and E. Schöll (2020), Physical Review E **102** (2), 022311.

Trias, A. (2012), in *Power and Energy Society General Meeting, 2012 IEEE* (IEEE) pp. 1–8.

Tumash, L., S. Olmi, and E. Schöll (2018), EPL (Europhysics Letters) **123** (2), 20001.

Tumash, L., S. Olmi, and E. Schöll (2019), Chaos: An Interdisciplinary Journal of Nonlinear Science **29** (12), 123105.

Tyloo, M., T. Coletta, and P. Jacquod (2018), Phys. Rev.

Lett. **120**, 084101.

Tyloo, M., and P. Jacquod (2020), IEEE Control Systems Letters **5** (3), 929.

Tyloo, M., L. Pagnier, and P. Jacquod (2019), Science Advances **5** (11), eaaw8359.

UCTE Operations Handbook, (2009), "Policy 1: Load-frequency control and performance," `https://www.entsoe.eu/fileadmin/user_upload/_library/publications/entsoe/Operation_Handbook/introduction_v25.pdf`.

Union for the Co-ordination of Transmission of Electricity, (2004), "Final report of the investigation committee on the 28 september 2003 blackout in italy," `https://www.entsoe.eu/fileadmin/user_upload/_library/publications/ce/otherreports/20040427_UCTE_IC_Final_report.pdf`.

Union for the Coordination of Transmission of Electricity, (2007), "Final report on the system disturbance on 4 november 2006," `https://www.entsoe.eu/fileadmin/user_upload/_library/publications/ce/otherreports/Final-Report-20070130.pdf`.

U.S.-Canada Power System Outage Task Force, (2014), "Final Report on the August 14, 2003 Blackout in the United States and Canada: Causes and Recommendations," `https://energy.gov/sites/prod/files/oeprod/DocumentsandMedia/BlackoutFinal-Web.pdf`.

Van Cutsem, T., and C. Vournas (2007), *Voltage stability of electric power systems* (Springer Science & Business Media).

Van Hertem, D., J. Verboomen, K. Purchala, R. Belmans, and W. Kling (2006), in *The 8th IEEE International Conference on AC and DC Power Transmission*, pp. 58–62.

Venkatasubramanian, V., and Y. Li (2004), Bulk Power System Dynamics and Control-VI, Cortina dAmpezzo, Italy , 22.

Verboomen, J., D. Van Hertem, P. H. Schavemaker, W. L. Kling, and R. Belmans (2005), in *Future Power Systems, 2005 International Conference on* (IEEE) pp. 6–pp.

Villella, F., S. Leclerc, I. Erlich, and S. Rapoport (2012), in *3rd IEEE PES International Conference and Exhibition on Innovative Smart Grid Technologies (ISGT Europe)* (IEEE) pp. 1–9.

Van der Vleuten, E., and V. Lagendijk (2010), Energy Policy **38** (4), 2042.

Wang, Z., A. Scaglione, and R. J. Thomas (2010), IEEE Trans. Smart Grid **1** (1), 28.

Weber, J., J. Wohland, M. Reyers, J. Moemken, C. Hoppe, J. G. Pinto, and D. Witthaut (2018), PLoS ONE **13** (8), e0201457.

Weckesser, T., H. Jóhannsson, and J. Østergaard (2013), in *2013 IREP Symposium Bulk Power System Dynamics and Control-IX Optimization, Security and Control of the Emerging Power Grid* (IEEE) pp. 1–9.

Wiedermann, M., J. F. Donges, J. Kurths, and R. V. Donner (2016), Phys. Rev. E **93** (4), 042308.

Wiegmans, B. (2016), "GridKit extract of ENTSO-E interactive map," `https://doi.org/10.5281/zenodo.55853`.

Wiser, R., K. Jenni, J. Seel, E. Baker, M. Hand, E. Lantz, and A. Smith (2016), Nature Energy **1** (10), 16135.

Witthaut, D., M. Rohden, X. Zhang, S. Hallerberg, and M. Timme (2016), Phys. Rev. Lett. **116**, 138701.

Witthaut, D., and M. Timme (2012), New J. Phys. **14**, 083036.

Witthaut, D., and M. Timme (2015), Phys. Rev. E **92** (3), 032809.

Wohland, J., N. E. Omrani, N. Keenlyside, and D. Witthaut (2019), Wind Energy Science **4** (3), 515.

Wohland, J., M. Reyers, J. Weber, and D. Witthaut (2017), Earth System Dynamics **8** (4), 1047.

Wolff, M. F., P. G. Lind, and P. Maass (2018), Chaos: An Interdisciplinary Journal of Nonlinear Science **28** (10), 103120.

Wolff, M. F., K. Schmietendorf, P. G. Lind, O. Kamps, J. Peinke, and P. Maass (2019), Chaos: An Interdisciplinary Journal of Nonlinear Science **29** (10), 103149.

Wood, A. J., B. F. Wollenberg, and G. B. Sheblé (2014), *Power Generation, Operation and Control* (John Wiley & Sons, New York).

Xi, K., J. L. Dubbeldam, and H. X. Lin (2017), Chaos: an interdisciplinary journal of nonlinear science **27** (1), 013109.

Xu, T., A. B. Birchfield, and T. J. Overbye (2018), IEEE Trans. Power Syst. **33** (6), 6501.

Yang, Y., and A. E. Motter (2017), Phys. Rev. Lett. **119**, 248302.

Yang, Y., T. Nishikawa, and A. E. Motter (2017), Science **358** (6365), eaan3184.

Yang, Z., K. Xie, J. Yu, H. Zhong, N. Zhang, and Q. Xia (2019), IEEE Trans. Power Syst. **34** (2), 1315.

You, H., V. Vittal, and X. Wang (2004), IEEE Transactions on power systems **19** (1), 483.

Zhang, H., G. T. Heydt, V. Vittal, and J. Quintero (2013), IEEE Trans. Power Syst. **28** (3), 3471.

Zhang, H., and P. Li (2010), IET Generation, Transmission & Distribution **4** (5), 553.

Zhang, X., S. Hallerberg, M. Matthiae, D. Witthaut, and M. Timme (2019), Science Advances **5** (7), eaav1027.

Zhang, X., D. Witthaut, and M. Timme (2020), Phys. Rev. Lett. **125**, 218301.

Zhang, X.-P., C. Rehtanz, and B. Pal (2012), *Flexible AC transmission systems: modelling and control* (Springer, Heidelberg).

Zhang, Y., L. Wehenkel, P. Rousseaux, and M. Pavella (1997), International Journal of Electrical Power & Energy Systems **19** (3), 195.

Zhou, K., I. Dobson, Z. Wang, A. Roitershtein, and A. P. Ghosh (2020), IEEE Transactions on Power Systems **35** (4), 3224.

Zimmerman, R. D., C. E. Murillo-Sanchez, and R. J. Thomas (2011), IEEE Trans. Power Syst. **26**, 12.

Zocca, A., C. Liang, L. Guo, S. H. Low, and A. Wierman (2021), arXiv preprint arXiv:2105.05234.